

**Carnegie Mellon University**  
CARNEGIE INSTITUTE OF TECHNOLOGY

THESIS

Submitted in Partial Fulfillment of the Requirements  
for the Degree of Doctor of Philosophy

TITLE

**ATOMIC-LEVEL MODELING OF THE  
EARLY STAGES OF Cu(100) OXIDATION**

PRESENTED BY

**MINYOUNG LEE**

ACCEPTED BY THE DEPARTMENT OF MECHANICAL ENGINEERING

---

ADVISOR, MAJOR PROFESSOR	DATE
--------------------------	------

---

DEPARTMENT HEAD	DATE
-----------------	------

APPROVED BY THE COLLEGE COUNCIL

---

DEAN	DATE
------	------



# ATOMIC-LEVEL MODELING OF THE EARLY STAGES OF Cu(100) OXIDATION

Submitted in partial fulfillment  
of the requirements for the degree of

Doctor of Philosophy

in

Mechanical Engineering

by

Minyoung Lee

M.S., Mechanical Engineering, Carnegie Mellon University, 2006

B.S., Mechanical Engineering, Seoul National University, 2001

Carnegie Mellon University  
Pittsburgh, Pennsylvania

December 2010



© Minyoung Lee 2010  
All Rights Reserved



# ABSTRACT

ATOMIC-LEVEL MODELING OF THE EARLY STAGES OF Cu(100) OXIDATION

by

Minyoung Lee

Chair: Alan McGaughey

The early stages of Cu(100) oxidation are investigated at the atomic-level using density functional theory (DFT) calculations. First, the transition from the  $c(2 \times 2)$  phase to the missing-row reconstruction phase is studied from energetic and kinetic view points. Using the nudged elastic band method, potential ejection paths are proposed. Vacancies and adatoms are found to affect the ejection energetics and lower the energy barriers in some cases. The findings suggest that a missing row will form quickly once the first copper atom ejects. Non-coordinated (i.e., one-by-one) and coordinated (i.e., the ejection of two copper atoms at the same time) ejections are compared. It is found that the non-coordinated ejection path is favorable above temperatures of 343 K. The energy barriers for the copper diffusion following the ejection are calculated to be much smaller than the ejection barriers and are comparable to those for diffusion on the  $c(2 \times 2)$  phase. This result, which suggests a copper diffusion channel, is consistent with the interpretation of an earlier scanning tunneling

microscopy experiment.

Next, the transition from the missing-row reconstruction phase to  $\text{Cu}_2\text{O}$  nucleation is investigated. On the missing-row reconstructed surface, the energy barrier for atomic oxygen embedment is smaller through the missing row compared to other paths, suggesting a mechanism for the formation of sub-surface oxygen structures that are consistent with experimental results. When the missing-row reconstructed surface is exposed to an additional oxygen molecule, surface restructuring that leads to oxide-like structures is only observed when sub-surface oxygen is present. The oxide-like nature of these structures is confirmed through structural, Bader, and electron density of states analyses. These findings demonstrate the key role played by sub-surface oxygen in  $\text{Cu}(100)$  oxidation. Then, the missing-row reconstruction is confirmed as a necessary event in  $\text{Cu}(100)$  oxidation by showing that the relative stability of the surface is increased two times more through the missing-row reconstruction than through the unreconstructed surface. No evidence of  $\text{Cu}_2\text{O}$ -like structures is found on unreconstructed  $\text{Cu}(100)$  surfaces.

To validate the proposed transition mechanisms at finite temperature and pressure conditions, an *ab-initio* atomistic thermodynamics framework is applied to the intermediate structures predicted by the DFT calculations. In range of 100 - 1000 K and  $10^{-15}$  -  $10^5$  atm, the experimentally observed  $c(2 \times 2)$ , missing-row reconstruction, and bulk  $\text{Cu}_2\text{O}$  phases are predicted as stable states. Then, it is demonstrated that the DFT-predicted missing-row reconstruction structures including extra on- or sub-surface oxygen atoms can be the most stable structures for certain finite temperature and pressure conditions.



## ACKNOWLEDGEMENTS

I have been supported by a diverse group of people during my Ph.D. research experience. Let me use this opportunity to thank all of them.

First of all, I would like to thank my wife, Yeon Hee, who is my best friend, counselor, and motivator, for her encouragement, advice, patience, and support. Because of her, I was able to arrive at this goal and I can now dream of something more. I thank my grandmother, parents, brother, and sister-in-law for their support, prayers, and confidence. My father has taught me strong will and enthusiasm and my mother has always given me unconditional love and belief.

I would like to thank Professor Alan McGaughey for being my thesis advisor. Although I lost confidence in myself at times, he always encouraged me and believed in me. He suggested proper directions and helped me to make the right decisions when I encountered many obstacles during this thesis research. I would also like to thank Professors John Kitchin, Burak Ozdoganlar, and Judith Yang for serving on my thesis committee.

I want to thank the members of the Nanoscale Transport Phenomena Laboratory (NTPL) and Thermal Energy Engineering Laboratory. In particular: Eric Landry, John Thomas, Joe Turney, Haibin Chen, Jason Larkin, Alex Massicotte, Wee Liat Ong, Scott Schiffres, Zonghui Su, and Sang eun Jee. Eric and John deserve my special thanks for helping me to get used to the NTPL academically and culturally. Special

thanks to Sang eun for good discussions and suggestions about the kinetic Monte Carlo simulations discussed in Chapter VII.

I would also like to thank my collaborators. Dr. Dominic Alfonso (National Energy Technology Laboratory) helped me learn to use VASP. Professor Wissam Al-Saidi (University of Pittsburgh) gave me many opportunities to discuss the *ab initio* atomistic thermodynamic framework used in Chapter VI and density functional theory calculations. Professor Simon Phillpot, Professor Susan Sinnott, Bryce Devine, and Ray Shan from Department of Materials Science and Engineering, University of Florida generously allowed me to use their computing resources and gave me good feedback.

I also thank the Center for Simulation and Modeling at the University of Pittsburgh, the department of Chemical Engineering at Carnegie Mellon University, and the Texas Advanced Computing Center (part of National Science Foundation-TeraGrid) for providing computing resources.

Finally, this thesis research has been funded by the Department of Energy, Office of Basic Energy Sciences, Division of Materials Science and Engineering (Grant No. DOE FGOA01ER45919).

# TABLE OF CONTENTS

<b>ABSTRACT</b> . . . . .	<b>ii</b>
<b>ACKNOWLEDGEMENTS</b> . . . . .	<b>iv</b>
<b>LIST OF TABLES</b> . . . . .	<b>viii</b>
<b>LIST OF FIGURES</b> . . . . .	<b>x</b>
<b>NOMENCLATURE</b> . . . . .	<b>xv</b>
<b>CHAPTERS</b>	
<b>I. Introduction</b> . . . . .	<b>1</b>
1.1 Motivation . . . . .	1
1.2 Atomic-level observations of oxygen covered Cu(100) surfaces . . . . .	2
1.3 Thesis overview and scope . . . . .	8
<b>II. DFT-based modeling of unreconstructed and missing-row reconstructed Cu(100) surfaces</b> . . . . .	<b>11</b>
2.1 Introduction to density functional theory (DFT) . . . . .	11
2.2 O <sub>2</sub> adsorption on a Cu(100) surface . . . . .	13
2.3 Structural comparison of missing-row reconstruction between DFT-predictions and experimental measurements . . . . .	17
2.4 Summary . . . . .	20
<b>III. Energetics and kinetics of the <math>c(2 \times 2)</math> to <math>(2\sqrt{2} \times \sqrt{2})R45^\circ</math> transition on the Cu(100) surface</b> . . . . .	<b>22</b>
3.1 Introduction . . . . .	22
3.2 Calculation methodology . . . . .	24
3.3 $c(2 \times 2)$ to $(2\sqrt{2} \times \sqrt{2})R45^\circ$ transition . . . . .	25
3.4 Summary . . . . .	33
<b>IV. Energetics of oxygen embedment into unreconstructed and reconstructed Cu(100) surfaces</b> . . . . .	<b>35</b>
4.1 Introduction . . . . .	35
4.2 Calculation methodology . . . . .	36
4.3 Oxygen embedment energetics . . . . .	40
4.4 Summary . . . . .	47
<b>V. Role of sub-surface oxygen in Cu(100) oxidation</b> . . . . .	<b>48</b>

5.1	Introduction . . . . .	48
5.2	Calculation methodology . . . . .	49
5.3	Oxygen-induced surface restructuring . . . . .	51
5.4	Summary . . . . .	64
<b>VI. <i>Ab-initio</i> atomistic thermodynamics study of early stages of Cu(100) oxidation . . . . .</b>		<b>66</b>
6.1	Introduction . . . . .	66
6.2	Calculation methodology . . . . .	67
6.3	Results . . . . .	69
6.4	Summary . . . . .	78
<b>VII. Summary of contributions and suggested directions for future work . . . .</b>		<b>80</b>
7.1	Summary of contributions . . . . .	80
7.2	Future research directions . . . . .	84
<b>BIBLIOGRAPHY . . . . .</b>		<b>89</b>

## LIST OF TABLES

### Table

2.1	The minimum adsorption energy and its associated distance ( $d$ ) between the two oxygen atoms and height ( $z$ ) above the copper surface. The sites are defined in Fig. 2.1(a). Atomic or molecular oxygen adsorption is identified by using “2O” or “O <sub>2</sub> ”.	16
2.2	Comparison of relaxed structural parameter values between the unreconstructed and reconstructed (missing-row reconstruction) Cu(100) surfaces at an oxygen coverage of 0.5 ML calculated by DFT. . . . .	18
2.3	Comparison between the structural parameter values for the reconstructed (missing-row reconstruction) Cu(100) surface at an oxygen coverage 0.5 ML from DFT calculations and experimental results (PhD: photoelectron diffraction, LEED: low energy electron diffraction). . . . .	20
3.1	Energy difference, $E_{diff}$ , and energy barrier, $E_{barrier}$ , for the copper ejection paths shown in Figs. 3.1(a), 3.3(a), 3.3(b), 3.3(c), 3.4(a), and 3.5(a). . . . .	28
3.2	Energy difference, $E_{diff}$ , and energy barrier, $E_{barrier}$ , for copper diffusion paths during the transition from the $c(2 \times 2)$ to the missing-row reconstructed Cu(100) surface. The copper diffusion paths are shown in Figs. 3.6(a) and 3.6(b) for diffusion following the copper ejection and in Fig. 3.6(c) for diffusion on the perfect $c(2 \times 2)$ phase. . . . .	32
4.1	Surface-oxide energy, $E_S$ , energy difference, $E_{diff}$ , and energy barrier, $E_{barrier}$ , for oxygen embedment into the Cu(100) $p(2 \times 2)$ and $p(4 \times 4)$ unit cells at different oxygen coverages. The unit cell area is 26.645 Å <sup>2</sup> for $p(2 \times 2)$ and 106.58 Å <sup>2</sup> for $p(4 \times 4)$ . $E_{diff}$ is calculated by subtracting the total system energy of the initial state from that of final state. $E_{barrier}$ is the energy difference between the initial state and the local energy maximum. . . . .	40
4.2	Surface-oxide energy, $E_S$ , energy difference, $E_{diff}$ , and energy barrier, $E_{barrier}$ , for oxygen embedment into the Cu(100) $p(2\sqrt{2} \times 2\sqrt{2})$ unit cell with different surface morphologies [ $c(2 \times 2)$ w/ 0.25 DV is $c(2 \times 2)$ with 0.25 ML disordered vacancy]. The unit cell area is 53.290 Å <sup>2</sup> for all cases and the coverage is 0.5 ML. . . . .	42
4.3	Surface-oxide energy, $E_S$ , energy difference, $E_{diff}$ , and energy barrier, $E_{barrier}$ , for oxygen embedment into the missing-row reconstructed Cu(100) surface for different embedding paths. The initial and final positions of the embedding oxygen atom are shown in Fig. 4.5. . . . .	45

5.1	Surface-oxide energy, $E_S$ , and height change for different on- and sub-surface oxygen coverages. The unit cell area is $26.645 \text{ \AA}^2$ for $p(2 \times 2)$ and $53.290 \text{ \AA}^2$ for $p(2\sqrt{2} \times 2\sqrt{2})$ . “U” and “R” represent unreconstructed and reconstructed surfaces. Oxygen coverages are shown for on-surface (On-) and sub-surface (Sub-) separately. 2octa2, 2octa23, 2octa123, and 2octa1234 are missing-row reconstructed (mr) surfaces relaxed with sub-surface oxygen atoms [see Figs. 5.2(a) and 5.2(b)]. . . . .	52
5.2	Surface-oxide energy, $E_S$ , of missing-row reconstructed Cu(100) surfaces including extra oxygen atoms at the on- and/or sub-surface sites [see Figs. 5.2(a) and 5.2(b)]. In the columns below $E_S$ , the results for surfaces relaxed without or with an additional oxygen molecule are provided. For the surfaces relaxed with an additional oxygen molecule, we use four different initial positions: fcc hollow (FCC), between fcc hollow and $\text{Cu}_S$ (BFC), perpendicular to missing-row (PMR), and parallel to missing-row (RMR) [see Fig. 5.1(a)]. The unit cell area is $53.290 \text{ \AA}^2$ for $p(2\sqrt{2} \times 2\sqrt{2})$ and $213.16 \text{ \AA}^2$ for $p(4\sqrt{2} \times 4\sqrt{2})$ . The bolded $E_S$ values correspond to the oxide-like structures, some of which are shown in Figs. 5.5(a), 5.5(b), 5.5(e), and 5.5(f). . . .	55
5.3	Surface-oxide energy, $E_S$ , of $p(4 \times 4)$ Cu(100) surfaces without and with an additional oxygen molecule. For each oxygen coverage, the configuration of surface oxygen atoms is chosen so as to minimize the energy [i.e. $c(2 \times 2)$ phase of oxygen for 0.5 ML coverage]. The initial positions of the additional oxygen molecule are the top-bridge (TB), fcc hollow (FCC), and unoccupied fcc hollow (UFC) sites [see Fig. 5.8(a)]. “-” indicates no data (e.g., there is no UFC site at 1.0 ML coverage). For on-surface coverage of 0.6875 ML, one of surface-adsorbed oxygen atoms at 0.75 ML embedded into the sub-surface region and the sub-surface coverage is thus 0.0625 ML (the summation of on- and sub-surface coverage is 0.75 ML). The unit cell area is $106.58 \text{ \AA}^2$ . . . . .	62
6.1	Surface-oxide energy, $E_S$ , for structures in the early stages of Cu(100) oxidation. For each oxygen coverage, the configuration of surface oxygen atoms is chosen so as to minimize the energy [i.e. $c(2 \times 2)$ phase of oxygen for 0.5 ML coverage]. The relaxed structures are shown in Fig. 6.1. The unit cell surface area, $A_{surf}$ , is $26.65 \text{ \AA}^2$ for $p(2 \times 2)$ unit cell and $53.29 \text{ \AA}^2$ for $p(2\sqrt{2} \times 2\sqrt{2})$ unit cell. . . . .	72
6.2	Surface-oxide energy, $E_S$ , of potential intermediate states between missing-row reconstruction and bulk $\text{Cu}_2\text{O}$ nucleation. The relaxed structures are shown in Fig. 6.3. The index notation is explained in Chapter V. The unit cell surface area, $A_{surf}$ , is $53.29 \text{ \AA}^2$ for $p(2\sqrt{2} \times 2\sqrt{2})$ unit cell. . . . .	76

## LIST OF FIGURES

### Figure

1.1	UHV-TEM images of $\text{Cu}_2\text{O}$ islands formed on the $\text{Cu}(100)$ surface at different temperatures. (a) Triangular shape at $350^\circ\text{C}$ . (b) Square shape at $500^\circ\text{C}$ . (c) Nano-rod shape at $600^\circ\text{C}$ . (d) Pyramid shape at $700^\circ\text{C}$ . (e) Pyramid with flat terrace at $1000^\circ\text{C}$ . Copyright 2003 Elsevier B.V. . . . .	3
1.2	Scanning tunneling microscopy (STM) images: (a) $c(2\times 2)$ phase. The area of this STM image is $55\times 55 \text{ \AA}^2$ . The black circles are adsorbed oxygen atoms at four-fold hollow sites and the open circles are copper atoms on the topmost layer of the $\text{Cu}(100)$ surface. Copyright 1996 The American Physical Society. (b) $p(2\sqrt{2} \times \sqrt{2})R45^\circ$ (missing-row reconstruction) phase. The area of this STM image is $15\times 15 \text{ \AA}^2$ . The unit cell is shown as a white square and the missing row is in the (001) direction. The bright region inside the unit cell indicates a oxygen-copper-oxygen chain. Copyright 1991 The American Physical Society. (c) Cartoon of the $p(2\sqrt{2} \times \sqrt{2})R45^\circ$ (missing-row reconstruction) phase. . . . .	4
1.3	(a) Surface phase diagram for $\text{Cu}(100)$ -oxygen at different temperature and pressure conditions. The solid line is an equilibrium phase boundary between the $p(2\sqrt{2} \times \sqrt{2})R45^\circ$ and $c(2\times 2)$ with 0.25 ML disordered vacancy phases. The dashed line is the hysteretic boundary for oxygen adsorption and desorption. The oxygen coverage is 1.0 ML for $p(1\times 1)$ and 0.5 ML for both $p(2\sqrt{2} \times \sqrt{2})R45^\circ$ and $c(2\times 2)$ with 0.25 ML disordered vacancy. (b) $c(2\times 2)$ with 0.25 ML disordered vacancy structure. The dashed square indicates the unit cell. The small red spheres are oxygen atoms and big spheres are copper atoms. The topmost copper atoms are colored dark grey. Copyright 2007 The American Physical Society. . . . .	6
1.4	(a) Derivative form of scanning tunneling microscope (STM) image of $\text{Cu}(100)$ surface after $9.4\times 10^5 \text{ L}$ oxygen exposure at $373 \text{ K}$ . The area of this STM image is $400\times 300 \text{ \AA}^2$ . (b) Line profiles 1, 2, and 3 shown from Fig. 1.4(a). Copyright 2007 American Institute of Physics. . . . .	7
1.5	Simplified top and side views of structures during the early stages of $\text{Cu}(100)$ oxidation. . . . .	8
2.1	$p(3\times 3)$ $\text{Cu}(100)$ surface. The narrow lines between copper atoms are created by the visualization program and have no physical meaning. (a) Top view. Oxygen molecule adsorption sites: top sites (1-2), fcc sites (3-4) and bridge sites (5-6). (b) Side view. $d$ is the bond length and $z$ is the height between the center of mass of the oxygen molecule and the surface copper atoms. . . . .	14
2.2	(a) Determining the zero-pressure bulk fcc lattice constant. (b) Finding the optimum number of $k$ -points for the surface calculations. . . . .	15

2.3	(a) Site 5 adsorption state. The oxygen molecule is fully dissociated and two oxygen atoms are adsorbed at fcc hollow sites, which are the most favorable adsorption sites on Cu(100) surface. (b) Site 4 adsorption state. The oxygen-oxygen bond is elongated but not dissociated yet (i.e., molecular oxygen adsorption). See Table 2.1 for the adsorption energy for each state. . . . .	17
2.4	Structural parameters of the Cu(100) reconstructed (missing row) surface at 0.5 ML coverage. (a) Distances between copper and oxygen atoms. (b) Vertical distances between oxygen atoms and copper layers. The values for these parameters are provided in Table 2.2. . . . .	18
2.5	Comparison between unreconstructed and reconstructed structures on the Cu(100) surface. The arrows indicate the size of the unit cell. (a) Relaxed $c(2 \times 2)$ structure, top view. (b) Relaxed missing-row reconstruction $[(2\sqrt{2} \times \sqrt{2})R45^\circ]$ , top view. (c) $c(2 \times 2)$ structure, side view. (d) Relaxed missing-row reconstruction $[(2\sqrt{2} \times \sqrt{2})R45^\circ]$ , side view. . . . .	19
3.1	(a) Top view and (b) Side view of the $p(4 \times 4)$ unit cell showing the initial (A) and final positions (B, C, and D) for the ejection at the first copper atom. For reference, the $p(2\sqrt{2} \times 2\sqrt{2})$ unit cell is contained by the white dashed lines. . . . .	26
3.2	Energetics of copper ejection on the $p(4 \times 4)$ unit cell ( $E$ = image energy, $E_0$ = energy of image 0). The initial (A) and final positions (B, C, and D) of each path are shown in Figs. 3.1(a) and 3.1(b). . . . .	27
3.3	Three possibilities for the second copper ejection: (a) with vacancy and adatom (w/ V&Ad), (b) with vacancy (w/ V), and (c) coordinated ejection (two neighboring copper atoms eject at the same time, $\times 2$ ). The energy barriers are provided in Table 3.1. . . . .	28
3.4	Comparing the energetics of coordinated and non-coordinated copper atom ejection for the A $\rightarrow$ C path. (a) Reaction pathway. (b) Transition rates vs. temperature. The energy barriers are provided in Table 3.1. In Eq. (3.1), $\nu_o$ is taken to be $1.0E+13$ [1/s], the typical frequency of an atomic vibration. The non-coordinated ejection is more probable than the coordinated ejection at temperatures higher than 343 K [vertical dashed line in Fig. 3.4(b)] . . . . .	29
3.5	Comparing the energetics of coordinated and non-coordinated copper atom ejection for the A $\rightarrow$ D path. (a) Reaction pathway. (b) Transition rates vs. temperature. The energy barriers are provided in Table 3.1. In Eq. (3.1), $\nu_o$ is taken to be $1.0E+13$ [1/s], the typical frequency of an atomic vibration. The non-coordinated ejection is more probable than the coordinated ejection at temperatures higher than 356 K [vertical dashed line in Fig. 3.5(b)] . . . . .	30
3.6	Copper diffusion paths following the copper ejection from (a) C sites and (b) B and D sites. "V" is the copper vacancy, which is the original location of the ejected copper atom. The dashed arrows are the ejection paths and the solid arrows are the diffusion paths. The "B" and "D" sites (black) are the initial positions and "B", "C", "D", "I", "II", and "III" (blue) are final positions]. (c) Copper diffusion paths on the perfect $c(2 \times 2)$ phase. Path $\gamma$ is over an oxygen atom. There is no oxygen atom along path $\alpha$ . . . . .	31



3.7	Copper ejection and diffusion paths that are most likely to occur during the transition from $c(2\times 2)$ to $(2\sqrt{2}\times\sqrt{2})R45^\circ$ on the Cu(100) surface (the original position of the ejected copper atoms are indicated by dashed circles): (a) $A\rightarrow B\rightarrow C-\beta$ path, and (b) $A1\rightarrow C1-A2\rightarrow C2$ w/ $V\&Ad-C1\rightarrow II$ path. (c) NEB results for each path. .	33
4.1	Cu(100) surface structures used in this work. The squares indicate the unit cells. The $p(4\times 4)$ unit cell area is four times bigger than the $p(2\times 2)$ unit cell area. Copyright 2009 Elsevier B.V. . . . .	37
4.2	(a) Top and (b) side view of the $p(2\times 2)$ unit cell at 0.25 ML coverage with four images for a NEB calculation. (c) Top and (d) side view of the $p(2\sqrt{2}\times 2\sqrt{2})$ unit cell (missing-row reconstruction) at 0.5 ML coverage with four images for a NEB calculation. Copyright 2009 Elsevier B.V. . . . .	38
4.3	Energetics of embedding an oxygen atom into the (a) the $p(2\times 2)$ unit cell and (b) the $p(4\times 4)$ unit cell ( $E$ = image energy, $E_0$ = energy of image 0). The embedding progress is the ratio of the embedding distance of each image to the total embedding distance. Lines are shown to guide the eye. Copyright 2009 Elsevier B.V. . . . .	42
4.4	Energetics of embedding an oxygen atom into the $p(2\sqrt{2}\times 2\sqrt{2})$ unit cell for different surface morphologies. ( $E$ = image energy, $E_0$ = energy of image 0) at 0.5 ML coverage. The embedding progress is the ratio of the embedding distance of each image to the total embedding distance. Lines are shown to guide the eye. Copyright 2009 Elsevier B.V. . . . .	43
4.5	(a) Top and (b) Side view of the $p(2\sqrt{2}\times 2\sqrt{2})$ unit cell and the initial and final positions of the embedding oxygen atom. Copyright 2009 Elsevier B.V. . . . .	44
4.6	Illustrations for embedding (a) path1 and (b) path3. The initial and final positions of the embedding oxygen atom are provided in Table 4.3 and Fig. 4.5. (c) Embedding oxygen atom energetics for path1-path4 into the missing-row reconstructed Cu(100) surface. . . . .	45
4.7	Illustrations for embedding (a) path5 and (b) path6. The initial and final positions are provided in Table 4.3 and Fig. 4.5. (c) Sub-surface oxygen atom diffusion energetics for path5 and path6 in the missing-row reconstructed Cu(100) surface. .	46
5.1	Initial positions of the oxygen molecule on the missing-row reconstructed Cu(100) surface. (a) Top and (b) side view of the $p(2\sqrt{2}\times 2\sqrt{2})$ unit cell at 0.5 ML coverage: 1. fcc hollow site (FCC). 2. Between fcc and $Cu_S$ (BFC). 3. Perpendicular to missing row (PMR). 4. Parallel to missing row (RMR). The oxygen molecules are only shown in (a). Copyright 2010 Elsevier B.V. . . . .	49
5.2	(a) Top and (b) side views of the unrelaxed missing-row reconstructed Cu(100) surface with on- and sub-surface oxygen atoms in the $p(2\sqrt{2}\times 2\sqrt{2})$ unit cell. Copyright 2010 Elsevier B.V. . . . .	50
5.3	Top and side views of (a) the clean Cu(100) surface, (b) the missing-row reconstruction (mr), and missing-row reconstructed surfaces relaxed with sub-surface oxygen atoms [(c) 2octa123 and (d) 2octa1234]. Copyright 2010 Elsevier B.V. . . . .	53

5.4	Surface-oxide energy vs. oxygen coverage on the missing-row reconstructed Cu(100) surface with extra on- and sub-surface oxygen atoms. For each index, $E_S$ is plotted for the case without an additional oxygen molecule and the minimum value found in the presence of an additional oxygen molecule (see data in Table 5.2). For each index, the $E_S$ of the surface relaxed without an oxygen molecule (“No O <sub>2</sub> ”) is connected to that of the surface relaxed with an oxygen molecule (“With O <sub>2</sub> ”) by an arrow. Copyright 2010 Elsevier B.V. . . . .	56
5.5	Oxygen-molecule induced surface restructuring on the missing-row reconstructed Cu(100) surface with extra on- and sub-surface oxygen atoms: (a) Top and (b) side views of 2octa12 FCC. (c) Top and (d) side views of 2octa123 PMR. (e) Top and (f) side views of 2octa1234 FCC. (g), (h) O-Cu-O bond in bulk Cu <sub>2</sub> O. Copyright 2010 Elsevier B.V. . . . .	57
5.6	Bader net charge vs. position measured from the fixed bottom layer for (a) oxygen and (b) copper atoms in surfaces relaxed with an oxygen molecule at different sub-surface oxygen coverages. The charges for atoms in bulk CuO and Cu <sub>2</sub> O are provided as dashed lines. Copyright 2010 Elsevier B.V. . . . .	58
5.7	Density of states for the (a) <i>p</i> -O and (b) <i>d</i> -Cu orbitals in the oxide-like 2octa1234 FCC and bulk Cu <sub>2</sub> O. The atomic indices are shown in Figs. 5.5(c), 5.5(d), 5.5(e), and 5.5(f). The average energies of each <i>d</i> - and <i>p</i> -orbital ( <i>d</i> -band center and <i>p</i> -band center) are shown with dashed and solid vertical lines for 2octa1234 FCC and bulk Cu <sub>2</sub> O. Copyright 2010 Elsevier B.V. . . . .	59
5.8	Initial positions of the oxygen molecule on the unreconstructed Cu(100) surface before structural relaxation. (a) Top and (b) side view of the unreconstructed <i>p</i> (4×4) unit cell at 0.5 ML coverage. The initial positions are labeled: 1. Top-bridge (TB), 2. Fcc hollow (FCC), and 3. Unoccupied fcc hollow (UFC). There are 16 octahedral (octa) sites in sub-surface region one of which is shown. . . . .	61
5.9	Potential oxidation paths on the unreconstructed and missing-row reconstructed Cu(100) surfaces. The surface-oxide energies ( $E_S$ ) are calculated from the <i>p</i> (4×4) unit cell for the unreconstructed path and from the <i>p</i> (2√2×2√2) unit cell for the missing-row reconstructed path. The surface-oxide energies are presented in Table 5.3 for the unreconstructed path. “0.75+0.25 ML” means on-surface coverage 0.75 ML with sub-surface coverage 0.25 ML. For the missing-row reconstructed path, MRR stands for the missing-row reconstructed Cu(100) surface and MRR w/ “Sub O” denotes the missing-row reconstructed Cu(100) surface with sub-surface oxygen. The MRR structures with an oxygen molecule are denoted by O <sub>2</sub> . . . . .	63
6.1	Top view of surface structures during the early stages of Cu(100) oxidation: (a) clean surface. (b) 2×2 phase at 0.25 ML oxygen coverage. (c) <i>c</i> (2×2) phase at 0.5 ML oxygen coverage. (d) missing-row reconstruction (MRR). (e) bulk Cu <sub>2</sub> O. (f) oxygen coverage 0.75 ML. (g) oxygen coverage 1.0 ML. (h) MRR with vacancy disorder [ <i>c</i> (2×2) w/ 0.25 DV]. MRR with copper vacancy at (i) not adjacent (Cu <sub>C</sub> ) and (j) adjacent (Cu <sub>S</sub> ) to the missing row. (k) MRR with an oxygen vacancy. MRR with two oxygen vacancies located (l) horizontally (2O-H), (m) vertically (2O-V), and (n) diagonally (2O-D). All these relaxed structures are visualized using the <i>p</i> (2√2×2√2) unitcell. . . . .	71

6.2	(a) Surface free energy [ $\gamma(T, p_{O_2})$ ] of the early stages of Cu(100) oxidation as a function of the relative oxygen chemical potential ( $\Delta\mu_o$ ). (b) Phase diagram predicted from Fig. 6.2(a)[these structures are shown in Figs. 6.1(a), 6.1(b), 6.1(d), and 6.1(e)]. The phase boundaries between 0.25 ML and MRR from an experiment (Iddir et al.) and a previous <i>ab-initio</i> thermodynamics calculation (Duan et al.) are shown for comparison. . . . .	73
6.3	Top and side views of relaxed structures that may exist between the missing-row reconstruction (MRR) and bulk Cu <sub>2</sub> O nucleation: MRR with additional on-surface oxygen atoms at (a) two hol7 sites (2hol7), (b) two hol8 sites (2hol8), and (c) two hol7 and hol8 sites (2hol78). MRR with additional sub-surface oxygen atoms at (d) two octa2 sites, (e) octa1 and octa2 sites, (f) two octa1 and octa2 sites, (g) two octa1 and octa2 sites, (h) two octa2 and octa3 sites, (i) octa1-4 sites, (j) two octa1-3 sites, (k) two octa1-4 sites, and (l) two octa1-4 sites with an oxygen molecule at FCC site (hol and octa sites are specified in Chapter V. Although (a)-(j) structures with an additional oxygen molecule are included in our <i>ab-initio</i> thermodynamics framework investigation, we show the only meaningful case, (l), here. . . . .	75
6.4	(a) Surface free energy ( $E_S$ ) of early stages of Cu(100) oxidation including intermediate states between the missing-row reconstruction and the bulk Cu <sub>2</sub> O formation as a function of oxygen chemical potential ( $\Delta\mu_o$ )(the bulk Cu <sub>2</sub> O limit, -1.24 eV, is provided by a dashed line), and (b) Phase diagram predicted from Fig. 6.4(a)[these structures are shown in Figs. 6.3(a), 6.3(h), 6.3(j), and 6.3(l)]. The arrow points out the transition observed by Lahtonen et al. as shown in Fig. 6.5. . . . .	77
6.5	Average thickness of oxide layer on Cu(100) surface at 373 K reproduced using the data of Lahtonen et al. For the vertical axis, 0.5 ML coverage in the O <sub>2</sub> pressure $7.89 \times 10^{-10}$ atm ( $8.0 \times 10^{-7}$ mbar) corresponds to 4 Å in the oxygen partial pressure $3.65 \times 10^{-5}$ atm ( $3.7 \times 10^{-5}$ mbar). The Cu(100) surface at 0.5 ML oxygen coverage is fully missing-row reconstructed [ $(2\sqrt{2} \times \sqrt{2})R45^\circ$ ]. The O <sub>2</sub> pressure regimes ( $7.9 \times 10^{-10}$ atm and $3.7 \times 10^{-5}$ atm) are separated by the break. . . . .	78
7.1	Number ratio between embedded oxygen atoms ( $N_{\text{embed O}}$ ) and total number of oxygen atoms ( $N_{\text{total O}}$ ) vs. initial oxygen coverages on a Cu(100) surface during DFT-based Lattice Gas kinetic Monte Carlo (LG-KMC) simulations. Data and graph courtesy of Dr. Sang eun Jee. . . . .	85
7.2	(a) Adsorption sites on the Cu(110) surface (3h: three-fold hollow site, 4h: four-fold hollow site, t: top site, sb: short bridge site, lb: long bridge site). (b) Side view of the Cu(110) surface. The topmost copper layer is colored differently. . . . .	87
7.3	Oxygen-induced reconstruction on Cu(110) surface; (a) Top and (b) Side view of added-row reconstruction (The arrows of the topmost copper atom indicate the copper diffusion direction). (c) Top and (d) Side view of missing-row reconstruction. . . . .	88

## NOMENCLATURE

$A$	initial site of ejection path
$ab - initio$	first principles
$Ad$	adatom
$A_{surf}$	unit cell surface area
$B, C, C1, C2$	final sites of ejection paths
$Cu_C$	copper atom not adjacent to missing row
$Cu_S$	copper atom at step edge site adjacent to missing row
$d$	distance between two oxygen atoms in an oxygen molecule
$D$	final sites of ejection paths
$DV$	disordered vacancy
$e$	charge of an electron, $1.60217 \times 10^{-19}$ C
$E$	energy calculated by density functional theory
$E_S$	surface-oxide energy
$F$	Helmholtz free energy
$G$	Gibbs free energy
$H$	enthalpy
$\hbar$	reduced Planck constant, $6.62606 \times 10^{-34}$ J-s
hol	face centered cubic hollow site

I, II, III	final sites of subsequent diffusion paths
$k_B$	Boltzmann constant, $1.38065 \times 10^{-23}$ J/K
$m$	mass of electron, $9.10938 \times 10^{-31}$ kg
$N$	number of atoms
octa	octahedral site
$p, p^0$	pressure, standard pressure (=1 atm)
$\mathbf{r}$	position vector of electron
$T$	temperature
tetra	tetrahedral site
V	vacancy
$V_{eff}$	effective external potential
$V$	volume
$z$	height of an oxygen molecule above copper surface
-D	diagonally distributed
-H	horizontally distributed
-V	vertically distributed

## Greek symbols

$\alpha, \beta, \gamma$	diffusion paths
$\Delta$	relative difference
$\Psi_i(\mathbf{r})$	wavefunction of Kohn-Sham orbital
$\gamma$	surface free energy
$\varepsilon_i$	energy of Kohn-Sham orbital
$\mu$	chemical potential
$\nu_0$	atomic vibrational frequency

## Subscripts

<i>barrier</i>	energy barrier
<i>bulk</i>	bulk structure
<i>Cu</i>	copper
<i>diff</i>	energy difference
<i>embedO</i>	number of embedded oxygen atoms
<i>f</i>	formation
<i>Final</i>	final state
<i>H</i>	harmonic approximation
<i>Initial</i> , 0	initial state
mr, MRR	missing row, missing-row reconstruction
<i>O</i> , <i>O</i> <sub>2</sub>	oxygen, oxygen molecule
<i>O/Cu</i>	oxygen adsorbed on copper surface
<i>Path</i>	ejection or diffusion path
<i>slab</i>	slab structure

totalO	number of total oxygen atoms
<i>vib</i>	vibration

## Acronyms

ARUPS	angle-resolved ultraviolet photoemission spectroscopy
BFC	between fcc and Cu <sub>5</sub>
DFT	density functional theory
FCC	face centered cubic
GGA	generalized gradient approximation
LDA	local density approximation
LEED	low energy electron diffraction
LG	lattice gas
KMC	kinetic Monte Carlo
ML	monolayers
NEB	nudged elastic band
PBC	periodic boundary conditions
PDOS	projected density of state
PhD	photoelectron diffraction
PMR	perpendicular to missing row
RMR	parallel to missing row
SEXAFS	surface extended xray absorption fine structure
STM	scanning tunneling microscopy
TB	top-bridge
TEM	transmission electron microscopy

TST	transition state theory
UFC	unoccupied face centered cubic
UHV	ultra high vacuum
VASP	Vienna <i>ab-initio</i> simulation package
XPS	x-ray photoelectron spectroscopy



## CHAPTER I

### Introduction

#### 1.1 Motivation

Copper and its oxides ( $\text{CuO}$  and  $\text{Cu}_2\text{O}$ ) are relevant in many scientific and engineering applications.  $\text{Cu}_2\text{O}$ , which is a direct band gap semiconductor, is a candidate material for next-generation photovoltaic cells [1,2]. As candidates to replace rare and expensive noble metal catalysts, copper,  $\text{CuO}$ , and  $\text{Cu}_2\text{O}$  have been investigated for the synthesis of methanol [3–5] and bio-chemical compounds [6], automobile catalytic converters [7], and the prevention of CO poisoning in fuel cells [8,9]. For example, copper surfaces with adsorbed oxygen or copper oxides can induce CO adsorption,  $\text{CO}_2$  formation, and  $\text{CO}_2$  desorption without a Pt catalyst [10]. It is thus important to understand the atomic structure and energetics of copper-oxide interfaces and how the associated free surfaces interact with their environments.

It was traditionally believed that copper oxide grows as a uniform layer on a clean copper surface [11]. Yang et al., however, found by *in situ* ultra high vacuum (UHV) transmission electron microscopy (TEM) that oxide islands nucleate and grow on the  $\text{Cu}(100)$  surface [12]. Based on the existing experimental and theoretical data, the oxidation of a  $\text{Cu}(100)$  surface is a four-step process that proceeds as more oxygen molecules arrive at the surface: (i) Oxygen molecules dissociate and the oxygen atoms

adsorb on the face-centered cubic (fcc) hollow sites up to 0.5 monolayer (ML) coverage [ $c(2\times 2)$  phase] [13–24]. (ii) The  $(2\sqrt{2}\times\sqrt{2})R45^\circ$  missing-row reconstruction is formed by the release of every fourth row of copper atoms from the top copper layer [25–36]. (iii) Merged missing-row reconstructed domains are formed and  $\text{Cu}_2\text{O}$  islands nucleate [37, 38]. (iv) Islands grow and merge with other islands to form a continuous oxide layer [12, 39–42]. The oxide grows into the substrate metal as well as horizontally along the surface [41, 42].

The shape of the oxide islands depends on the copper surface orientation, temperature, and oxygen partial pressure. Zhou et al. observed various nano-structures of copper (I) oxide ( $\text{Cu}_2\text{O}$ ) islands on the  $\text{Cu}(100)$  surface, as shown in Fig. 1.1 [39, 40]. At a temperature of  $600^\circ\text{C}$  [see Fig. 1.1(c)], they observed an elongated nano-rod structure, whose size and aspect ratio are determined by the oxidation time [39, 40]. At the higher temperatures, the oxide islands have pyramid shapes [40], as shown in Figs. 1.1(d) and 1.1(e).

The growth of the nano-rod structure (and other morphologies) is an example of self-assembly, a process in which a structure is built from the bottom-up without direct intervention [43]. To take advantage of the different morphologies, we need to better understand the atomic-level mechanisms of copper oxidation.

## 1.2 Atomic-level observations of oxygen covered $\text{Cu}(100)$ surfaces

The initial oxygen adsorption on a copper surface has been investigated by experiments [12, 14, 15, 25, 26, 28–30, 32, 34, 39, 41, 42, 44–50] and *ab initio* (i.e., first principles) calculations [13, 16–22, 24, 27, 31, 33, 35, 51–59]. Initially, cluster model calculations were widely used [13, 51, 53]. However, with increasing computing power, surface models with periodic boundary conditions (using  $k$ -point sampling and plane

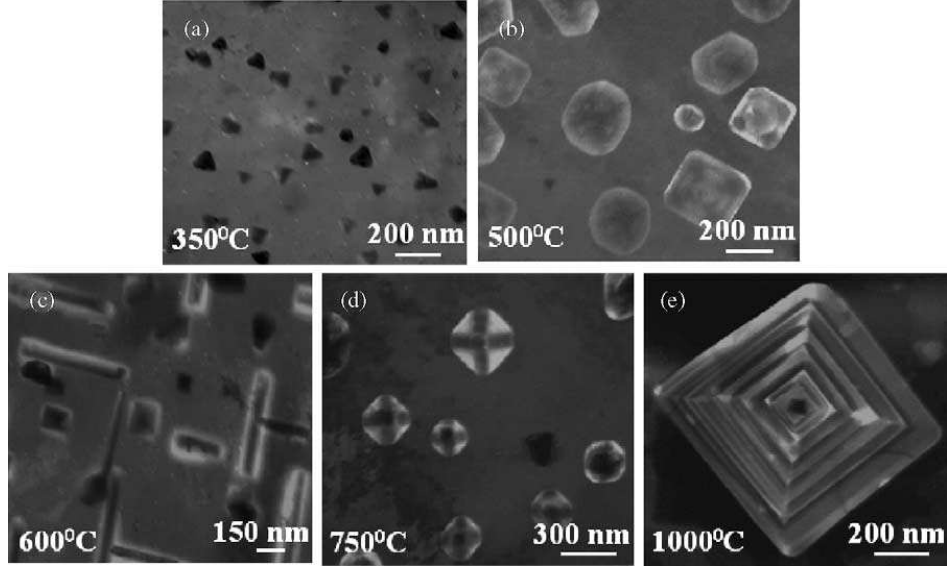


Figure 1.1: UHV-TEM images of  $\text{Cu}_2\text{O}$  islands formed on the  $\text{Cu}(100)$  surface at different temperatures. (a) Triangular shape at  $350^\circ\text{C}$ . (b) Square shape at  $500^\circ\text{C}$ . (c) Nano-rod shape at  $600^\circ\text{C}$ . (d) Pyramid shape at  $750^\circ\text{C}$ . (e) Pyramid with flat terrace at  $1000^\circ\text{C}$ . Copyright 2003 Elsevier B.V.

wave basis sets) are now widely used [20–22, 33, 35, 54, 57–59]. The low index copper surfaces [(100), (110), and (111)] are frequently chosen [13, 16, 17, 19].

On the  $\text{Cu}(100)$  surface, Alatalo and co-workers investigated (i) the oxygen adsorption energies by density functional theory (DFT) calculations [20], and (ii) the dynamics of oxygen molecule dissociation and atomic oxygen adsorption by *ab initio* molecular dynamics simulation [22]. Based on their computational work and previous experimental observations, it is understood that when a copper surface is exposed to an oxygen environment, oxygen molecules approach the surface, dissociate [16, 17, 20], and adsorb on the next-nearest-neighbor hollow sites, as shown in Fig. 1.2(a) [23].

The oxygen coverage on the  $\text{Cu}(100)$  surface is defined as the ratio of the number of oxygen-occupied four-fold hollow sites to the total number of four-fold hollow sites. If

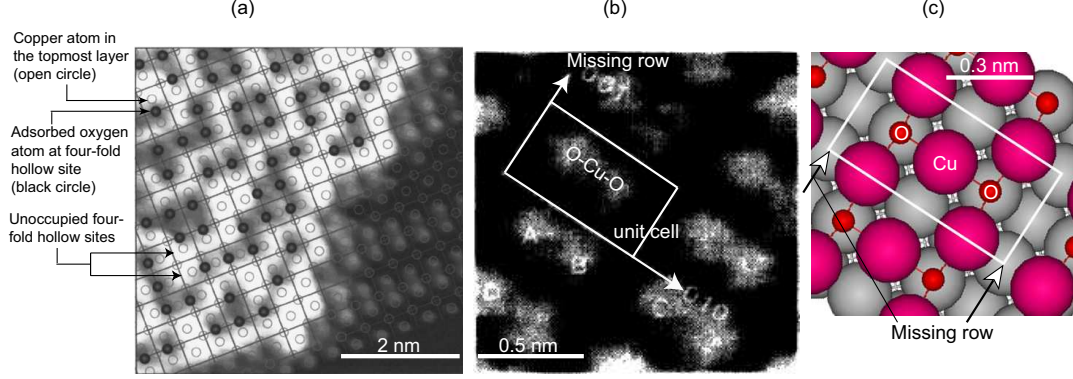


Figure 1.2: Scanning tunneling microscopy (STM) images: (a)  $c(2\times 2)$  phase. The area of this STM image is  $55\times 55 \text{ \AA}^2$ . The black circles are adsorbed oxygen atoms at four-fold hollow sites and the open circles are copper atoms on the topmost layer of the Cu(100) surface. Copyright 1996 The American Physical Society. (b)  $p(2\sqrt{2} \times \sqrt{2})R45^\circ$  (missing-row reconstruction) phase. The area of this STM image is  $15\times 15 \text{ \AA}^2$ . The unit cell is shown as a white square and the missing row is in the (001) direction. The bright region inside the unit cell indicates a oxygen-copper-oxygen chain. Copyright 1991 The American Physical Society. (c) Cartoon of the  $p(2\sqrt{2} \times \sqrt{2})R45^\circ$  (missing-row reconstruction) phase.

one out of every four hollow sites is occupied by an oxygen atom, the oxygen coverage of the surface is 0.25 monolayer (ML). It is known that for a wide range of temperature and pressure conditions, as the oxygen coverage approaches 0.5 ML, the  $c(2\times 2)$  phase evolves into the missing-row reconstruction  $[p(2\sqrt{2} \times \sqrt{2})R45^\circ]$  [26, 30, 60]. Jensen et al. proposed that the missing row forms by the ejection of every fourth row of the top copper layer, as shown in Figs. 1.2(b) and 1.2(c) [26]. This mechanism has been supported by experimental and computational investigations [14, 28–36, 38]. Using scanning tunneling microscopy (STM), Fujita et al. found that nano-meter size domains of the  $c(2\times 2)$  phase [see Fig. 1.2(a)] are formed and transform into the missing-row reconstruction  $[p(2\sqrt{2} \times \sqrt{2})R45^\circ]$  as the surface-adsorbed oxygen coverage increases from 0.34 ML to 0.5 ML. The nucleation and growth of the oxide islands does not begin until after the surface reconstruction is complete.

There have been many experimental and computational studies aimed at identifying the driving force behind the Cu(100) reconstruction. Experimental techniques

including low energy electron diffraction (LEED) [25], scanning tunneling microscopy (STM) [26,28], surface extended x-ray absorption fine structure (SEXAFS) [14], angle-resolved ultraviolet photoemission spectroscopy (ARUPS) [29], and photoelectron diffraction (PhD) [30] have been applied. Typical computational methods for this investigation are surface Madelung potentials within the muffin-tin approximation [31] and atomic vibrational mode calculation by DFT [32]. Based on these experimental and computational results, two driving forces for the missing-row reconstruction have been suggested: surface stress [14, 32] and long-range Coulombic interactions [31]. The stabilities of the  $c(2\times 2)$  and  $(2\sqrt{2} \times \sqrt{2})R45^\circ$  phases at an oxygen coverage of 0.5 ML have been compared using DFT-predicted chemisorption energies and average binding energies per oxygen atom [33,36]. The  $(2\sqrt{2} \times \sqrt{2})R45^\circ$  phase is consistently found to be more stable than the  $c(2\times 2)$  phase, but the energy differences are small (e.g., 0.1 eV for the difference of average binding energy) [36].

Although these experimental and computational works revealed many secrets of the missing-row reconstruction, questions remain including: (i) Why is the missing-row reconstruction highly probable during Cu(100) oxidation? (ii) How do the copper atoms eject and diffuse? (iii) What are the energy barriers of ejection and diffusion? To answer these questions, we need to investigate the  $c(2\times 2)$ -( $2\sqrt{2} \times \sqrt{2})R45^\circ$  transition at the atomic level.

After the missing-row reconstruction is complete,  $\text{Cu}_2\text{O}$  islands nucleate and grow [12]. The phase transition between the missing-row reconstruction and  $\text{Cu}_2\text{O}$  island nucleation has been investigated by experimental [34,37,38] and computational [57, 61] methods. Iddir et al. used the *in situ* synchrotron x-ray scattering method to examine oxygen adsorption on the Cu(100) surface for different oxygen partial pressures and temperatures, and constructed the surface phase diagram shown in

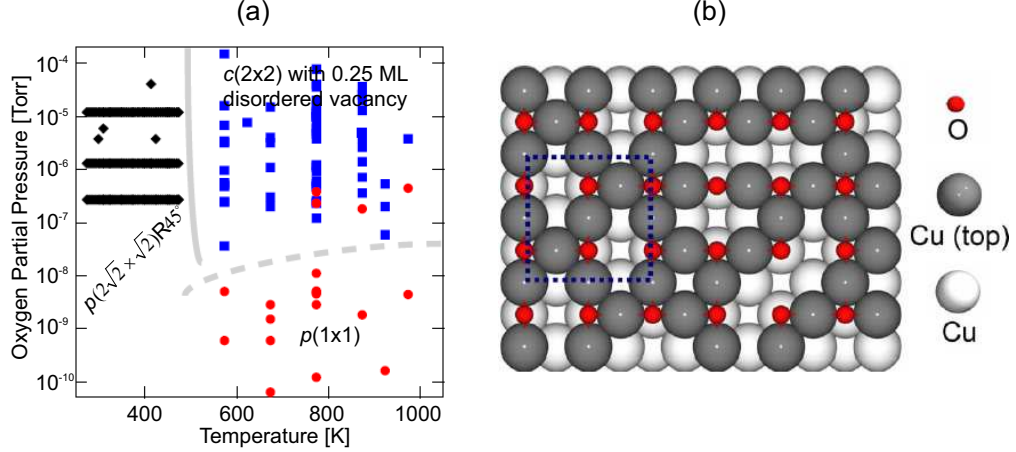


Figure 1.3: (a) Surface phase diagram for Cu(100)-oxygen at different temperature and pressure conditions. The solid line is an equilibrium phase boundary between the  $p(2\sqrt{2} \times \sqrt{2})R45^\circ$  and  $c(2 \times 2)$  with 0.25 ML disordered vacancy phases. The dashed line is the hysteric boundary for oxygen adsorption and desorption. The oxygen coverage is 1.0 ML for  $p(1 \times 1)$  and 0.5 ML for both  $p(2\sqrt{2} \times \sqrt{2})R45^\circ$  and  $c(2 \times 2)$  with 0.25 ML disordered vacancy. (b)  $c(2 \times 2)$  with 0.25 ML disordered vacancy structure. The dashed square indicates the unit cell. The small red spheres are oxygen atoms and big spheres are copper atoms. The topmost copper atoms are colored dark grey. Copyright 2007 The American Physical Society.

Fig. 1.3(a) [34]. Note that the missing-row reconstruction is more stable than other surface structures at temperatures below  $\sim 500$  K. However, for temperatures above  $\sim 500$  K and oxygen partial pressures above  $10^{-7}$  Torr, the missing-row reconstruction transforms into the  $c(2 \times 2)$  with 0.25 ML vacancy disorder structure. The  $c(2 \times 2)$  with 0.25 ML vacancy disorder structure is made by relocating the copper atom between two oxygen atoms to one of the vacancies in the missing row, as shown in Fig. 1.3(b). It was found that the order-disorder transition between the  $(2\sqrt{2} \times \sqrt{2})R45^\circ$  phase and the reconstructed  $c(2 \times 2)$  with 0.25 ML disordered vacancy phase is reversible [34]. They also predicted the two energy barriers involved with the copper atom-vacancy exchange (0.53 eV and 0.56 eV) [34], which are comparable to or less than that of copper (0.53 eV) and oxygen (0.74 eV) diffusion on the clean Cu(100) surface [20]. This result indicates that copper atoms near the missing row are mobile. The order-disorder transition, however, does not fully explain the formation of  $\text{Cu}_2\text{O}$

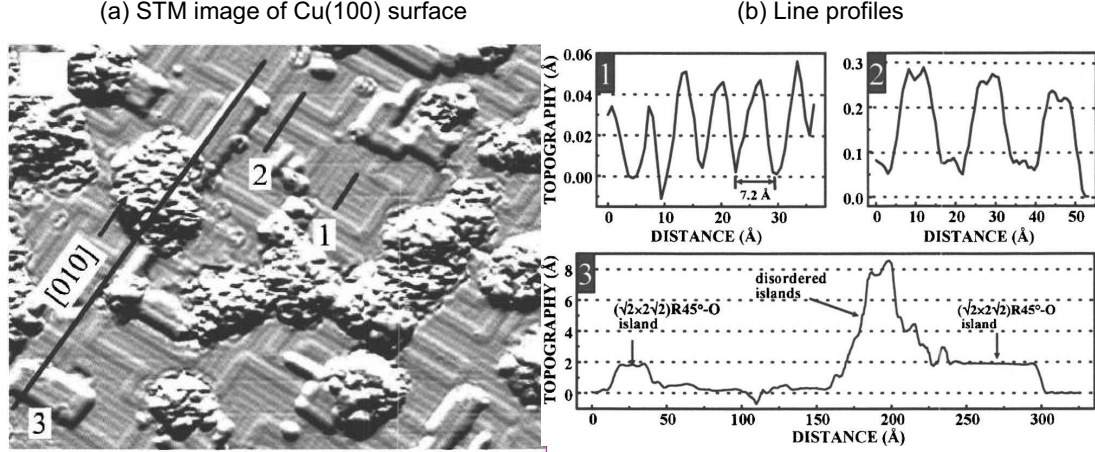


Figure 1.4: (a) Derivative form of scanning tunneling microscope (STM) image of Cu(100) surface after  $9.4 \times 10^5$  L oxygen exposure at 373 K. The area of this STM image is  $400 \times 300 \text{ Å}^2$ . (b) Line profiles 1, 2, and 3 shown from Fig. 1.4(a). Copyright 2007 American Institute of Physics.

on the missing-row reconstructed Cu(100) surface because the vacancy exchange is a horizontal movement while vertical movements of copper and oxygen atoms are required to form the  $\text{Cu}_2\text{O}$  tetrahedral structure.

Lampimäki et al. observed using STM that individual missing-row reconstructions (see line profile 1 in Fig. 1.4) merge to form an ordered domain (see line profile 2 in Fig. 1.4) [37].  $\text{Cu}_2\text{O}$  islands form on these missing-row reconstructed domains, which are elevated  $1.8 \text{ Å}$  (see line profile 3 in Fig. 1.4) [37]. They suggested that the elevated regions form as mobile copper adatoms stick to the phase boundaries between the missing-row reconstruction domains. This mechanism is not sufficient to explain the subsequent oxide-island growth into the substrate, however, as it does not provide a mechanism for oxygen supply to the sub-surface region.

Later, Lahtonen et al. found, using STM and x-ray photoelectron spectroscopy (XPS), that oxygen penetration into the sub-surface region plays an important role in the subsequent formation and growth of  $\text{Cu}_2\text{O}$  islands [38]. Using DFT calculations, Kangas et al. calculated oxygen adsorption energies on the missing-row reconstructed Cu(100) surface for various combinations of on- and sub-surface oxygen atoms and

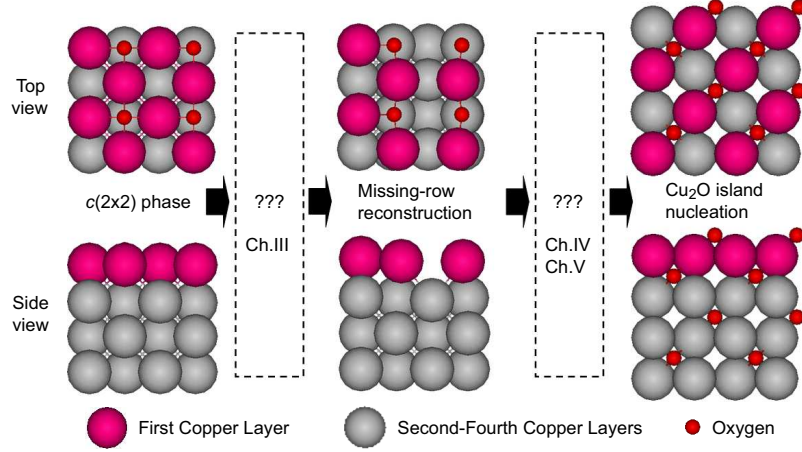


Figure 1.5: Simplified top and side views of structures during the early stages of Cu(100) oxidation.

found that sub-surface oxygen atoms makes the entire system more energetically stable under high oxygen coverages [57]. Kangas and Laasonen later found that oxygen embeds into the sub-surface more easily when there are adsorbed oxygen atoms both on the surface and in the sub-surface [61]. Their unit cell  $[p(2\sqrt{2} \times \sqrt{2})]$ , however, was too small to identify possible  $\text{Cu}_2\text{O}$ -like structures and the transition mechanism from the missing-row reconstructed surface to  $\text{Cu}_2\text{O}$  island nucleation.

### 1.3 Thesis overview and scope

The objective of this thesis research is to identify the transition mechanisms during the early stages of Cu(100) oxidation (see Fig. 1.5) using theory and computation. The primary research tool is density functional theory (DFT), a quantum-mechanical calculation technique for predicting the electronic and structural behavior of many-particle systems. The DFT calculations are performed using the Vienna *ab-initio* simulation package (VASP) [62–66]. The simulation results include the atomic structures of intermediate oxidation states, surface energies for stability comparison, and energy barriers for atomic ejection, diffusion, and embedment events. Where possible, the results are compared to available experimental and/or earlier DFT results.



The remainder of this thesis is organized as follows. In Chapter II, the DFT method is briefly introduced. The adsorption of an oxygen molecule on the Cu(100) surface is discussed and the DFT-predicted atomic structure of the missing-row reconstruction is compared with experimental measurements. In Chapter III, the  $c(2 \times 2)$  to  $(2\sqrt{2} \times \sqrt{2})R45^\circ$  (missing-row reconstruction) transition is investigated using DFT calculations and the nudged elastic band (NEB) method [67]. The energy barriers for potential ejection and subsequent diffusion paths are investigated, including the effects of adatoms, vacancies and the type of movement (i.e., single or multiple atoms).

In Chapter IV, oxygen embedment and sub-surface diffusion are examined [68]. It is found that the oxygen embedment is more probable into the missing-row reconstructed surface compared to the unreconstructed surface and that the diffusion barrier for sub-surface oxygen is comparable to that of oxygen surface diffusion near the missing-row. These results indicate that oxygen embedment and sub-surface diffusion are important mechanisms in the  $(2\sqrt{2} \times \sqrt{2})R45^\circ$  (missing-row reconstruction)- $\text{Cu}_2\text{O}$  nucleation transition. In Chapter V, the missing-row reconstruction to  $\text{Cu}_2\text{O}$  nucleation transition is investigated [69]. Missing-row reconstructed surfaces including extra on- or sub-surface oxygen atoms are relaxed with an additional oxygen molecule to investigate structural and energetic changes. It is found that  $\text{Cu}_2\text{O}$ -like structures are formed only when sub-surface oxygen is present.

To augment the zero-temperature and zero-pressure DFT calculations, phase transitions during the early stages of Cu(100) oxidation are investigated at finite temperatures and pressures in Chapter VI using an *ab-initio* atomistic thermodynamics framework [70]. The stability comparison is done among the missing-row reconstructed surfaces with extra on- or sub-surface oxygen and experimentally observed structures of the early stages of Cu(100) oxidation. The results support our proposed mecha-

nism of the oxygen embedment and sub-surface diffusion for the  $(2\sqrt{2} \times \sqrt{2})R45^\circ$  to  $\text{Cu}_2\text{O}$  transition.

A summary of the research and suggestions for future research directions are presented in Chapter VII.

## CHAPTER II

### DFT-based modeling of unreconstructed and missing-row reconstructed Cu(100) surfaces

#### 2.1 Introduction to density functional theory (DFT)

Density functional theory (DFT) is an *ab-initio* (first principles) calculation method based on quantum mechanics that can be used to investigate the electronic structure of a many-particle system. The quantum state of a physical system is described by the Schrödinger equation [71], which is analogous to Newton's 2nd law in classical physics. For  $N$  particles in a confined space, the Schrödinger equation is a differential equation in  $3N$  variables and there is no exact solution for  $N > 1$ . Hohenburg and Kohn proved that all the properties of a system of interacting electrons can be determined by the ground state electron density, which is a scalar function of the electronic positions [72]. According to the Hohenburg-Kohn theorem, there is a one-to-one mapping between the ground-state electron density and the ground-state wave function of a many-particle system. The electron density that minimizes the total system energy is the true electron density corresponding to the solution of the Schrödinger equation. Kohn and Sham demonstrated that the properties of an inhomogeneous system of interacting electrons can be predicted using the properties of a homogeneous system of non-interacting electrons [73], i.e., by solving the Kohn-Sham equation,

$$\left[ -\frac{\hbar^2}{2m} \nabla^2 + V_{eff}(\mathbf{r}) \right] \Psi_i(\mathbf{r}) = \varepsilon_i \Psi_i(\mathbf{r}). \quad (2.1)$$

Here,  $-\frac{\hbar^2}{2m} \nabla^2$  and  $V_{eff}(\mathbf{r})$  are the kinetic energy operator and effective external potential, and  $\hbar$ ,  $m$ , and  $\mathbf{r}$  are the reduced Planck constant and the mass and position vector of the electron.  $\varepsilon_i$  and  $\Psi_i(\mathbf{r})$  are the energy and the wavefunction of the Kohn-Sham orbital of the  $i$ th electron. For  $N > 1$ , the system is described by a set of coupled Kohn-Sham equations and solved by self-consistent iterations for the wavefunctions,  $\Psi_i(\mathbf{r})$ . The Kohn-Sham equation describes the system using electron-nuclei and electron-electron interactions through  $V_{eff}(\mathbf{r})$ . In the electron-electron interactions, the electron exchange-correlation effect is unknown and an approximation is required for DFT calculations. Typically, DFT calculations apply either the local density approximation (LDA) [73] or the generalized gradient approximation (GGA) [74]. In the case of the LDA, the energy of each electron is predicted from the energy of a uniform electron gas. The GGA includes an additional (correction) term for the gradient of the local electron density and is widely used in the chemistry and condensed matter physics communities. Based on the Hohenburg-Kohn theorem and the Kohn-Sham equation, DFT can be implemented to solve for the electronic structure of condensed-matter phases numerically.

Many software packages exist for performing DFT calculations [64, 75–78]. In this work, the Vienna Ab-initio Simulation Package (VASP) [64] is used. VASP performs *ab initio* quantum mechanical calculations using plane-wave basis sets [65, 66], which are computationally efficient for metals, metal-oxide interfaces, and semiconductors. The VASP calculations presented in this thesis are performed using ultra-soft pseudo potentials with the GGA. The GGA predicts total energies, atomization

energies, energy barriers, and structural energy differences for copper that are in better agreement with experiments and high-level theory (cluster calculations) than the LDA [20, 22, 36, 57, 61]. Spin-averaged calculations are performed for all structural relaxations. In this chapter, the energy cut-off is 300 eV and the  $k$ -point mesh is generated by the Monkhorst-Pack scheme [79]. Further details of the DFT calculations are provided in Chapters III-VI.

## 2.2 O<sub>2</sub> adsorption on a Cu(100) surface

The adsorption of an oxygen molecule on a copper surface is the first step in copper oxidation. The purpose of the work presented in this section is to find the most favorable adsorption site on a Cu(100) surface. On the un-reconstructed Cu(100) surface, we calculate the adsorption energy for six different initial configuration of an oxygen molecule by varying the distance between oxygen atoms and the height from the topmost copper layer. The adsorption state for the minimum adsorption energy is compared to previous DFT calculation results.

The Cu(100) surface that we used in our calculations is shown in Figs. 2.1(a) and 2.1(b). The  $p(3\times 3)$  unit cell is four layers deep (36 total atoms), and there is an 8 Å vacuum in the  $z$ -direction. Periodic boundary conditions (PBC) are applied in the  $x$ - and  $y$ -directions. There is a vacuum region in the  $z$ -direction. The six potential adsorption sites defined by Alatalo et al. were investigated, as shown in Figs. 2.1(a) and 2.1(b) [20]. The big spheres are copper atoms and small spheres are oxygen atoms.

To find the copper lattice constant, a bulk face centered cubic (fcc) structure was initially modeled with a  $13\times 13\times 13$   $k$ -point mesh. The zero-pressure bulk lattice constant is obtained by determining where the total system energy is minimized,

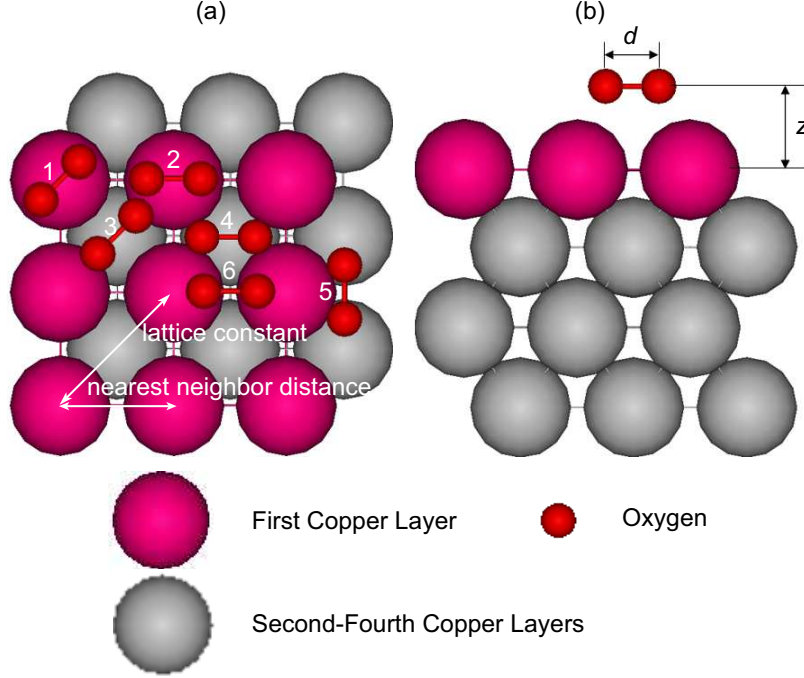


Figure 2.1:  $p(3\times 3)$  Cu(100) surface. The narrow lines between copper atoms are created by the visualization program and have no physical meaning. (a) Top view. Oxygen molecule adsorption sites: top sites (1-2), fcc sites (3-4) and bridge sites (5-6). (b) Side view.  $d$  is the bond length and  $z$  is the height between the center of mass of the oxygen molecule and the surface copper atoms.

as shown in Fig. 2.2(a). We obtain a value of  $3.65 \text{ \AA}$ , which is larger than the experimentally measured value of  $3.60 \text{ \AA}$  [80–82] but is consistent with previous DFT calculations [20, 83]. The  $p(3\times 3)$  copper surface structure is then built based on this lattice constant. The copper surface is first relaxed at fixed volume without the oxygen molecule. The relaxed structure is then used in single-point total system energy calculations with an oxygen molecule. To minimize the computational effort for the surface structure, we would like to use as coarse a  $k$ -point mesh as possible. The mesh must be fine enough, however, to predict mesh-independent results. To find a suitable mesh,  $k$ -point meshes between  $1\times 1\times 1$  and  $9\times 9\times 1$  were investigated for the surface structure, as shown in Fig. 2.2(b). As the number of  $k$ -points increases, the total system energy also increases and converges to  $-124.5 \text{ eV}$  after the  $3\times 3\times 1$  mesh. The energy difference between the  $3\times 3\times 1$  and  $9\times 9\times 1$   $k$ -point mesh is  $0.005$

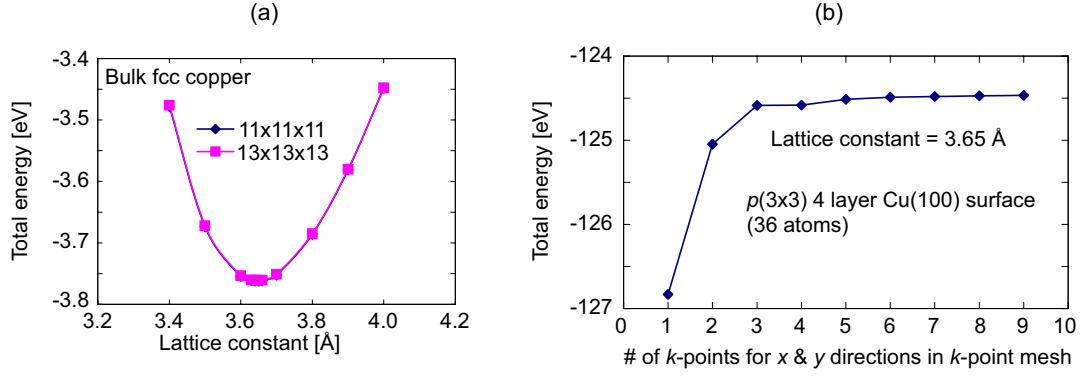


Figure 2.2: (a) Determining the zero-pressure bulk fcc lattice constant. (b) Finding the optimum number of  $k$ -points for the surface calculations.

eV, and so the  $3 \times 3 \times 1$  mesh is chosen for all single point energy calculation for the surface structure.

For the single point energy calculations, the distance between the two oxygen atoms ( $d$ ) and the height ( $z$ ) of the molecule from the copper surface are varied from 1.0 Å to 2.4 Å by 0.2 Å increments. 1.21 Å is used for  $d$  instead of 1.2 Å because that is the oxygen bond length at equilibrium [84,85] measured by experiment. There are thus 64 ( $=8 \times 8$ ) calculations for each adsorption site and the total number of calculations is 384. The oxygen molecule can be modeled in a horizontal or vertical configuration. The horizontal configurations are shown in Figs. 2.1(a) and 2.1(b). In the vertical configuration, the molecular bond is perpendicular to the surface plane. In previous DFT calculations, the adsorption energy was investigated for both the horizontal and vertical configurations [16,17,20]. The horizontal configuration was found to be more energetically stable than the vertical configuration, and no dissociation was predicted in the vertical configuration. Therefore, only the horizontal configuration is studied here.

Table 2.1: The minimum adsorption energy and its associated distance ( $d$ ) between the two oxygen atoms and height ( $z$ ) above the copper surface. The sites are defined in Fig. 2.1(a). Atomic or molecular oxygen adsorption is identified by using “2O” or “O<sub>2</sub>”.

Site	$d$ [Å]	$z$ [Å]	$E_{ads}$ [eV]	2O or O <sub>2</sub>
1	2.4	1.2	-1.16	2O
2	2.4	1.2	-1.14	2O
3	1.4	1.6	-1.06	O <sub>2</sub>
4	1.6	1.4	-1.46	O <sub>2</sub>
5	2.4	1.0	-1.99	2O
6	1.4	1.8	-1.08	O <sub>2</sub>

The adsorption energy is calculated from [57]

$$E_{ads} = \frac{E_{O/Cu} - E_{Cu} - N_O \cdot \frac{E_{O_2}}{2}}{N_O}, \quad (2.2)$$

where  $E_{O/Cu}$  is the total system energy of the oxygen-covered copper surface,  $E_{Cu}$  is the energy of the clean copper surface,  $E_{O_2}$  is the energy of an isolated oxygen molecule, and  $N_O$  is the number of oxygen atoms in the computational cell. The minimum adsorption energy on each site is listed in Table 2.1. The adsorption energy is minimized when the oxygen molecule (or its dissociated oxygen atoms) are adsorbed at a four-fold hollow site [see Figs. 2.3(a)]. The configuration of the oxygen atoms in the second lowest energy adsorption site is shown in Fig. 2.3(b). The lowest adsorption energy is found at the initial position of bridge site (site 5) with  $d = 2.4$  Å and  $z = 1.0$  Å, corresponding to atomic oxygen adsorption on two four fold hollow sites. This result is consistent with experiment [60] and previous DFT calculations [20]. The lowest adsorption energy is 0.31 eV lower than the -1.68 eV value calculated by Alatalo et al., who also found the four fold hollow site to be the most favorable adsorption site [20]. We believe that this difference is a result of different unit cell and vacuum sizes and the convergence criteria (this information is not provided by Alatalo et al.).



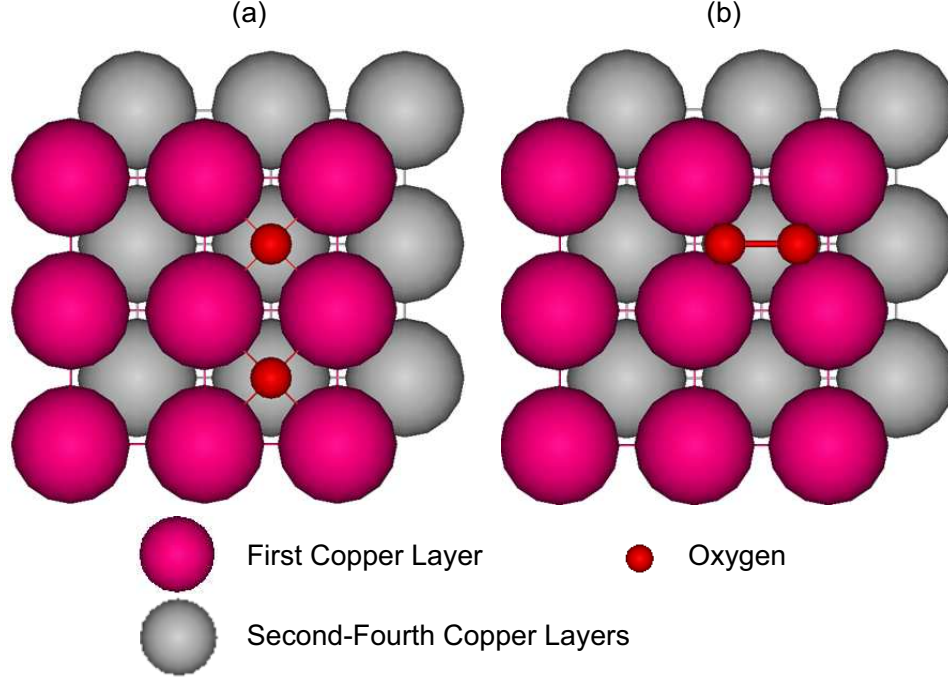


Figure 2.3: (a) Site 5 adsorption state. The oxygen molecule is fully dissociated and two oxygen atoms are adsorbed at fcc hollow sites, which are the most favorable adsorption sites on Cu(100) surface. (b) Site 4 adsorption state. The oxygen-oxygen bond is elongated but not dissociated yet (i.e., molecular oxygen adsorption). See Table 2.1 for the adsorption energy for each state.

### 2.3 Structural comparison of missing-row reconstruction between DFT-predictions and experimental measurements

As a preliminary work, we investigated the energetics and morphologies of unreconstructed  $[c(2 \times 2)]$  and missing-row reconstructed  $[(2\sqrt{2} \times \sqrt{2})R45^\circ]$  Cu(100) surfaces using DFT calculations. This comparison will show the structural differences before and after the reconstruction. The unreconstructed and reconstructed surfaces are first relaxed and then the structural parameters shown in Fig. 2.4 [30] are measured and provided in Table 2.2. The  $p(2 \times 2)$  and  $p(2\sqrt{2} \times \sqrt{2})$  unit cells including five copper layers are used and the oxygen coverage is 0.5 ML. The bottom copper layer is fixed and the other copper layers and the oxygen atoms can move during the structural relaxation.

The relaxed structures are shown in Figs. 2.5(a)-(d). The surface copper atoms

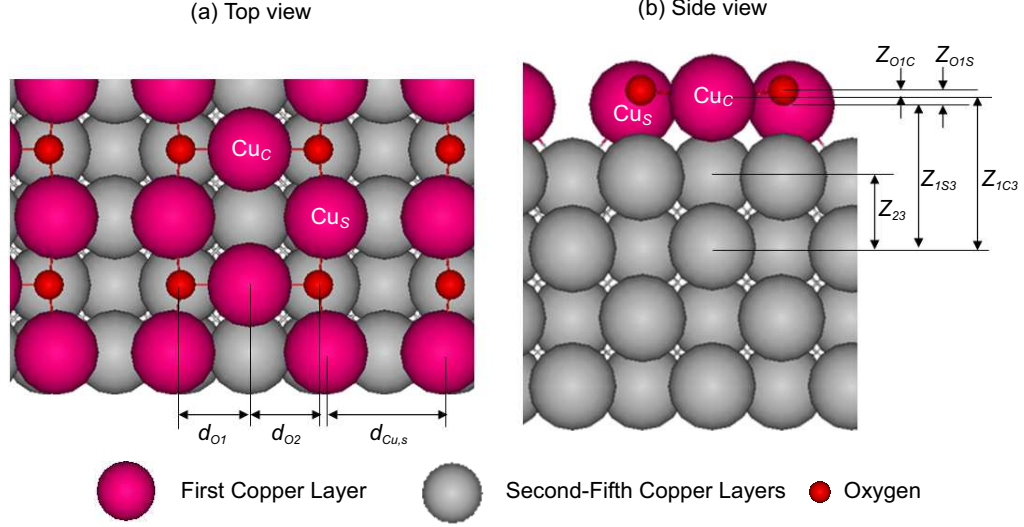


Figure 2.4: Structural parameters of the Cu(100) reconstructed (missing row) surface at 0.5 ML coverage. (a) Distances between copper and oxygen atoms. (b) Vertical distances between oxygen atoms and copper layers. The values for these parameters are provided in Table 2.2.

Table 2.2: Comparison of relaxed structural parameter values between the unreconstructed and reconstructed (missing-row reconstruction) Cu(100) surfaces at an oxygen coverage of 0.5 ML calculated by DFT.

	$d_{Cu,S}$ [Å]	$d_{O1}$ and $d_{O2}$ [Å]	$z_{23}$ [Å]	$z_{1C3}$ [Å]	$z_{O1C}$ [Å]
Unreconstructed	3.65	1.83	1.80	3.71	0.73
Reconstructed	3.17	1.87	1.81	3.88	0.21

are missing in every fourth row in the missing-row reconstruction. In Figs. 2.5(b) and 2.5(d), some of the copper atoms are located at the step-edges next to the missing row. The subscript “S” is used for the structural parameters related to these copper atoms ( $Cu_S$ ). Likewise, “C” is used to identify the structural parameters related to the topmost copper atoms ( $Cu_C$ ), which are located between the copper atoms at the step-edges.

The structural parameters measured from the relaxed structures are provided in Table 2.2. The distances between the oxygen and copper atoms ( $d_{O1}$  and  $d_{O2}$ ) for the reconstructed surface are slightly bigger than those of the unreconstructed surfaces. The interatomic distance between the copper atoms at the step-edge ( $d_{Cu,S}$ ) is smaller on the reconstructed surface compared to the unreconstructed surface. The inter-layer

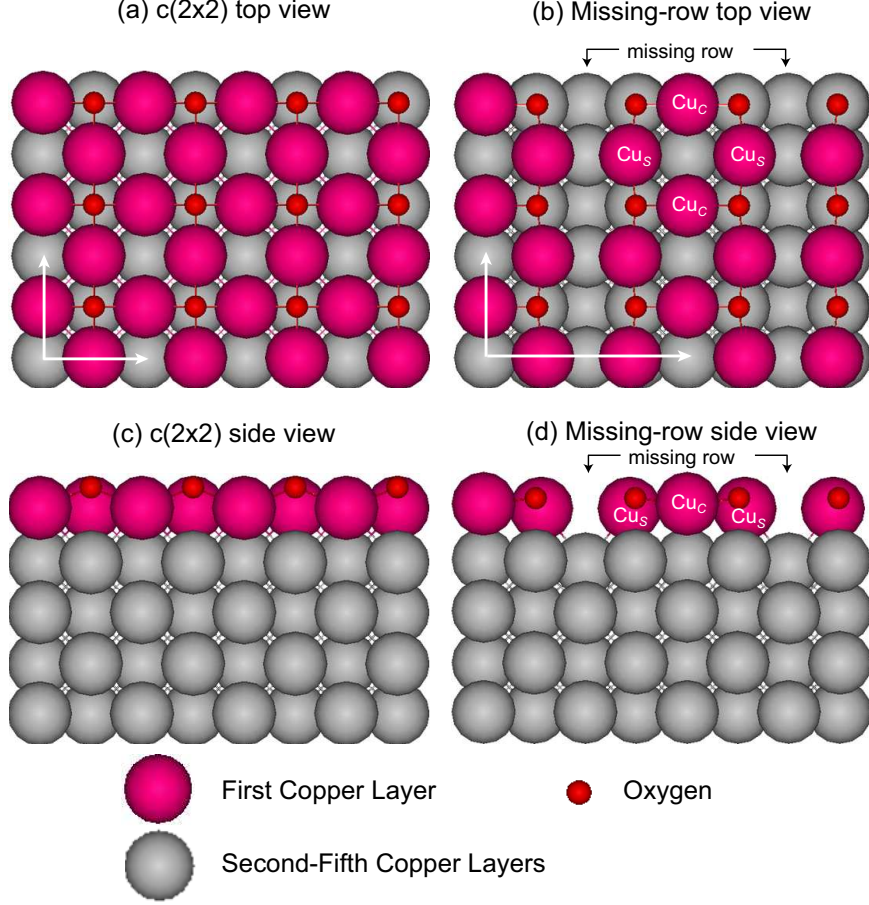


Figure 2.5: Comparison between unreconstructed and reconstructed structures on the Cu(100) surface. The arrows indicate the size of the unit cell. (a) Relaxed  $c(2 \times 2)$  structure, top view. (b) Relaxed missing-row reconstruction  $[(2\sqrt{2} \times \sqrt{2})R45^\circ]$ , top view. (c)  $c(2 \times 2)$  structure, side view. (d) Relaxed missing-row reconstruction  $[(2\sqrt{2} \times \sqrt{2})R45^\circ]$ , side view.

distances ( $z_{1C3}$  and  $z_{23}$ ) indicate that the topmost copper layer of the missing-row reconstruction moves 0.17 Å upward (see  $z_{1C3}$ ). The upward movement does not significantly affect the height difference between the second and third copper layers (see  $z_{23}$ ). The vertical position of the copper atoms at the step-edges ( $\text{Cu}_S$ ) is lower than that of the copper atoms located between the copper atoms at the step-edge ( $\text{Cu}_C$ ). The difference of  $z_{O1C}$  between the unreconstructed and reconstructed surfaces is 0.52 Å. This result indicates that the oxygen atoms move down 0.52 Å during the missing row-reconstruction. This downward movement is consistent with previous *ab initio* calculations [27]. Based on this observation, the missing-row reconstruction

Table 2.3: Comparison between the structural parameter values for the reconstructed (missing-row reconstruction) Cu(100) surface at an oxygen coverage 0.5 ML from DFT calculations and experimental results (PhD: photoelectron diffraction, LEED: low energy electron diffraction).

	$d_O$ [Å]	$z_{23}$ [Å]	$z_{1S3}$ [Å]	$z_{1C3}$ [Å]	$z_{O1S}$ [Å]	$z_{O1C}$ [Å]
DFT	0.04	1.81	3.72	3.88	0.37	0.21
PhD [30]	0.04 +0.04/-0.08	1.83 +0.30/-0.20	3.71 +0.30/-0.20	3.97 $\pm 0.30$	0.17 $\pm 0.10$	0.09 +0.16/-0.19
LEED [25]	0.00	1.84	3.88	3.78	0.10	0.20

makes the topmost copper layer move upward and the oxygen atoms move downward to get to an energetically stable structure. This finding is consistent with what has been observed in experiments [25, 30].

The structural parameters of the DFT-predicted missing-row reconstruction are compared to experimental results in Table 2.3. The distance between (i) the second and third copper layers ( $z_{23}$ ), (ii) the topmost copper atom at the step-edge and third copper layer ( $z_{1S3}$ ), and (iii) the topmost copper atom ( $\text{Cu}_C$ ) and third copper layer ( $z_{1C3}$ ) are comparable to the experimental results [25, 30]. The vertical distance between an oxygen atom and a  $\text{Cu}_S$  atom ( $z_{O1S}$ ) is overestimated with respect to experiment, but that of the oxygen atom to  $\text{Cu}_C$  ( $z_{O1C}$ ) is consistent with experimental results. Hence, the missing-row reconstruction structure predicted by DFT is comparable to the experimental results and we believe that the DFT method can be used for further investigation of the oxidation process.

## 2.4 Summary

This chapter began with a discussion about the primary tool of this thesis research, DFT calculations. In Section 2.2, oxygen molecule adsorption on the Cu(100) surface was investigated. It was found that the most stable oxygen covered Cu(100) surface has oxygen atoms adsorbed at the four-fold hollow sites. In Section 2.3, structural differences between the  $c(2 \times 2)$  phase and the missing-row reconstruction were first

compared. Then, the structural parameters of the missing-row reconstruction predicted by DFT were compared to those from experiments and reasonable agreement was found. In the next Chapter, the  $c(2\times 2)$ -missing-row reconstruction transition will be investigated.

## CHAPTER III

### **Energetics and kinetics of the $c(2 \times 2)$ to $(2\sqrt{2} \times \sqrt{2})R45^\circ$ transition on the Cu(100) surface**

#### **3.1 Introduction**

As discussed in Chapter I, during the early stages of Cu(100) oxidation, the  $c(2 \times 2)$  phase is experimentally observed to transition into the  $(2\sqrt{2} \times \sqrt{2})R45^\circ$  phase by a missing-row reconstruction at an oxygen coverage of around 0.5 monolayers (ML) [14, 15, 23–31]. Based on their scanning tunneling microscopy (STM) observations, Jensen et al. proposed that the missing row forms by the ejection of every fourth row of the top copper layer [26]. This mechanism has been supported by experimental and computational investigations [14, 28–36, 38, 68, 69]. The stabilities of the  $c(2 \times 2)$  and  $(2\sqrt{2} \times \sqrt{2})R45^\circ$  phases at an oxygen coverage of 0.5 ML have been compared using density functional theory (DFT)-predicted chemisorption energies, average oxygen binding energies per oxygen atom, and surface-oxide energies [33, 36, 68, 69]. The  $(2\sqrt{2} \times \sqrt{2})R45^\circ$  phase is consistently found to be more stable than the  $c(2 \times 2)$  phase, but the energy differences are small (e.g., 0.1 eV for the average oxygen binding energy [36]). Iddir et al. used *in situ* surface x-ray scattering to investigate the stability of oxygen-covered Cu(100) surface phases for temperatures between 300 and 1000 K and oxygen partial pressures between  $10^{-10}$  and  $10^{-4}$  Torr [34]. They found that the

reconstructed phases  $[(2\sqrt{2} \times \sqrt{2})R45^\circ$  and a related phase that has disordered copper surface vacancies] are more stable than unreconstructed phases at oxygen partial pressures higher than  $10^{-8}$  Torr. They also found that the transition between the unreconstructed phases and the reconstructed phases is hysteretic [34]. Later, Duan et al., using *ab-initio* atomistic thermodynamics, confirmed that the reconstructed phases are more stable than the unreconstructed phases (clean and 0.25 ML oxygen covered surfaces) in the same range of oxygen partial pressure [36].

Two driving forces for the missing-row reconstruction have been suggested: (i) surface stress [14, 32] and (ii) long-range Coulombic interactions [31]. Harrison et al. found that the compressive stress on the  $c(2 \times 2)$  phase is larger than that on the  $(2\sqrt{2} \times \sqrt{2})R45^\circ$  phase from both experiments (crystal curvature technique in an ultra-high vacuum chamber) and DFT calculations [32]. Using temperature-dependent surface-extended x-ray-absorption fine structure measurements, Lederrer et al. also studied the  $c(2 \times 2)$  and  $(2\sqrt{2} \times \sqrt{2})R45^\circ$  phases [14]. They found that adsorbate-induced forces between substrate copper atoms in the  $c(2 \times 2)$  phase induce surface strains and lead to the missing-row reconstruction. They also found that the copper-oxygen bond is ionic on the unreconstructed surface but covalent on the missing-row reconstructed surface. Calculating surface Madelung potentials within the muffin-tin approximation, Stolbov et al. showed that long-range Coulombic interactions among oxygen atoms of the  $c(2 \times 2)$  phase make copper atoms eject leading to the  $(2\sqrt{2} \times \sqrt{2})R45^\circ$  phase, which has stronger  $pO-dCu$  covalent coupling [31]. Based on these findings, we hypothesize that long-range Coulombic interactions induce a compressive surface stress, leading to the ejection of the atoms of every fourth row of the top copper layer.

While the driving forces behind the missing-row reconstruction have been in-

investigated, three fundamental questions remain. First, is the missing-row reconstruction necessary for Cu(100) oxidation? Previous investigations showed that the  $(2\sqrt{2} \times \sqrt{2})R45^\circ$  phase is more stable than the  $c(2 \times 2)$  phase, but did not show whether  $\text{Cu}_2\text{O}$  can form on unreconstructed Cu(100) surfaces without the missing-row reconstruction [33, 36, 69]. This question will be addressed in Chapter V. Second, how do the copper atoms eject and diffuse away during the missing-row reconstruction? The transition kinetics from the  $c(2 \times 2)$  phase to the  $(2\sqrt{2} \times \sqrt{2})R45^\circ$  phase are not well understood. Third, where do the ejected copper atoms go? Based on STM measurements, it was suggested that the ejected copper atoms diffuse away from the missing row and attach on top of adjacent missing-row reconstructed surfaces [37] and/or step edges in phase boundaries [38]. The diffusion paths, however, are unknown.

Here, we will focus on the second question by investigating the  $c(2 \times 2)$  to  $(2\sqrt{2} \times \sqrt{2})R45^\circ$  transition using DFT calculations. In Section 3.2, the computational unit cells, set-up, and procedures are presented. In Section 3.3, we predict the energy barriers for copper atom ejection and diffusion during the  $c(2 \times 2)$  to  $(2\sqrt{2} \times \sqrt{2})R45^\circ$  transition. The results are used to propose a mechanism by which the missing row reconstruction occurs. To address the third questions, modeling techniques that can access longer length and time scales are required. One candidate technique, Kinetic Monte Carlo simulation, is briefly discussed in Chapter VII.

### 3.2 Calculation methodology

We perform the DFT calculations using the Vienna Ab-initio Simulation Package (VASP) [62–66], which uses a plane-wave basis set [64, 66]. We use ultra-soft pseudo potentials, the PW91 generalized gradient approximation [86], and apply a 350 eV energy cutoff. The  $p(2 \times 2)$ ,  $p(2\sqrt{2} \times \sqrt{2})$ ,  $p(2\sqrt{2} \times 2\sqrt{2})$ , and  $p(4 \times 4)$  unit cells were



initially considered. To minimize non-physical size effects, we report only the results from the  $p(4\times 4)$  unit cell. All slab structures include 5 layers (the bottom layer is fixed) and the vacuum size is 11 Å. There are 81 copper and 8 oxygen atoms in the  $p(4\times 4)$  unit cell, the biggest that we consider. The  $k$ -point mesh is generated by the Monkhorst-Pack scheme [79]. We use an  $8\times 16\times 1$  mesh for the  $p(2\sqrt{2}\times\sqrt{2})$  unit cells, an  $8\times 8\times 1$  mesh for the  $p(2\times 2)$  and  $p(2\sqrt{2}\times 2\sqrt{2})$  unit cells, and a  $6\times 6\times 1$  mesh for the  $p(4\times 4)$  unit cells. The  $k$ -points meshes, the energy cutoff, and the number of copper layers are chosen based on convergence tests performed for the  $p(2\sqrt{2}\times 2\sqrt{2})$  missing-row reconstructed surface, which are discussed in Chapter V.

To investigate the ejection of copper atoms and their subsequent diffusion during the  $c(2\times 2)$  to  $(2\sqrt{2}\times\sqrt{2})R45^\circ$  transition, the climbing image nudged elastic band (NEB) method is applied [87–90]. The NEB method is a computational approach for finding the minimum energy path between specified initial and final equilibrium states. To specify the initial and final states, separate single-point DFT calculations are performed to ensure relaxed structures. We use five images between the initial and final states.

### 3.3 $c(2\times 2)$ to $(2\sqrt{2}\times\sqrt{2})R45^\circ$ transition

#### 3.3.1 Copper atom ejection

To investigate the energetics and kinetics of the copper ejection, we will propose a set of potential paths and then compare their energy barriers. The initial (A) and final positions (B, C, and D) of the copper atom in the three possible ejection paths are shown in Figs. 3.1(a) and 3.1(b) for the  $p(4\times 4)$  unit cell. Relaxed configurations of these structures are used in the NEB calculations. The energetics of the ejection of the first copper atom from a perfect  $c(2\times 2)$  surface are shown in Fig. 3.2. The energy

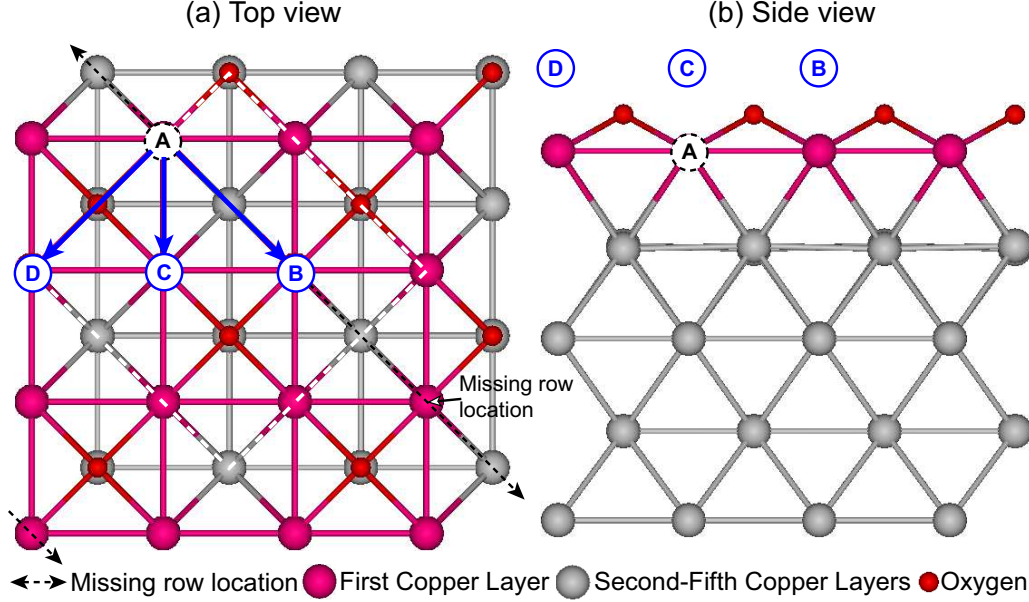


Figure 3.1: (a) Top view and (b) Side view of the  $p(4\times 4)$  unit cell showing the initial (A) and final positions (B, C, and D) for the ejection at the first copper atom. For reference, the  $p(2\sqrt{2}\times 2\sqrt{2})$  unit cell is contained by the white dashed lines.

barriers are comparable, ranging from 1.92 eV ( $A\rightarrow B$ ) to 2.12 eV ( $A\rightarrow D$ ). We note that the B site lies on what would be the missing row. The only relevant next event is therefore a diffusion to C or D, which is discussed in Section 3.3.2. These barriers are comparable to the activation energy of  $\text{Cu}_2\text{O}$  formation on the  $\text{Cu}(100)$  surface ( $1.4\pm 0.2$  eV/atom) [91] and to the activation energy for Ag on the Ag 1ML/Mo(100) surface (2.5 eV/atom) [92].

Once one copper atom has been ejected, the question arises as to what happens next. Does a second copper atom eject while the first is still nearby? Or, does the first atom diffuse away and then the second atom ejects? Or, can two copper atoms eject at the same time? We investigated these possibilities using the ejection paths shown in Figs. 3.3(a)[ejection with vacancy and adatom (w/ V&Ad)], 3.3(b)[ejection with vacancy (w/ V)], and 3.3(c)[coordinated ejection ( $\times 2$ )]. The energy barriers are provided in Table 3.1. The energy barriers of all the  $A\rightarrow D$  paths are similar (i.e., they are not affected by the vacancy or the adatom). When the first ejected copper atom

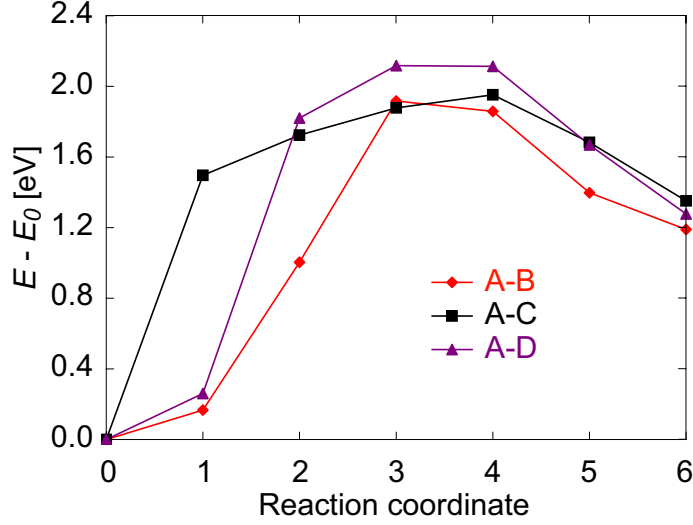


Figure 3.2: Energetics of copper ejection on the  $p(4\times 4)$  unit cell ( $E$  = image energy,  $E_0$  = energy of image 0). The initial (A) and final positions (B, C, and D) of each path are shown in Figs. 3.1(a) and 3.1(b).

stays at the C site and the second copper atom ejects ( $A \rightarrow C$  w/ V&Ad), however, the energy difference between the initial and final state ( $E_{diff}$ ) is 0.62 eV, which is smaller than that of first ejection (1.35 eV), and the energy barrier decreases by 0.54 eV. While the first ejected copper atom may diffuse away, the energy barrier for the ejection of a second copper atom to the C site in the presence of a vacancy is still lower than that of the first one. These results suggest that once one copper atom is ejected, many copper atoms will soon follow. The ejection of an entire row is consistent with experimental observations [23, 25–27].

The coordinated and non-coordinated ejections lead to the same final structure. As shown in Figs. 3.4(a) and 3.5(a), there are two energy barriers for the non-coordinated ejection and one energy barrier for the coordinated ejection. To determine which event is more probable, we use transition state theory, TST, a theoretical method for calculating the transition rate between two equilibrium states using thermodynamics, kinetic theory, and statistical mechanics [93, 94]. The transition rate can be calculated

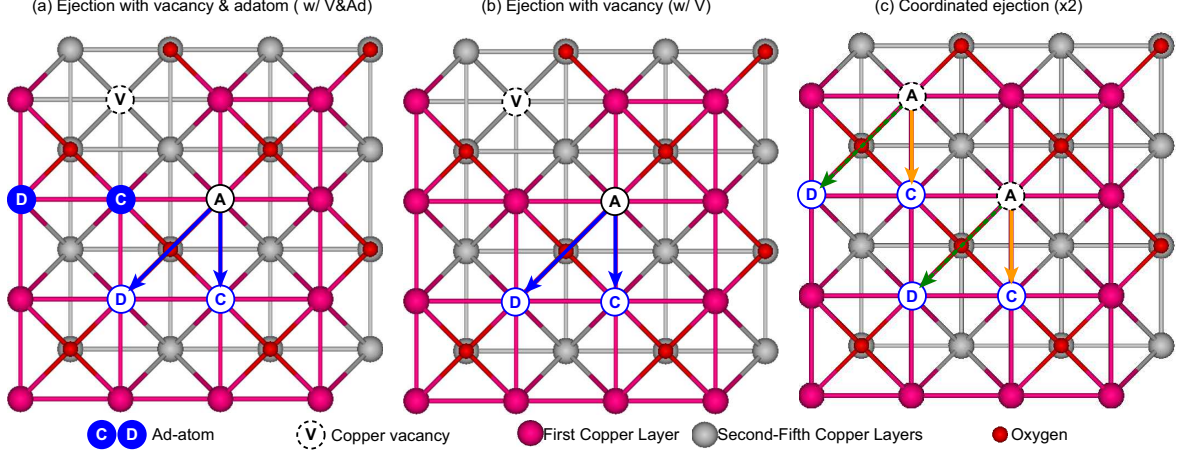


Figure 3.3: Three possibilities for the second copper ejection: (a) with vacancy and adatom (w/ V&Ad), (b) with vacancy (w/ V), and (c) coordinated ejection (two neighboring copper atoms eject at the same time,  $\times 2$ ). The energy barriers are provided in Table 3.1.

Table 3.1: Energy difference,  $E_{diff}$ , and energy barrier,  $E_{barrier}$ , for the copper ejection paths shown in Figs. 3.1(a), 3.3(a), 3.3(b), 3.3(c), 3.4(a), and 3.5(a).

Index	$E_{diff}$ [eV]	$E_{barrier}$ [eV]
A $\rightarrow$ B	1.19	1.92
A $\rightarrow$ C	1.35	1.95
A $\rightarrow$ C w/ V&Ad	0.62	1.41
A $\rightarrow$ C w/ V	1.58	1.66
(A $\rightarrow$ C) $\times 2$	1.97	2.47
A $\rightarrow$ D	1.28	2.12
A $\rightarrow$ D w/ V&Ad	1.33	2.03
A $\rightarrow$ D w/ V	1.28	2.12
(A $\rightarrow$ D) $\times 2$	2.60	3.23

under the harmonic approximation as

$$k_{path}^{TST,H} = \nu_o \cdot \exp \left[ -\frac{E_{barrier}}{k_B T} \right], \quad (3.1)$$

where  $\nu_o$ ,  $k_B$ ,  $T$ , and  $E_{barrier}$  are the atomic vibrational frequency, the Boltzmann constant, and temperature [95]. In Eq. (3.1),  $\nu_o$  is taken to be  $1.0\text{E}+13$  [1/s], the typical frequency of an atomic vibration [96]. The transition rates of the non-coordinated (A $\rightarrow$ C and A $\rightarrow$ C w/ V&Ad) and coordinated [(A $\rightarrow$ C) $\times 2$ ] ejections are  $k_{A\rightarrow C}^{TST,H} \cdot k_{A\rightarrow C \text{ w/V\&Ad}}^{TST,H}$  and  $k_{(A\rightarrow C)\times 2}^{TST,H}$ . The transition rates for the coordinated and non-

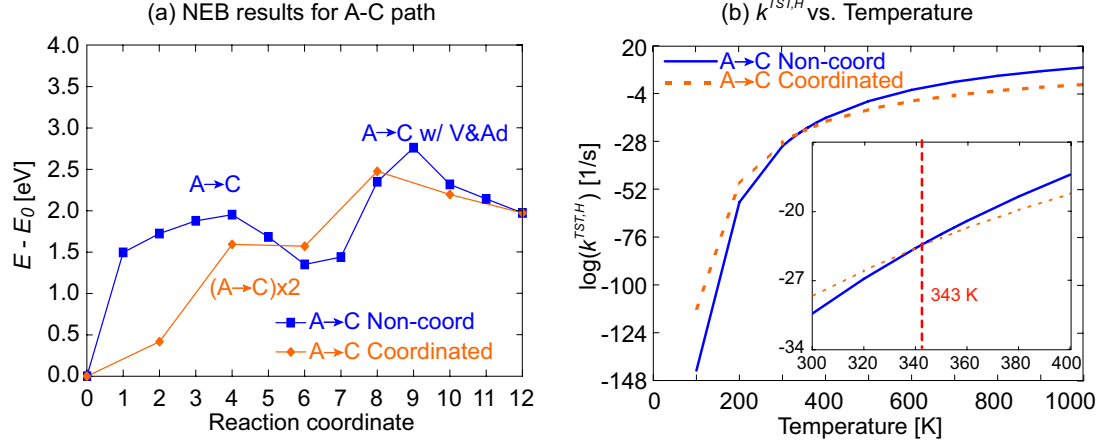


Figure 3.4: Comparing the energetics of coordinated and non-coordinated copper atom ejection for the A→C path. (a) Reaction pathway. (b) Transition rates vs. temperature. The energy barriers are provided in Table 3.1. In Eq. (3.1),  $\nu_o$  is taken to be  $1.0\text{E}+13$  [1/s], the typical frequency of an atomic vibration. The non-coordinated ejection is more probable than the coordinated ejection at temperatures higher than 343 K [vertical dashed line in Fig. 3.4(b)]

coordinated A→C and A→D ejection paths are plotted vs. temperature between 100 and 1000 K in Figs. 3.4(b) and 3.5(b). The probable ejection changes from the coordinated ejection to the non-coordinated ejection at 343 K for the A→C paths and at 356 K for the A→D paths [see vertical dashed lines in Figs. 3.4(b) and 3.5(b)]. These temperatures can be calculated using Eq. (3.1), when the transition rate of the coordinated ejection [i.e.,  $k_{(A\rightarrow C)\times 2}^{TST,H}$ ] is equal to that of the non-coordinated ejection (i.e.,  $k_{A\rightarrow C}^{TST,H} \cdot k_{A\rightarrow C\text{ w/V\&Ad}}^{TST,H}$ ). The available experimental observations about Cu(100) oxidation are all done at temperatures higher than 450 K [23,26,34,40]. Our results suggest that the missing-row reconstruction observed in these experiments is produced by the non-coordinated ejection.

Based on the results presented in this section, we believe that the missing row forms through A→C ejections that take place because of lower energy barrier induced by copper adatom and vacancy effects. In the next section, we will investigate the subsequent diffusion process.

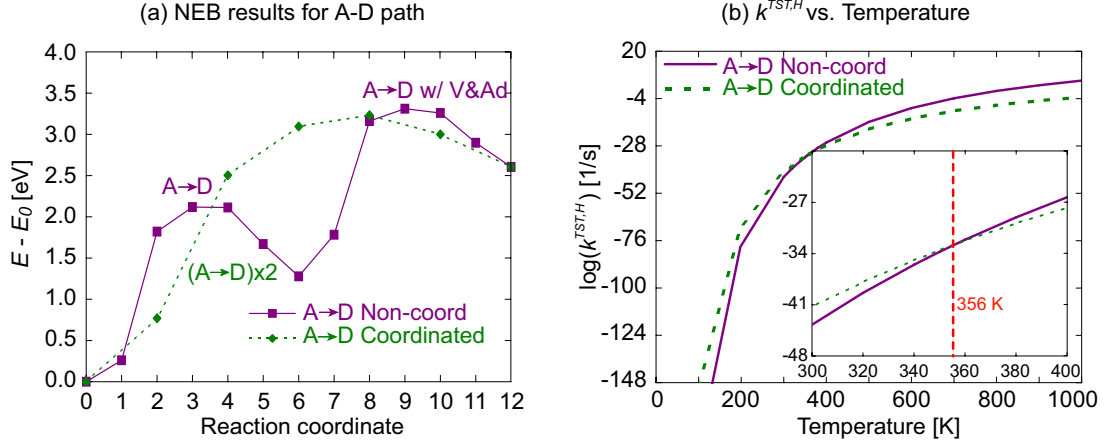


Figure 3.5: Comparing the energetics of coordinated and non-coordinated copper atom ejection for the A→D path. (a) Reaction pathway. (b) Transition rates vs. temperature. The energy barriers are provided in Table 3.1. In Eq. (3.1),  $\nu_o$  is taken to be  $1.0\text{E}+13$  [1/s], the typical frequency of an atomic vibration. The non-coordinated ejection is more probable than the coordinated ejection at temperatures higher than 356 K [vertical dashed line in Fig. 3.5(b)]

### 3.3.2 Copper atom diffusion away from the missing-row

To study the copper diffusion that will follow the copper ejection, we define NEB paths starting at the C sites, the final positions of the probable ejection paths found in Section 3.3.1. To investigate the diffusion following the A→C then A→C w/ V&Ad ejections [see Fig. 3.3 and Table 3.1] there are four diffusion paths (C1→I, C1→II, C2→II, C2→III), as shown in Fig. 3.6(a). We investigated the C2→I path but found that the copper adatom at the C1 site returned to V1 because of the periodicity of the computational cell. Because the ejection barriers for the first ejection are comparable for all three paths [see Fig. 3.2 and Table 3.1], we also investigated diffusion from the B and D sites. As shown in Fig. 3.6(b), there are four distinct diffusion paths (B→B, B→C, B→D, and D→C). Note that D→D and D→B are equivalent to B→B and B→D. We also investigated copper diffusion on the perfect  $c(2\times 2)$  phase as shown in Fig. 3.6(c) (paths  $\alpha$ ,  $\beta$ , and  $\gamma$ ). The predicted energy differences and energy barriers for all these diffusion events are presented in Table 3.2.

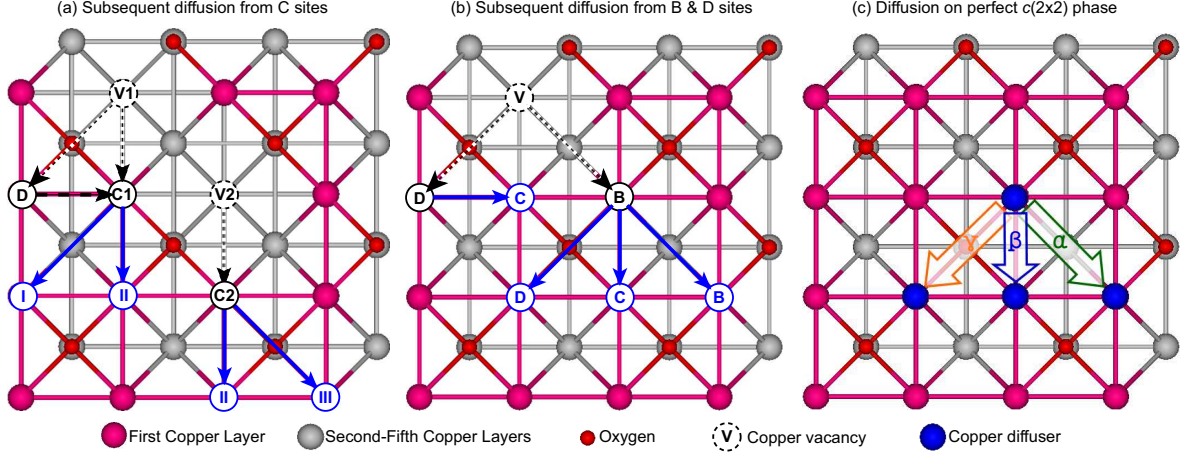


Figure 3.6: Copper diffusion paths following the copper ejection from (a) C sites and (b) B and D sites. “V” is the copper vacancy, which is the original location of the ejected copper atom. The dashed arrows are the ejection paths and the solid arrows are the diffusion paths. The “B” and “D” sites (black) are the initial positions and “B”, “C”, “D”, “I”, “II”, and “III” (blue) are final positions]. (c) Copper diffusion paths on the perfect  $c(2\times 2)$  phase. Path  $\gamma$  is over an oxygen atom. There is no oxygen atom along path  $\alpha$ .

The barriers from the C sites are 0.36-1.44 eV smaller than the ejection barriers (see Table 3.1). To increase the probability of the second copper ejection, as discussed in Section 3.3.1, a copper atom needs to be at a C site. The energy barriers of the  $B\rightarrow C$  and  $D\rightarrow C$  diffusions are smaller than all the ejection barriers and the other diffusion barriers [see Tables 3.1 and 3.2], such that there is a source of atoms available to promote further ejection.

If we ignore the copper vacancy [V in Fig. 3.6(b)], the  $B\rightarrow B$ ,  $B\rightarrow C$ , and  $B\rightarrow D$  paths are equivalent to the  $\alpha$ ,  $\beta$ , and  $\gamma$  paths [see Figs. 3.6(b) and 3.6(c)]. The energy barriers for  $B\rightarrow B$ ,  $B\rightarrow C$ , and  $B\rightarrow D$  are comparable to those for the  $\alpha$ ,  $\beta$ , and  $\gamma$  paths. As discussed in Section 3.3.1, the vacancy affects the ejection energetics. The vacancy, however, does not affect copper diffusion away from it, suggesting that the spatial extent of its effect is less than 4 Å.

On the perfect  $c(2\times 2)$  phase, the  $\beta$  path has the smallest barrier. The energy barriers for the  $B\rightarrow C$  and  $\beta$  paths are comparable to copper diffusion barriers on the

Table 3.2: Energy difference,  $E_{diff}$ , and energy barrier,  $E_{barrier}$ , for copper diffusion paths during the transition from the  $c(2\times 2)$  to the missing-row reconstructed Cu(100) surface. The copper diffusion paths are shown in Figs. 3.6(a) and 3.6(b) for diffusion following the copper ejection and in Fig. 3.6(c) for diffusion on the perfect  $c(2\times 2)$  phase.

Path	$E_{diff}$ [eV]	$E_{barrier}$ [eV]
C1→I	0.58	0.99
C1→II	-0.59	0.41
C2→II	0.72	0.87
C2→III	0.33	1.52
D→C	0.07	0.56
B→B	0.09	0.64
B→C	-0.13	0.52
B→D	0.00	0.97
on perfect $c(2\times 2)$ phase		
$\alpha$	0	0.63
$\beta$	0	0.55
$\gamma$	0	0.74

clean Cu(100) surface measured from experiment ( $0.36\pm 0.03$  eV) [92] and predicted from a previous DFT study (0.53 eV). [20] This result indicates that the mobility of a copper adatom near the missing row is similar to that on the clean and  $c(2\times 2)$  oxygen-covered Cu(100) surfaces. The  $c(2\times 2)$  phase can thus play an important role as copper diffusion channel, consistent with the findings of Lahtonen et al [38].

### 3.3.3 Most Probable Paths

Although we did not consider all possible ejection and diffusion paths, we tried to follow a logical sequence of these events. In summary, the copper ejection and diffusion paths that are most likely to occur are shown in Figs. 3.7(a)-3.7(b). In the first path, one copper atom ejects from A to B, then diffuses to C, and finally diffuses away from the vacancy through  $\beta$  event on the perfect  $c(2\times 2)$  phase. For the second path, there are two ejected copper atoms. The first copper atom ejects from A1 to C1 and then stays there to decrease the energy barrier for the second copper atom ejection (or, another copper atom can diffuse to the C1 because of relatively small



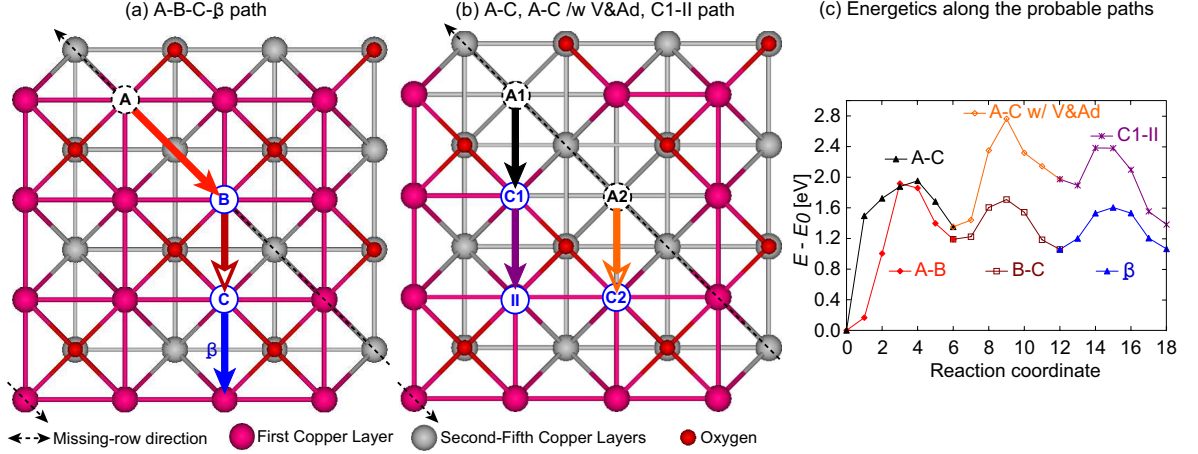


Figure 3.7: Copper ejection and diffusion paths that are most likely to occur during the transition from  $c(2 \times 2)$  to  $(2\sqrt{2} \times \sqrt{2})R45^\circ$  on the Cu(100) surface (the original position of the ejected copper atoms are indicated by dashed circles): (a)  $A \rightarrow B \rightarrow C \rightarrow \beta$  path, and (b)  $A1 \rightarrow C1 \rightarrow A2 \rightarrow C2$  w/ V&Ad- $C1 \rightarrow II$  path. (c) NEB results for each path.

energy barriers). When there is a copper adatom on C1, the second copper atom ejects from A2 to C2. Finally, the copper atom diffuses from C1 to II. The results shown in Fig. 3.7(c) describe the energy surface that the ejected copper atom goes through. The energies of the final states are bigger than that of the initial state [the  $c(2 \times 2)$  phase] because the NEB method must be applied to initial and final states that include the same number of atoms. In other words, the ejected copper atoms from the missing-row remain in the unit cell. When we removed the ejected copper atoms one by one from those unit cells, the surface-oxide energy,  $E_S$ , decreased and converged to the surface-oxide energy of the missing-row reconstruction, indicating that the big energy differences between the initial and final states are induced by the limitation of NEB method.

### 3.4 Summary

In this chapter, we used DFT calculations to investigate the kinetics and energetics of copper ejection and diffusion during the missing-row reconstruction. In Section

3.3.1, we investigated copper ejection paths using the NEB method and found that the most probable route to the missing-row reconstruction is the successive ejection of copper atoms to the C sites. The presence of a copper adatom on the C site was found to reduce the energy barrier for the next ejection by 0.54 eV. In Section 3.3.2, we showed that diffusion away from the C site is comparable to that on the  $c(2\times 2)$  phase. This finding indicates that the  $c(2\times 2)$  phase can act as a copper diffusion channel. In Section 3.3.3, we summarized probable ejection and diffusion paths and showed the potential energy surfaces that the ejected copper atoms go through. In the future, these energy barriers could be used in kinetic Monte Carlo simulations [97–101] to investigate larger length and longer time scales, which are not accessible using DFT calculations.

After the missing-row reconstruction,  $\text{Cu}_2\text{O}$  islands nucleate on the missing-row reconstructed domains [37] and oxygen embedment into substrate is observed by experiment [38]. We will investigate the energetics and kinetics of oxygen embedment in the next chapter.

## CHAPTER IV

# Energetics of oxygen embedment into unreconstructed and reconstructed Cu(100) surfaces

### 4.1 Introduction

As discussed in Chapter II, when a copper surface is exposed to an oxygen environment, the oxygen molecules approach the surface, dissociate [14, 16, 17, 20], and adsorb on the next-nearest-neighbor hollow sites [23]. As discussed in Chapters II and III, as the surface-oxygen coverage approaches 0.5 ML, the surface structure transforms into the missing-row reconstruction [25, 26, 28, 34]. Yang and co-workers found using transmission electron microscopy that  $\text{Cu}_2\text{O}$  islands then nucleate and grow [12, 39–42]. Thin film growth begins once the islands meet. The  $\text{Cu}_2\text{O}$  islands identified by Yang and co-workers grow into and out from the copper substrate as well as along it [41, 42]. Lampimäki et al. later observed using scanning tunneling microscopy that individual missing-row reconstructions merge to form ordered domains that are 1.8 Å higher than the clean surface and that  $\text{Cu}_2\text{O}$  islands form on these missing-row reconstructed domains [37]. Lampimäki et al. suggest that the elevated regions form as mobile copper adatoms stick to the phase boundaries between the missing-row reconstruction domains [37]. This explanation, however, is not sufficient to explain the subsequent oxide-island growth into the substrate, as it does

not provide a mechanism for oxygen supply to the sub-surface region.

Theoretical and modeling work has been performed on the oxygen-induced surface reconstruction and the early stages of the subsequent oxidation [13, 14, 16, 17, 20–22, 24, 35, 51, 53, 57, 61]. Kangas et al., using DFT, calculated adsorption energies on the missing-row reconstructed Cu(100) surface for various amounts of on- and sub-surface oxygen coverage [57]. They found that the presence of sub-surface oxygen makes the system more energetically stable at 1.0 ML and higher oxygen coverages (including on- and sub-surface oxygen) [57]. Kangas and Laasonen found that oxygen embeds into the sub-surface more easily when there are adsorbed oxygen atoms both on the surface and in the sub-surface [61]. The unit cell  $[p(2\sqrt{2} \times \sqrt{2})]$  used in that study, however, was too small for the authors to determine if the missing row plays an important role in the oxygen embedment.

The objective of the work presented in this chapter is to apply DFT calculations to investigate oxygen embedment energetics and to identify potential embedding paths on the missing-row reconstructed Cu(100) surface. In Section 4.2, the computational unit cells, set-up, and procedures are presented. We investigate the relationship between the oxygen embedment energetics, surface oxygen coverage, and surface morphology in Sections 4.3.1 and 4.3.2. Then, we investigate the energetics of embedding an oxygen atom into the missing-row reconstruction along different embedding paths in Section 4.3.3. In Section 4.3.4, we examine how oxygen atoms diffuse between sub-surface sites.

## 4.2 Calculation methodology

The Cu(100) surface morphologies used in this work are shown in Fig. 4.1. The oxygen coverage is defined as the fraction of face-centered cubic (fcc) hollow sites

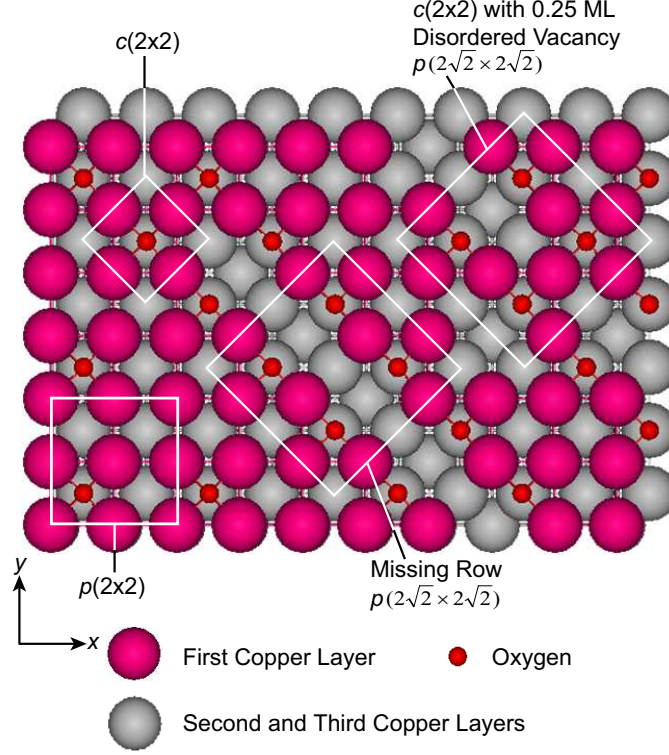


Figure 4.1: Cu(100) surface structures used in this work. The squares indicate the unit cells. The  $p(4 \times 4)$  unit cell area is four times bigger than the  $p(2 \times 2)$  unit cell area. Copyright 2009 Elsevier B.V.

occupied by oxygen. To study the surface-oxygen coverage effect (Section 4.3.1), we use the  $p(2 \times 2)$  and  $p(4 \times 4)$  unit cells at 0.25, 0.5, 0.75, and 1.0 ML oxygen coverages. To study the surface morphology effect (Section 4.3.2), we use the  $p(2\sqrt{2} \times 2\sqrt{2})$  unit cell at 0.5 ML coverage and three different surface morphologies [ $c(2 \times 2)$ , the missing-row reconstruction, and  $c(2 \times 2)$  with 0.25 ML disordered vacancy]. The  $c(2 \times 2)$  with 0.25 ML disordered vacancy morphology has one quarter of the first-layer copper atoms randomly replaced with vacancies [34]. For our DFT calculations, we obtain this structure by taking the missing-row reconstruction and moving one surface copper atom to the missing-row.

The DFT calculations are performed using the Vienna Ab-initio Simulation Package (VASP) [62–66], which uses a plane-wave basis set [64, 66]. We use ultra-soft

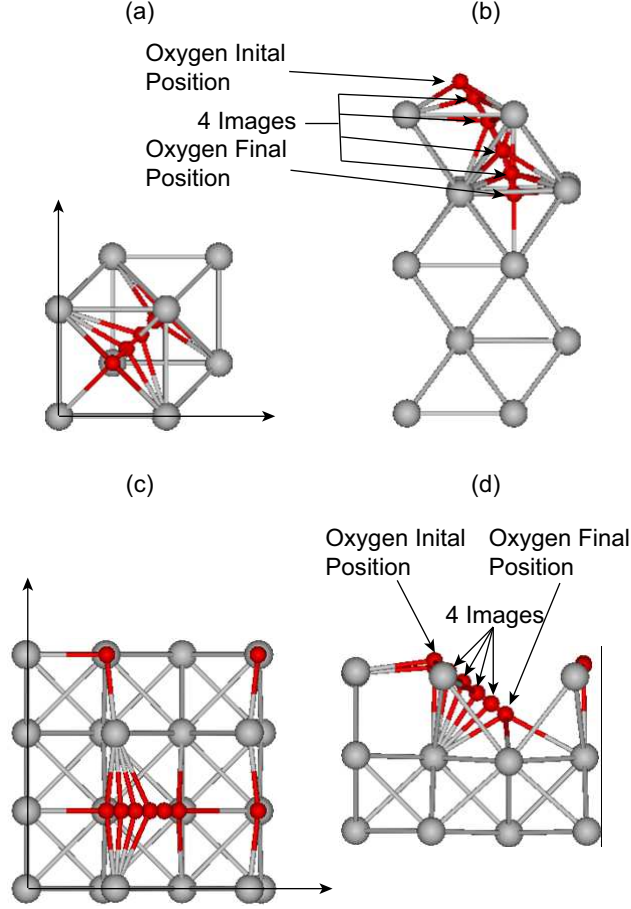


Figure 4.2: (a) Top and (b) side view of the  $p(2 \times 2)$  unit cell at 0.25 ML coverage with four images for a NEB calculation. (c) Top and (d) side view of the  $p(2\sqrt{2} \times 2\sqrt{2})$  unit cell (missing-row reconstruction) at 0.5 ML coverage with four images for a NEB calculation. Copyright 2009 Elsevier B.V.

pseudo potentials, the PW91 generalized gradient approximation [86], and apply a 330 eV energy cutoff.

The  $p(2 \times 2)$  unit cell contains five copper layers, as shown in Figs. 4.2(a) and 4.2(b). The  $p(4 \times 4)$  unit cell contains four copper layers to decrease the computational load. For the  $p(2\sqrt{2} \times 2\sqrt{2})$  unit cell, as shown in Figs. 4.2(c) and 4.2(d), we use three copper layers due to the large number of atoms. In Sections 4.3.3 and 4.3.4, however, five copper layers are used for the  $p(2\sqrt{2} \times 2\sqrt{2})$  unit cell. The vacuum size is 11 Å for all cases. The bottom copper layer is fixed and the other layers are relaxed during the structure optimization. The  $k$ -point mesh is generated by the Monkhorst-Pack

scheme [79]. To be consistent with Kangas et al. [57], we use a  $6 \times 6 \times 1$  mesh for the  $p(2 \times 2)$  unit cell, a  $3 \times 3 \times 1$  mesh for the  $p(4 \times 4)$  unit cell, and an  $8 \times 8 \times 1$  mesh for the  $p(2\sqrt{2} \times 2\sqrt{2})$  unit cell. The  $p(2\sqrt{2} \times 2\sqrt{2})$  unit cell is twice as big as that used by Kangas and co-workers [57, 61]. This larger unit cell will allow us to investigate the energetics of embedding oxygen into the  $c(2 \times 2)$  with 0.25 ML disordered vacancy structure (see Fig. 4.1) and through more paths.

To investigate the energetics of oxygen embedment into the copper surface, the climbing image nudged elastic band (NEB) method is applied [87–90]. The NEB method is a computational approach for finding the minimum energy path between specified initial and final equilibrium states. To specify the initial and final states, separate single-point DFT calculations are performed to ensure relaxed structures. We use spin-averaged calculations for the surface-adsorbed oxygen atoms and a dipole correction to compensate for having adsorbates on only one side of the structure. Based on the initial and final states, four images are created along the embedding path (see Fig. 4.2).

The relative stabilities of the equilibrium structures are compared using the surface-oxide energy,  $E_S$  [102]:

$$E_S = \frac{E_{O/Cu} - N_{Cu} \cdot E_{Cu,bulk} - N_O \cdot \frac{E_{O_2}}{2}}{A_{surf}}. \quad (4.1)$$

Here,  $E_{O/Cu}$  is the total system energy,  $E_{Cu,bulk}$  is the energy of one atom in bulk fcc copper, and  $E_{O_2}$  is the energy of an isolated oxygen molecule.  $N_O$  and  $N_{Cu}$  are the total number of oxygen and copper atoms in the system, and  $A_{surf}$  is the unit-cell surface area. Because  $E_S$  is normalized by the unit-cell area, we can compare surfaces with different unit-cell sizes. A spin-polarized DFT calculation is used to obtain  $E_{O_2}$ .

We performed convergence tests for the  $p(2\sqrt{2} \times 2\sqrt{2})$  missing-row reconstructed

Table 4.1: Surface-oxide energy,  $E_S$ , energy difference,  $E_{diff}$ , and energy barrier,  $E_{barrier}$ , for oxygen embedment into the Cu(100)  $p(2\times 2)$  and  $p(4\times 4)$  unit cells at different oxygen coverages. The unit cell area is  $26.645 \text{ \AA}^2$  for  $p(2\times 2)$  and  $106.58 \text{ \AA}^2$  for  $p(4\times 4)$ .  $E_{diff}$  is calculated by subtracting the total system energy of the initial state from that of final state.  $E_{barrier}$  is the energy difference between the initial state and the local energy maximum.

Coverage [ML]	unit cell	$E_{S,Initial}$ [eV/ $\text{\AA}^2$ ]	$E_{S,Final}$ [eV/ $\text{\AA}^2$ ]	$E_{diff}$ [eV]	$E_{barrier}$ [eV]
0.25	$p(2\times 2)$	0.104	0.193	2.37	2.54
0.5	$p(2\times 2)$	0.040	0.103	1.69	2.30
0.75	$p(2\times 2)$	0.040	0.014	-0.67	0.20
1.0	$p(2\times 2)$	0.062	-	-	-
0.25	$p(4\times 4)$	0.106	0.128	2.27	2.65
0.5	$p(4\times 4)$	0.042	0.055	1.44	2.37
0.75	$p(4\times 4)$	0.040	0.026	-1.50	0.49
1.0	$p(4\times 4)$	0.068	-	-	-

surface for the number of  $k$ -points, the energy cutoff, and the number of copper layers. The total energy difference between  $8\times 8\times 1$  and  $12\times 12\times 1$   $k$ -point meshes is 0.005 eV. The total energy difference between 330 eV and 600 eV energy cutoffs is 0.066 eV. The difference of  $E_S \times A_{surf}$  is 0.048 eV for three layers and 0.041 eV for five layers with respect to eight layers. Based on these small energy changes, we believe that the energies reported in Section 6.3 are sufficiently converged to allow us to compare the different surfaces and oxygen embedment energetics.

### 4.3 Oxygen embedment energetics

#### 4.3.1 Unreconstructed Cu(100) surface: Role of oxygen coverage

In this section, we investigate the energetics of atomic oxygen embedment into the unreconstructed Cu(100) surface at 0.25 ML, 0.5 ML, 0.75 ML and 1.0 ML coverages. In all calculations, there is only one embedding oxygen atom, which is initially located on the surface and then penetrates into the sub-surface site to the final state. The initial and final structures are both relaxed. For the 1.0 ML coverage final states, we find that there are two sub-surface oxygen atoms for the  $p(2\times 2)$  unit cell and a severe surface restructuring for the  $p(4\times 4)$  unit cell, which break the single oxygen-atom



embedding condition. Because of these findings, we do not report the embedding energetics for the 1.0 ML coverage.

In the initial state, all oxygen atoms are located on the on-surface fcc sites. As shown in Table 4.1, increasing the oxygen coverage makes the initial surface more stable for the lower coverages. At higher coverages, increased oxygen-oxygen repulsion leads to higher energies. In the final state, one oxygen atom is located in a sub-surface fcc site. Increasing the oxygen coverage makes the final state more energetically stable because the top copper layer hides the sub-surface oxygen atom, weakening the repulsive interactions between oxygen atoms [103]. The initial states are energetically more stable than the final states at 0.25 ML and 0.5 ML coverages. The final state is more stable than the initial state at 0.75 ML coverage, indicating that the oxygen embedding is energetically favorable. The trends for the  $p(2\times 2)$  and  $p(4\times 4)$  unit cells are comparable.

The NEB results are presented in Table 4.1 and Figs. 4.3(a) and 4.3(b). In Table 4.1, the energy difference,  $E_{diff}$ , is calculated by subtracting the total system energy of the initial state from that of final state. The energy difference is positive at the lower oxygen coverages (0.25 ML and 0.5 ML) and negative at the higher coverage (0.75 ML). The negative value at higher coverage indicates that the sub-surface adsorption site is more stable than the on-surface site.

The energy barrier,  $E_{barrier}$ , is the energy difference between the initial state and the local energy maximum. As the oxygen coverage increases, the energy barriers decrease for both the  $p(2\times 2)$  and  $p(4\times 4)$  unit cells. The energy barriers for the  $p(4\times 4)$  unit cell are slightly higher than these for the  $p(2\times 2)$  unit cell, but the trends are consistent. These results indicate that oxygen embedding will first occur between coverages of 0.5 ML and 0.75 ML, where the energy difference becomes negative and

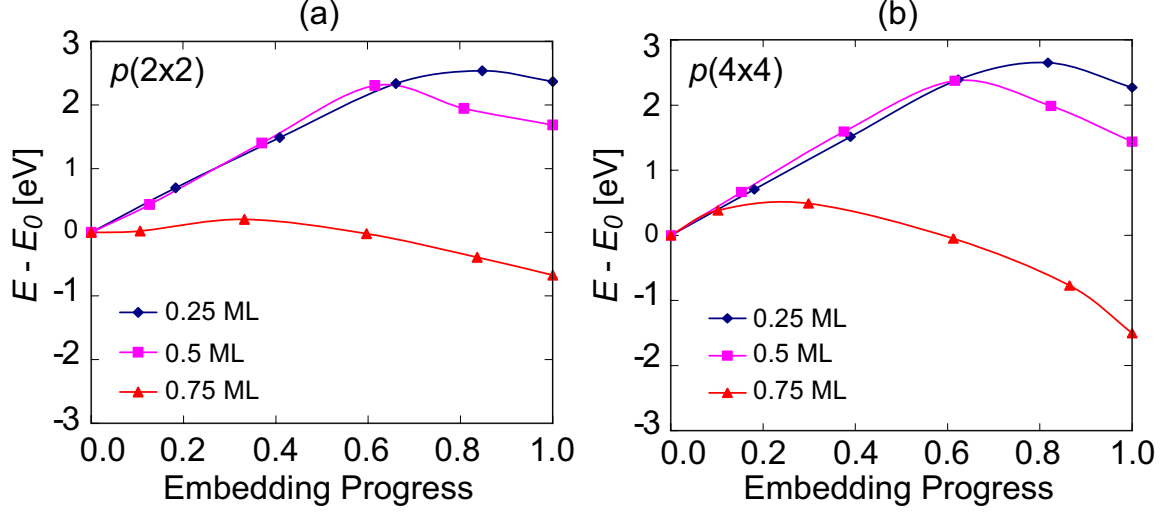


Figure 4.3: Energetics of embedding an oxygen atom into the (a) the  $p(2 \times 2)$  unit cell and (b) the  $p(4 \times 4)$  unit cell ( $E$  = image energy,  $E_0$  = energy of image 0). The embedding progress is the ratio of the embedding distance of each image to the total embedding distance. Lines are shown to guide the eye. Copyright 2009 Elsevier B.V.

Table 4.2: Surface-oxide energy,  $E_S$ , energy difference,  $E_{diff}$ , and energy barrier,  $E_{barrier}$ , for oxygen embedment into the Cu(100)  $p(2\sqrt{2} \times 2\sqrt{2})$  unit cell with different surface morphologies [ $c(2 \times 2)$  w/ 0.25 DV is  $c(2 \times 2)$  with 0.25 ML disordered vacancy]. The unit cell area is  $53.290 \text{ \AA}^2$  for all cases and the coverage is 0.5 ML.

Morphology	$E_{S,Initial}$ [eV/ $\text{\AA}^2$ ]	$E_{S,Final}$ [eV/ $\text{\AA}^2$ ]	$E_{diff}$ [eV]	$E_{barrier}$ [eV]
$c(2 \times 2)$	0.049	0.078	1.55	1.96
Missing-row	0.039	0.066	1.43	1.55
$c(2 \times 2)$ w/ 0.25 DV	0.043	0.062	1.02	1.43

the energy barrier decreases.

#### 4.3.2 Cu(100) surface at 0.5 ML coverage: Role of surface morphology

In this section, we investigate the energetics of embedding an oxygen atom into surfaces with different morphologies. We use the same unit-cell size [ $p(2\sqrt{2} \times 2\sqrt{2})$ ] and oxygen coverage (0.5 ML) for all the calculations. For the different surface morphologies, we use (i)  $c(2 \times 2)$ , (ii) the missing-row reconstruction, and (iii)  $c(2 \times 2)$  with 0.25 ML disordered vacancy. These structures are shown in Fig. 4.1. We choose the oxygen atom located in the lower-left position of the unit cell as the embedding

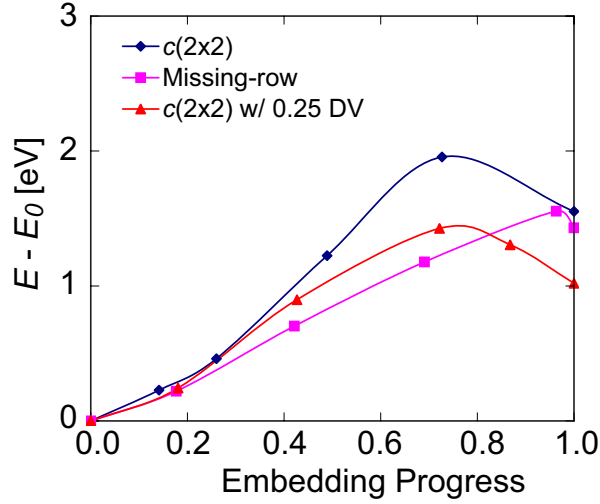


Figure 4.4: Energetics of embedding an oxygen atom into the  $p(2\sqrt{2}\times 2\sqrt{2})$  unit cell for different surface morphologies. ( $E$  = image energy,  $E_0$  = energy of image 0) at 0.5 ML coverage. The embedding progress is the ratio of the embedding distance of each image to the total embedding distance. Lines are shown to guide the eye. Copyright 2009 Elsevier B.V.

oxygen atom for all morphologies [see Figs. 4.2(c) and 4.2(d)].

The embedding energetics are shown in Table 4.2 and Fig. 4.4. The energy differences are all positive, indicating that the initial state is more stable than the final state. The missing-row reconstruction and  $c(2\times 2)$  with 0.25 ML disordered vacancy structures have lower energy barriers than the  $c(2\times 2)$  surface. Based on these findings, in the next section we will investigate the energetics of embedding an additional oxygen atom into the missing-row reconstructed surface.

#### 4.3.3 Reconstructed Cu(100) surface: Role of embedding path

To identify potential oxygen embedding paths into the missing-row reconstruction, in this section we investigate atomic oxygen embedment into the  $p(2\sqrt{2}\times 2\sqrt{2})$  unit cell including five copper layers.<sup>1</sup> The bottom copper layer is fixed. An oxygen coverage of 0.625 ML is considered, which includes one embedding oxygen atom and

<sup>1</sup>In our published paper [68], we used three copper layers structures. Here, we use five copper layer so as to obtain more accurate embedment energy barriers. The general trends of the energy barriers are the same between the three layer and five layer structures.

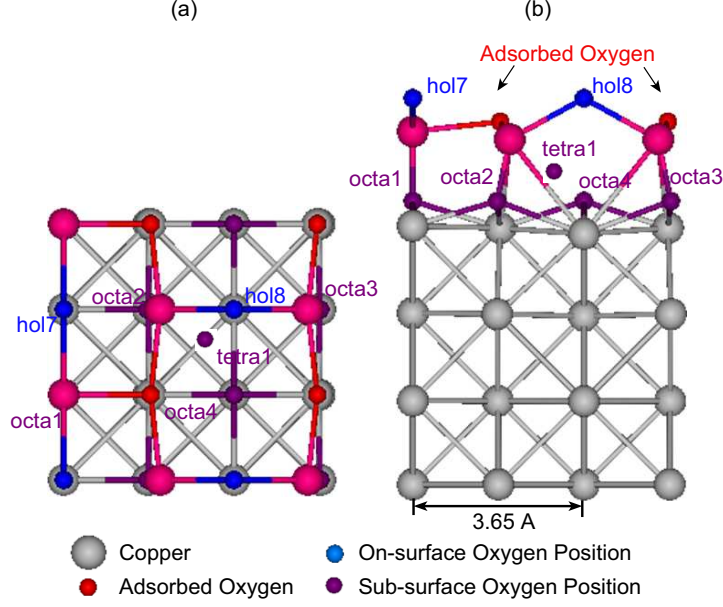


Figure 4.5: (a) Top and (b) Side view of the  $p(2\sqrt{2} \times 2\sqrt{2})$  unit cell and the initial and final positions of the embedding oxygen atom. Copyright 2009 Elsevier B.V.

four surface-adsorbed oxygen atoms. The initial and final positions of the embedding oxygen atom (on-surface and sub-surface oxygen positions) are shown in Figs. 4.5(a) and 4.5(b). All of these states are relaxed, stable structures. We adopt the notation of Kangas et al. [61]. “Hol”, “tetra”, and “octa” refer to the fcc hollow, tetrahedral, and octahedral sites. The energy difference ( $E_{diff}$ ) and energy barrier ( $E_{barrier}$ ) for six embedding paths are listed in Table 4.3 and the energetics are plotted in Figs. 4.6(c).

As shown in Tables 4.1, 4.2, and 4.3, the surface-oxide energies,  $E_S$ , for the missing-row reconstructed surfaces are smaller than those of the unreconstructed surface structures. This result indicates that the missing-row reconstructed surface is more stable than the other surfaces, consistent with a previous report [57].

Our objective is to determine how the embedment energetics differ between missing-row and non-missing-row paths. The missing-row paths are path1 (hol8 to octa4) and path3 (hol8 to octa2). The non-missing-row paths are path2 (hol7 to octa1) and path4

Table 4.3: Surface-oxide energy,  $E_S$ , energy difference,  $E_{diff}$ , and energy barrier,  $E_{barrier}$ , for oxygen embedment into the missing-row reconstructed Cu(100) surface for different embedding paths. The initial and final positions of the embedding oxygen atom are shown in Fig. 4.5.

Index	Initial Position	Final Position	$E_{S,Initial}$ [eV/Å <sup>2</sup> ]	$E_{S,Final}$ [eV/Å <sup>2</sup> ]	$E_{diff}$ [eV]	$E_{barrier}$ [eV]
path1 (mr)	hol8	octa4	0.036	0.025	-0.58	0.26
path2	hol7	octa1	0.029	0.028	-0.10	0.89
path3 (mr)	hol8	octa2	0.036	0.029	-0.35	0.30
path4	hol7	octa2	0.029	0.029	-0.02	0.86
path5(a)	octa4	tetra1	0.025	0.032	0.39	0.68
path5(b)	tetra1	octa2	0.032	0.029	-0.16	0.28
path6	octa2	octa1	0.029	0.028	-0.08	0.78

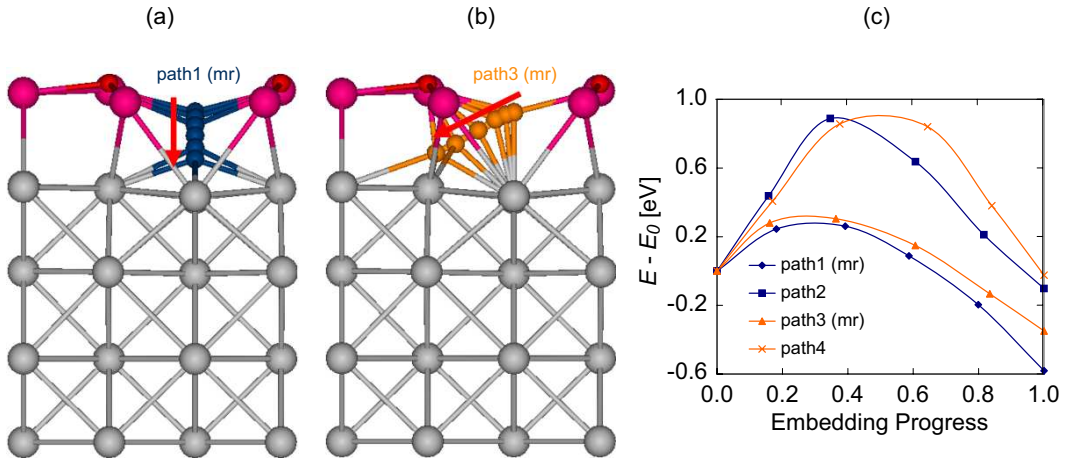


Figure 4.6: Illustrations for embedding (a) path1 and (b) path3. The initial and final positions of the embedding oxygen atom are provided in Table 4.3 and Fig. 4.5. (c) Embedding oxygen atom energetics for path1-path4 into the missing-row reconstructed Cu(100) surface.

(hol7 to octa2). As shown in Figs. 4.6(c) and 4.6(d) and Table 4.3, the energy barrier is smaller through the missing-row paths (0.26 eV for path1 and 0.30 eV for path3) than through the non-missing-row paths (0.89 eV for path2 and 0.86 eV for path4). For comparison, the energy barrier predicted by DFT for the diffusion of an oxygen atom between hollow sites on a clean Cu(100) surface is 0.74 eV [20]. Oxygen embedment is thus more probable through the missing-row. In addition,  $E_{diff}$  is negative only for the missing-row paths, indicating that the missing-row paths are energetically more favorable than non-missing-row paths.

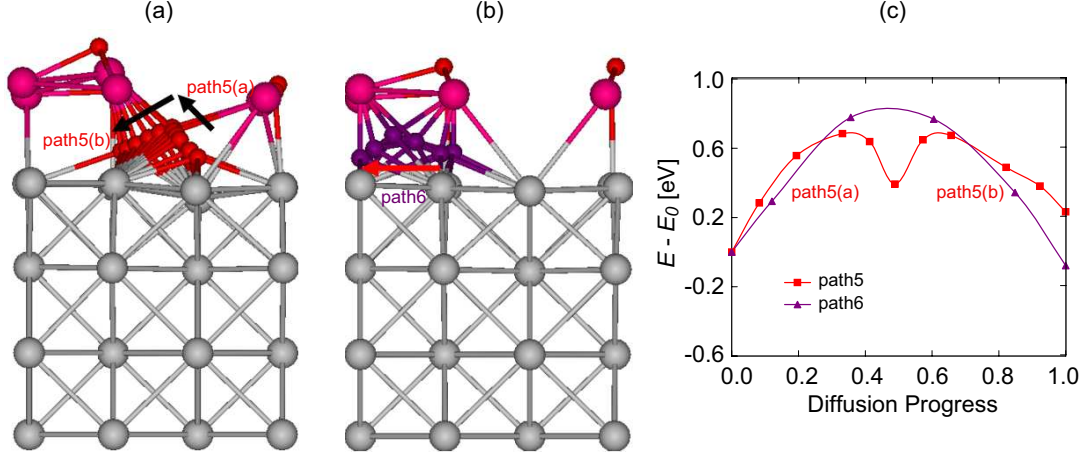


Figure 4.7: Illustrations for embedding (a) path5 and (b) path6. The initial and final positions are provided in Table 4.3 and Fig. 4.5. (c) Sub-surface oxygen atom diffusion energetics for path5 and path6 in the missing-row reconstructed Cu(100) surface.

#### 4.3.4 Reconstructed Cu(100) surface: Oxygen diffusion between sub-surface adsorption sites

As shown in Section 4.3.3, the energy barriers for oxygen embedment through the missing-row paths are smaller than that for surface diffusion. Previous DFT studies [57,61] found that when the missing-row reconstructed Cu(100) surface includes both on- and sub-surface oxygen adsorption, the surface is energetically more favorable than the case of only on-surface adsorption. Based on these two findings, we expect that oxygen atoms will diffuse between the sub-surface adsorption sites [octa1-octa4, see Fig. 4.5(b)]. We investigate the sub-surface oxygen diffusion energetics by NEB calculation. The results are provided in Table 4.3 and Figs. 4.7(c) and 4.7(d). We find that a local energy minimum exists between octa4 and octa2 (denoted by tetra1), and two separate NEB calculations are thus performed. The energy barriers for path5 and path6 are smaller than or comparable to that for surface diffusion (0.74 eV), indicating that sub-surface diffusion is probable. This sub-surface diffusion mechanism may be useful in explaining how to form the on- and sub-surface-adsorption structures suggested by previous DFT studies [57,61].

## 4.4 Summary

We applied DFT calculations to study the energetics of embedding atomic oxygen into a copper surface. When the surface oxygen coverage increases on the unreconstructed Cu(100) surface, as shown in Figs. 4.3(a) and 4.3(b), the energy barrier for the oxygen embedment decreases. The embedding energetics is found to vary with the surface morphology, with the reconstructed surfaces [missing-row reconstruction and  $c(2\times 2)$  with 0.25 ML disordered vacancy] being more favorable than the  $c(2\times 2)$  structure for oxygen embedment (see Fig. 4.4). As shown in Figs. 4.6(c) and 4.7(c), on the missing-row reconstructed surface, the energy barriers for oxygen embedment through the missing-row and sub-surface diffusion are small compared to that for surface diffusion on a clean Cu(100) surface. These results indicate that oxygen embedment and sub-surface diffusion are potential mechanisms for linking the missing-row reconstruction to Cu<sub>2</sub>O island nucleation. In the next chapter, we will test this hypothesis to explain the transition mechanism between the reconstructed surface and the bulk-like oxide.

## CHAPTER V

### Role of sub-surface oxygen in Cu(100) oxidation

#### 5.1 Introduction

There have been theoretical and experimental investigations of the atomic oxygen adsorption [13–24] and the oxygen-induced surface reconstruction [25–36]. A limited number of investigations, however, have studied the transition from the missing-row reconstruction to  $\text{Cu}_2\text{O}$  island formation [37, 38, 57, 61, 68]. Lahtonen et al. found, using STM and x-ray photoelectron spectroscopy, that oxygen penetration into the sub-surface region plays a key role in the subsequent oxidation and the growth of  $\text{Cu}_2\text{O}$  islands [38].

The objective of the work presented in this chapter is to use DFT calculations to investigate the transition from the missing-row reconstructed Cu(100) surface to  $\text{Cu}_2\text{O}$  island formation. In Chapter IV, we used DFT calculations to show that oxygen embedment into the Cu(100) surface and sub-surface diffusion are possible mechanisms for driving this transition. In Section 5.2, the computational unit cells, set-up, and procedures are presented. In Section 5.3.1, we investigate the relative stabilities of unreconstructed and reconstructed Cu(100) surfaces. In Section 5.3.2, we analyze the energetic and structural changes induced when an oxygen molecule interacts with missing-row reconstructed Cu(100) surfaces for different on- and sub-



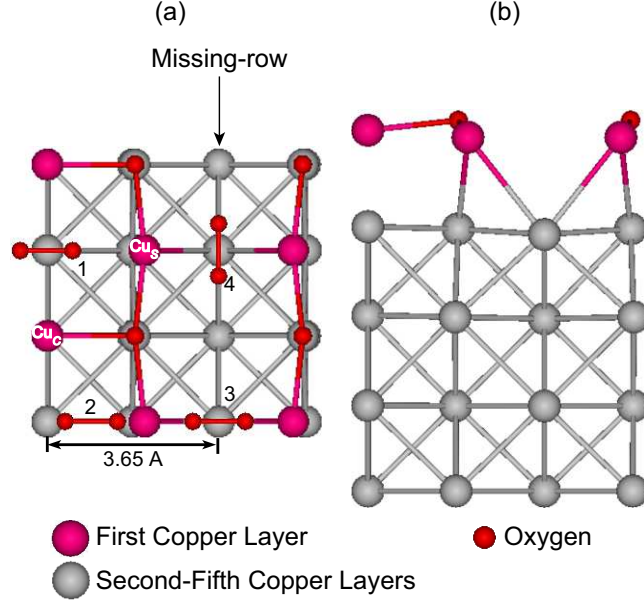


Figure 5.1: Initial positions of the oxygen molecule on the missing-row reconstructed Cu(100) surface. (a) Top and (b) side view of the  $p(2\sqrt{2} \times 2\sqrt{2})$  unit cell at 0.5 ML coverage: 1. fcc hollow site (FCC). 2. Between fcc and  $\text{Cu}_S$  (BFC). 3. Perpendicular to missing row (PMR). 4. Parallel to missing row (RMR). The oxygen molecules are only shown in (a). Copyright 2010 Elsevier B.V.

surface oxygen coverages. In Section 5.3.3, we demonstrate that the  $c(2 \times 2)$  to  $(2\sqrt{2} \times \sqrt{2})\text{R}45^\circ$  transition is necessary for subsequent  $\text{Cu}_2\text{O}$  formation using both energetic and structural arguments.

## 5.2 Calculation methodology

Our DFT calculations are performed using the Vienna Ab-initio Simulation Package (VASP) [62–66], which uses a plane-wave basis set [64, 66]. We use ultra-soft pseudo potentials, the PW91 generalized gradient approximation [86], and apply a 350 eV energy cutoff. The  $p(2 \times 2)$  unit cell is used for the unreconstructed surface and the  $p(2\sqrt{2} \times 2\sqrt{2})$  and  $p(4\sqrt{2} \times 4\sqrt{2})$  unit cells are used for the missing-row reconstructed surface. All the slab structures include 5 copper layers (with the bottom layer fixed) and a vacuum gap thickness of 11 Å. There are 152 copper and 48 oxygen atoms in the  $p(4\sqrt{2} \times 4\sqrt{2})$  unit cell with a sub-surface oxygen coverage of 1.0 ML,

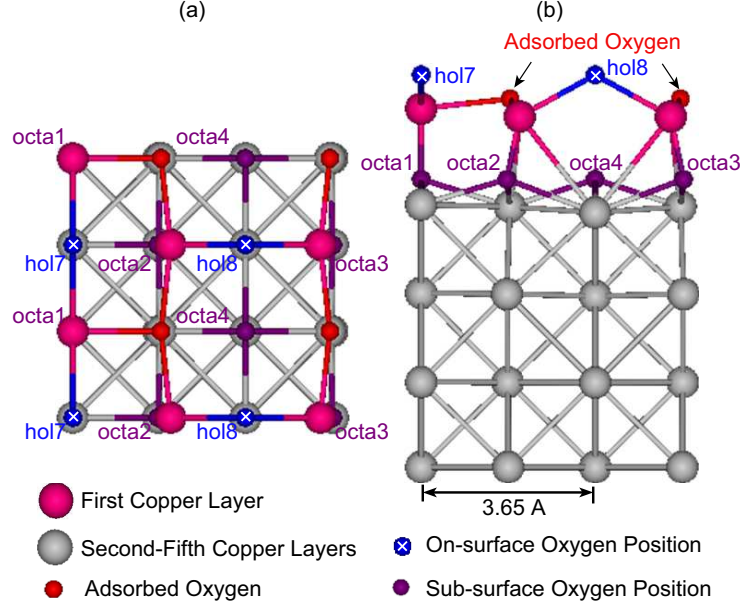


Figure 5.2: (a) Top and (b) side views of the unreaxed missing-row reconstructed Cu(100) surface with on- and sub-surface oxygen atoms in the  $p(2\sqrt{2} \times 2\sqrt{2})$  unit cell. Copyright 2010 Elsevier B.V.

the largest that we consider. The  $k$ -point mesh is generated by the Monkhorst-Pack scheme [79]. We use an  $8 \times 8 \times 1$  mesh for the  $p(2 \times 2)$  and  $p(2\sqrt{2} \times 2\sqrt{2})$  unit cells, and a  $4 \times 4 \times 1$  mesh for the  $p(4\sqrt{2} \times 4\sqrt{2})$  unit cell.

To induce further restructuring, we add an oxygen molecule to the missing-row structures. The initial positions are shown in Figs. 5.1(a) and 5.1(b). The copper atom located at the step-edges next to the missing row is labeled  $\text{Cu}_s$ . The topmost copper atoms located between the copper atoms at the step-edges are labeled  $\text{Cu}_C$ .

The on- and sub-surface oxygen sites for the unreaxed reconstructed surface are shown in Figs. 5.2(a) and 5.2(b). “Hol” and “octa” refer to the fcc hollow and octahedral sites, consistent with the notation used in Chapter IV. In the  $p(2\sqrt{2} \times 2\sqrt{2})$  unit cell, there are two identical locations for each hol and octa site. The label “2hol7” represents the missing-row reconstructed surface with every hol7 site occupied. “octa23” represents a surface with one octa2 site and one octa3 site occupied. In the “2octa23” structure, every octa2 and octa3 site is occupied.

The relative stabilities of the relaxed structures described in Sections 5.3.1 and 5.3.2 are compared using the surface-oxide energy,  $E_S$  [68, 102]:

$$E_S = \frac{E_{O/Cu} - N_{Cu} \cdot E_{Cu,bulk} - N_O \cdot \frac{E_{O_2}}{2}}{A_{surf}}. \quad (5.1)$$

Here,  $E_{O/Cu}$  is the total system energy,  $E_{Cu,bulk}$  is the energy of one atom in bulk fcc copper, and  $E_{O_2}$  is the energy of an isolated oxygen molecule.  $N_O$  and  $N_{Cu}$  are the total number of oxygen and copper atoms in the system and  $A_{surf}$  is the unit cell surface area. Because  $E_S$  is normalized by the unit cell area, it can be used to compare surfaces with different unit cell sizes. A spin-polarized DFT calculation is used to obtain  $E_{O_2}$ . Spin-averaged calculations are used for all other calculations.

We performed convergence tests for the  $p(2\sqrt{2} \times 2\sqrt{2})$  missing-row reconstructed surface for the number of  $k$ -points, the energy cutoff, and the number of copper layers. The total energy difference between  $8 \times 8 \times 1$  and  $12 \times 12 \times 1$   $k$ -point meshes is 0.005 eV ( $9.4 \times 10^{-5}$  eV/Å<sup>2</sup>). The total energy difference between 350 eV and 600 eV energy cutoffs is 0.005 eV. The surface-oxide energy difference between 5 and 8 copper layers is  $7.7 \times 10^{-4}$  eV/Å<sup>2</sup>. Based on the magnitudes of these energy differences, we believe that the energies reported in Section 5.3 are sufficiently accurate to allow us to compare the stabilities of and structural changes in different structures.

### 5.3 Oxygen-induced surface restructuring

#### 5.3.1 Relative stabilities of surfaces relaxed without an oxygen molecule

In Table 5.1, we report the surface-oxide energy and the height of the top copper layer measured from that of the clean Cu(100) surface for different oxygen coverages.<sup>1</sup> No additional oxygen molecules are present. For the unreconstructed surfaces [clean,

---

<sup>1</sup>Using an energy cutoff of 330 eV, we previously reported the  $E_S$  of  $c(2 \times 2)$ ,  $mr$ , and  $p(2 \times 2)$  to be 0.049, 0.039, and 0.040 eV/Å<sup>2</sup> [68]. Based on the energy cutoff convergence test discussed in Section 5.2, we believe that the results presented in Table 5.1 are more accurate.

Table 5.1: Surface-oxide energy,  $E_S$ , and height change for different on- and sub-surface oxygen coverages. The unit cell area is  $26.645 \text{ \AA}^2$  for  $p(2 \times 2)$  and  $53.290 \text{ \AA}^2$  for  $p(2\sqrt{2} \times 2\sqrt{2})$ . “U” and “R” represent unreconstructed and reconstructed surfaces. Oxygen coverages are shown for on-surface (On-) and sub-surface (Sub-) separately. 2octa2, 2octa23, 2octa123, and 2octa1234 are missing-row reconstructed (mr) surfaces relaxed with sub-surface oxygen atoms [see Figs. 5.2(a) and 5.2(b)].

Index	U or R	On- [ML]	Sub- [ML]	Unit Cell	$E_S$ [eV/ $\text{\AA}^2$ ]	Height [ $\text{\AA}$ ]
clean	U	0.00	0.00	$p(2\sqrt{2} \times 2\sqrt{2})$	0.184	0.00
$c(2 \times 2)$	U	0.50	0.00	$p(2\sqrt{2} \times 2\sqrt{2})$	0.047	0.89
mr	R	0.50	0.00	$p(2\sqrt{2} \times 2\sqrt{2})$	0.045	0.32
$p(2 \times 2)$	U	0.75	0.00	$p(2 \times 2)$	0.047	0.44
$p(1 \times 1)$	U	1.00	0.00	$p(2 \times 2)$	0.070	0.36
2octa2	R	0.50	0.25	$p(2\sqrt{2} \times 2\sqrt{2})$	0.010	1.16
2octa23	R	0.50	0.50	$p(2\sqrt{2} \times 2\sqrt{2})$	-0.030	1.72
2octa123	R	0.50	0.75	$p(2\sqrt{2} \times 2\sqrt{2})$	-0.057	1.74
2octa1234	R	0.50	1.00	$p(2\sqrt{2} \times 2\sqrt{2})$	-0.051	1.75

$c(2 \times 2)$ ,  $p(2 \times 2)$ , and  $p(1 \times 1)$ ],  $E_S$  decreases with increasing oxygen coverage from 0 ML to 0.50 ML then increases from 0.75 ML to 1.0 ML. This result indicates that there is an energetically stable structure between coverages of 0.5 ML and 0.75 ML. At an oxygen coverage of 0.5 ML,  $E_S$  of the missing-row reconstructed (mr) surface is smaller than that of  $c(2 \times 2)$ . The missing-row reconstruction is thus more energetically favorable than  $c(2 \times 2)$ . We note that while the  $E_S$  difference is small and sensitive to the DFT calculation parameters, this result agrees with previous experimental and modeling works [25–36], indicating that the missing-row reconstructed surface is the stable transition state from a clean copper surface to copper-oxide island nucleation.

For the reconstructed surfaces (mr, 2octa2<sup>2</sup>, 2octa23, 2octa123, and 2octa1234), the on-surface oxygen coverage is fixed at 0.5 ML and the sub-surface oxygen coverage is increased from 0 (mr) to 1.0 ML (2octa1234). As the sub-surface oxygen coverage increases,  $E_S$  decreases, and the minimum  $E_S$  is predicted at a total coverage of 1.25 ML (2octa123). In all cases with sub-surface oxygen, there is a notable elevation of

<sup>2</sup>We tested all distinct structures at 0.25 ML sub-surface oxygen coverage (2octa1, 2octa2 and 2octa4). The minimum  $E_S$  and the maximum elevation of the top copper atoms are found for 2octa2.

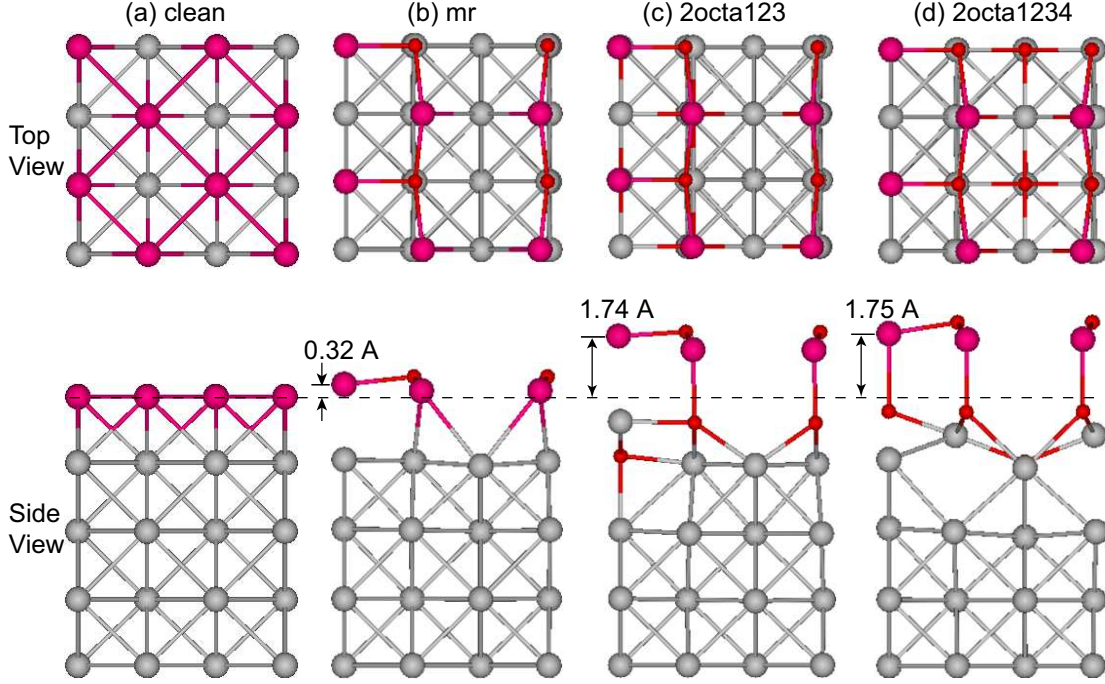


Figure 5.3: Top and side views of (a) the clean Cu(100) surface, (b) the missing-row reconstruction (mr), and missing-row reconstructed surfaces relaxed with sub-surface oxygen atoms [(c) 2octa123 and (d) 2octa1234]. Copyright 2010 Elsevier B.V.

the top copper layer and structural changes [compare Figs. 5.3(c) and 5.3(d) to Figs. 5.3(a) and 5.3(b)]. The smaller  $E_S$  values indicate that sub-surface oxygen makes the surfaces more energetically stable, as found by others [57,61].

We previously argued for the presence of sub-surface oxygen by showing that the energy barriers for oxygen embedment are comparable to those for on-surface diffusion [68]. Further proof for the existence of sub-surface oxygen can be obtained by comparing the DFT-predicted surface elevation to experimental measurements. As shown in Figs. 5.3(c) and 5.3(d), sub-surface oxygen atoms cause the surface to rise by 1.7 Å. This height is comparable to the 1.8 Å elevation measured by STM as shown in the line profile 3 of Fig. 1.4(b).

While the energetic and structural results presented in this section demonstrate the likely presence of sub-surface oxygen during Cu(100) oxidation process, they do

not lead to the surface restructuring that we hypothesize is needed before  $\text{Cu}_2\text{O}$  can form. As such, we next investigate the surface restructuring induced by the presence of an additional oxygen molecule.

### 5.3.2 Missing-row reconstructed Cu(100) surfaces relaxed with an oxygen molecule

Using STM, Lahotonen et al. found that defects in a  $\text{Cu}_2\text{O}$  island play a role in the growth of additional oxide [38]. To test if this defect effect is present in the earlier stages of oxidation, we first examined the stability and structure of missing-row reconstructed Cu(100) surfaces with or without a copper point defect with an oxygen molecule located at the initial positions shown in Fig. 5.1(a). No significant structural and/or energetic changes were found. Based on these results, we believe that while defects play a role after  $\text{Cu}_2\text{O}$  island nucleation, they do not play a significant role in the transition from the missing-row reconstruction to  $\text{Cu}_2\text{O}$  island nucleation.

We next examined the effect of on- and sub-surface oxygen atoms on the structure of the missing-row reconstructed Cu(100) surface when it is exposed to an additional oxygen molecule. In Table 5.2, the surface-oxide energies are reported for relaxed surfaces without an oxygen molecule (“No  $\text{O}_2$ ”) and with an oxygen molecule at different initial positions [see Fig. 5.1(a)]. In Fig. 5.4, we plot the  $E_S$  of each surface relaxed without an oxygen molecule and the minimum  $E_S$  of the surface relaxed with an oxygen molecule from Table 5.2 to highlight the effects of oxygen-induced surface restructuring.

When extra oxygen atoms are added to the on-surface sites and the surfaces are relaxed without an oxygen molecule,  $E_S$  drops for 2hol7 and 2hol78, while  $E_S$  for 2hol8 shows a much smaller decrease. This result indicates that the hol7 sites are more effective at stabilizing the surface than the hol8 sites. The hol7 site is surrounded

Table 5.2: Surface-oxide energy,  $E_S$ , of missing-row reconstructed Cu(100) surfaces including extra oxygen atoms at the on- and/or sub-surface sites [see Figs. 5.2(a) and 5.2(b)]. In the columns below  $E_S$ , the results for surfaces relaxed without or with an additional oxygen molecule are provided. For the surfaces relaxed with an additional oxygen molecule, we use four different initial positions: fcc hollow (FCC), between fcc hollow and Cu<sub>S</sub> (BFC), perpendicular to missing-row (PMR), and parallel to missing-row (RMR) [see Fig. 5.1(a)]. The unit cell area is 53.290 Å<sup>2</sup> for  $p(2\sqrt{2}\times 2\sqrt{2})$  and 213.16 Å<sup>2</sup> for  $p(4\sqrt{2}\times 4\sqrt{2})$ . The bolded  $E_S$  values correspond to the oxide-like structures, some of which are shown in Figs. 5.5(a), 5.5(b), 5.5(e), and 5.5(f).

Index	On- [ML]	Sub- [ML]	Unit Cell	$E_S$ [eV/Å <sup>2</sup> ]				
				No O <sub>2</sub>	FCC	BFC	PMR	RMR
mr	0.50	0.00	$p(2\sqrt{2}\times 2\sqrt{2})$	0.045	0.054	0.044	0.046	0.060
2hol7	0.75	0.00	$p(2\sqrt{2}\times 2\sqrt{2})$	0.006	0.020	0.013	0.006	0.020
2hol8	0.75	0.00	$p(2\sqrt{2}\times 2\sqrt{2})$	0.039	0.026	0.018	0.032	0.053
2hol78	1.00	0.00	$p(2\sqrt{2}\times 2\sqrt{2})$	0.003	0.015	-0.008	0.001	0.006
octa12	0.50	0.25	$p(2\sqrt{2}\times 2\sqrt{2})$	0.022	0.008	0.026	0.014	0.015
2octa2	0.50	0.25	$p(2\sqrt{2}\times 2\sqrt{2})$	0.010	0.015	0.056	0.008	0.020
2octa12	0.50	0.50	$p(2\sqrt{2}\times 2\sqrt{2})$	-0.016	<b>-0.025</b>	0.073	-0.024	0.000
2octa12	0.50	0.50	$p(4\sqrt{2}\times 4\sqrt{2})$	-0.016	<b>-0.019</b>	0.004	-0.020	-0.013
2octa14	0.50	0.50	$p(2\sqrt{2}\times 2\sqrt{2})$	-0.012	-0.010	-0.016	-0.015	-0.013
2octa23	0.50	0.50	$p(2\sqrt{2}\times 2\sqrt{2})$	-0.030	-0.028	-0.028	-0.030	-0.014
octa1234	0.50	0.50	$p(2\sqrt{2}\times 2\sqrt{2})$	-0.005	-0.018	-0.017	-0.022	-0.015
2octa123	0.50	0.75	$p(2\sqrt{2}\times 2\sqrt{2})$	-0.057	-0.055	-0.056	-0.060	-0.042
2octa1234	0.50	1.00	$p(2\sqrt{2}\times 2\sqrt{2})$	-0.051	<b>-0.102</b>	-0.066	-0.074	-0.034
2octa1234	0.50	1.00	$p(4\sqrt{2}\times 4\sqrt{2})$	-0.051	<b>-0.079</b>	<b>-0.079</b>	-0.053	-0.047

by four copper atoms and is the most favorable adsorption site for atomic oxygen [20].

The hol8 site, however, has only two nearest-neighbor copper atoms because of the missing-row and is thus less effective at stabilizing the surface.

While  $E_S$  decreases in the presence of on-surface oxygen atoms,  $E_S$  for the majority of the surfaces relaxed with an extra oxygen molecule is comparable to or greater than that of the surfaces relaxed without an oxygen molecule. The exceptions are 2hol8 (FCC, BFC, and PMR) and 2hol78 (BFC and PMR). In the relaxed structures of 2hol8 FCC and BFC, we found that the oxygen molecule or dissociated oxygen atom adsorbs at the stabilizing hol7 site. In the relaxed structures of 2hol8 PMR, 2hol78 BFC, and 2hol78 PMR, there is further elevation of the top copper atoms. We attribute this elevation to repulsion between the oxygen molecule and the adsorbed oxygen atom at hol8 (2hol8 PMR and 2hol78 PMR) or hol7 (2hol78 BFC). This fur-

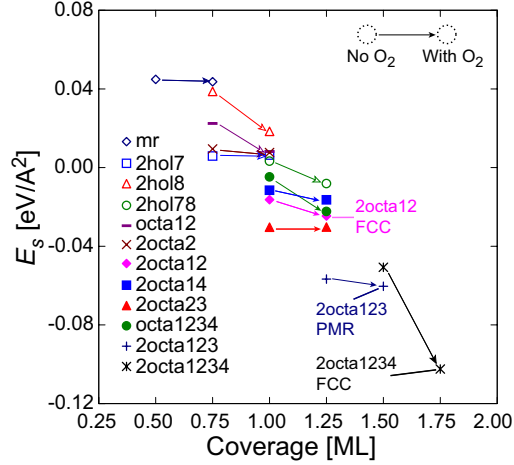


Figure 5.4: Surface-oxide energy vs. oxygen coverage on the missing-row reconstructed Cu(100) surface with extra on- and sub-surface oxygen atoms. For each index,  $E_S$  is plotted for the case without an additional oxygen molecule and the minimum value found in the presence of an additional oxygen molecule (see data in Table 5.2). For each index, the  $E_S$  of the surface relaxed without an oxygen molecule (“No O<sub>2</sub>”) is connected to that of the surface relaxed with an oxygen molecule (“With O<sub>2</sub>”) by an arrow. Copyright 2010 Elsevier B.V.

ther surface elevation induces a decrease in  $E_S$ . In all cases, there is no significant surface restructuring (i.e, no formation of oxide-like structures). These findings indicate that extra oxygen atoms on the on-surface adsorption sites are not sufficient to induce the transition from the missing-row reconstruction to Cu<sub>2</sub>O island formation. We therefore need to investigate the role of sub-surface oxygen.

For the missing-row reconstructed surfaces including sub-surface oxygen, the  $E_S$  of surfaces without an oxygen molecule decreases with increasing sub-surface oxygen coverage. The minimum  $E_S$  is predicted for the 2octa123 structure. For surfaces relaxed with an oxygen molecule, as shown in Table 5.2 and Fig. 5.4, a higher sub-surface oxygen coverage makes  $E_S$  decrease. The smallest  $E_S$  is predicted for 2octa1234 FCC. This structure also has the most severe surface restructuring [see Figs. 5.5(e) and 5.5(f)].<sup>3</sup> Comparing the surfaces relaxed with an oxygen molecule (“With O<sub>2</sub>”)

<sup>3</sup>To prevent unrealistically high forces caused by small interatomic distance in the unrelaxed structures, we added 20% to the gap between the top and second copper layer of 2octa1234 FCC and relaxed the structure. An identical surface restructuring was found.



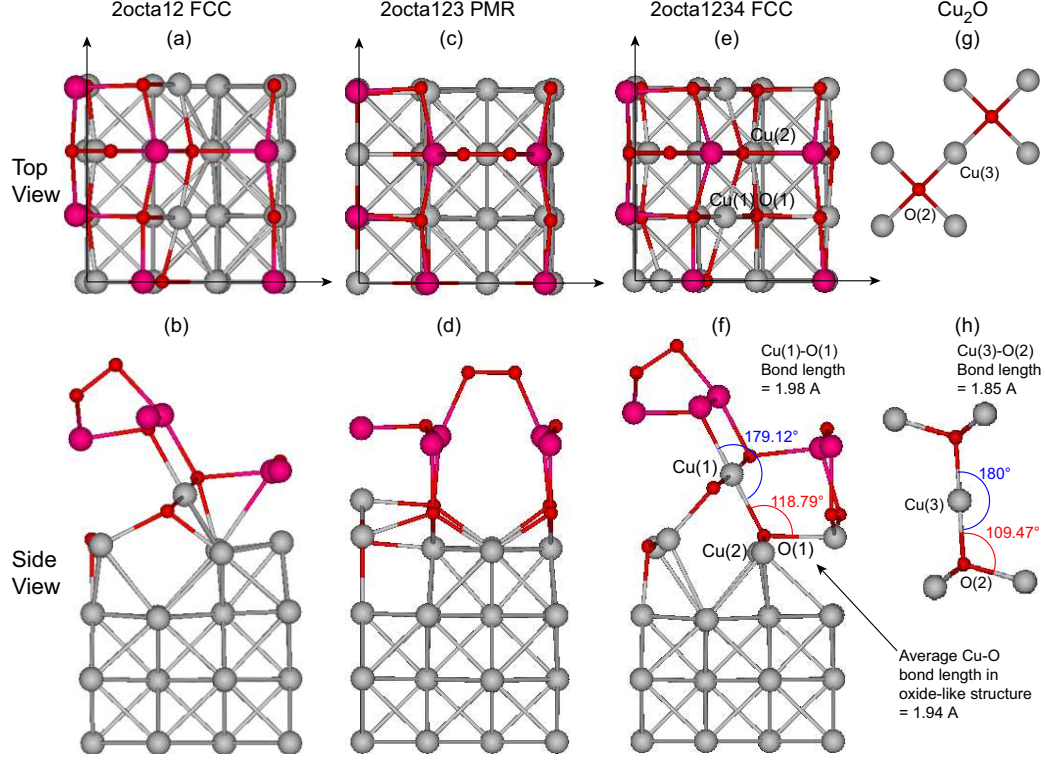


Figure 5.5: Oxygen-molecule induced surface restructuring on the missing-row reconstructed Cu(100) surface with extra on- and sub-surface oxygen atoms: (a) Top and (b) side views of 2octa12 FCC. (c) Top and (d) side views of 2octa123 PMR. (e) Top and (f) side views of 2octa1234 FCC. (g), (h) O-Cu-O bond in bulk  $\text{Cu}_2\text{O}$ . Copyright 2010 Elsevier B.V.

to the surfaces relaxed without an oxygen molecule (“No  $\text{O}_2$ ”) in Fig. 5.4, we find that  $E_S$  decreases more and that there is more severe surface restructuring for 2octa12 FCC and 2octa1234 FCC compared to 2octa123 PMR [see Figs. 5.5(a)-5.5(f)]. Severe surface restructuring thus leads to a more stable structure.

This surface restructuring, as shown in Figs. 5.5(a), 5.5(b), 5.5(e), and 5.5(f), leads to the formation of tetrahedral structures that are similar to the bulk  $\text{Cu}_2\text{O}$  structures shown in Figs. 5.5(g) and 5.5(h). Such tetrahedral structures are only found in 2octa12 FCC and 2octa1234 FCC. The tetrahedral structures found in 2octa1234 FCC have similar bond lengths and bond angles as found in bulk  $\text{Cu}_2\text{O}$ . To check for size effects, we also relaxed the 2octa12 and 2octa1234 structures in the  $p(4\sqrt{2} \times 4\sqrt{2})$  unit-cell with and without an additional oxygen molecule. The tetrahedral structure was

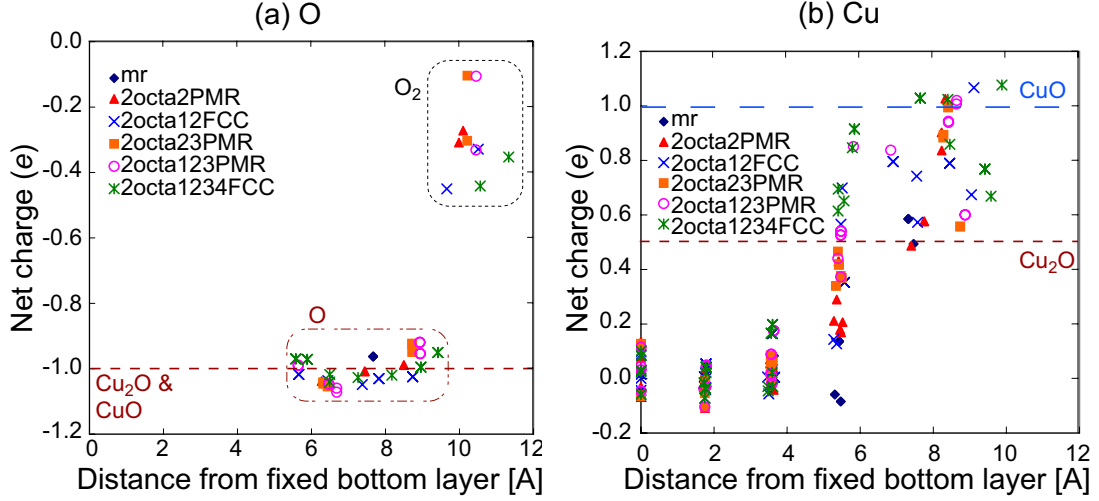


Figure 5.6: Bader net charge vs. position measured from the fixed bottom layer for (a) oxygen and (b) copper atoms in surfaces relaxed with an oxygen molecule at different sub-surface oxygen coverages. The charges for atoms in bulk  $\text{CuO}$  and  $\text{Cu}_2\text{O}$  are provided as dashed lines. Copyright 2010 Elsevier B.V.

observed in both structures. Comparing the  $p(2\sqrt{2} \times 2\sqrt{2})$  and  $p(4\sqrt{2} \times 4\sqrt{2})$  unit-cells in Table 5.2, the bigger unit-cell has a higher  $E_S$  value because there are fewer tetrahedral structures per unit-area.

To further study the  $\text{Cu}_2\text{O}$ -like structures, we now investigate the net charges on the copper and oxygen ions predicted using the Bader decomposition of charge density [104, 105]. We first calculated the charges in bulk  $\text{Cu}_2\text{O}$  (-1.0 for oxygen and 0.5 for copper) and  $\text{CuO}$  (-1.0 for oxygen and 1.0 for copper). We then calculated the charge on all atoms in the missing-row reconstructed surface as the sub-surface oxygen coverage increases. The results are plotted in Figs. 5.6(a) and 5.6(b) versus the position normal to the surface measured from the fixed bottom layer. As seen in Fig. 5.6(a), the oxygen atoms from the additional oxygen molecule have charges between -0.4 and -0.1. The charges on the atomic oxygens are around -1.0, which is the bulk  $\text{Cu}_2\text{O}$  value. The copper charges are shown in Fig. 5.6(b). In the bulk-like copper layers between 0 and 4 Å, the charge is around 0. In the missing-row reconstructed

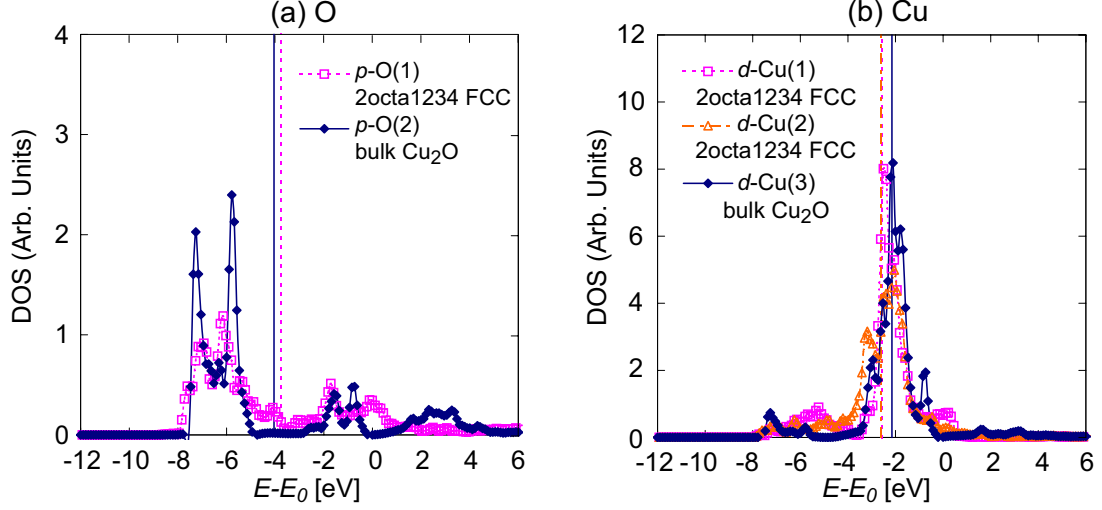


Figure 5.7: Density of states for the (a)  $p$ -O and (b)  $d$ -Cu orbitals in the oxide-like 2octa1234 FCC and bulk  $\text{Cu}_2\text{O}$ . The atomic indices are shown in Figs. 5.5(c), 5.5(d), 5.5(e), and 5.5(f). The average energies of each  $d$ - and  $p$ -orbital ( $d$ -band center and  $p$ -band center) are shown with dashed and solid vertical lines for 2octa1234 FCC and bulk  $\text{Cu}_2\text{O}$ . Copyright 2010 Elsevier B.V.

surface (mr), the copper charge is 0 for the bottom four layers because there is no sub-surface oxygen. In surfaces that contain sub-surface oxygen, the copper charge increases between 4 Å and 6 Å. Above 6 Å, the surface restructuring leads to copper charges between 0.5 and 1.0, a range between the bulk  $\text{CuO}$  and  $\text{Cu}_2\text{O}$  copper charges. This result further confirms the presence of oxide-like structures.

The projected density of state (PDOS) for the oxygen and copper atoms in the 2octa1234 tetrahedral structure [see Figs. 5.5(e) and 5.5(f)] and bulk  $\text{Cu}_2\text{O}$  [see Figs. 5.5(g) and 5.5(h)] are shown in Figs. 5.7(a) and 5.7(b). The oxygen  $p$ -band center and the copper  $d$ -band center are calculated using the first moment of the PDOS referenced to the Fermi level. The results are shown in Figs. 5.7(a) and 5.7(b) as vertical lines. The root mean square (rms) band width is calculated from the square root of the second moment of the PDOS [106].

As shown in Fig. 5.7(a), the PDOS of oxygen  $p$ -orbitals in 2octa1234 FCC and bulk  $\text{Cu}_2\text{O}$  have similar shapes. The rms band widths are 5.52 and 5.20 eV for 2octa1234

FCC and bulk  $\text{Cu}_2\text{O}$ . For the copper  $d$ -orbital, as shown in Fig. 5.7(b), the PDOS of the oxide-like structure (2octa1234 FCC) and bulk  $\text{Cu}_2\text{O}$  also have similar features. The rms band widths for Cu(1) and Cu(2) in 2octa1234 FCC are 3.35 and 3.42 eV, which is comparable to the value of 3.00 eV for bulk  $\text{Cu}_2\text{O}$ . During the transition from 2octa1234 FCC to bulk  $\text{Cu}_2\text{O}$ , the oxygen  $p$ -band center shifts downward by 0.29 eV and the copper  $d$ -band center shifts 0.42 eV upward for Cu(1) and 0.46 eV upward for Cu(2). This trend is opposite to the 0.4 eV downshift that a surface copper atom experiences during the earlier transition from the clean surface to the missing-row reconstruction [35].

### 5.3.3 Unreconstructed Cu(100) surfaces relaxed with an oxygen molecule

The  $(2\sqrt{2} \times \sqrt{2})\text{R}45^\circ$  phase [i.e., the missing-row reconstructed Cu(100) surface] is experimentally observed during Cu(100) oxidation [15, 23, 25, 26, 28, 29, 34, 37, 38]. As shown in Section 5.3.2, DFT calculations predict that  $\text{Cu}_2\text{O}$ -like structures are generated when the missing-row reconstructed Cu(100) surface with sub-surface oxygen atoms is exposed to additional oxygen molecules. No studies have investigated the potential for  $\text{Cu}_2\text{O}$  to form on the unreconstructed Cu(100) surface. To determine if the missing-row reconstruction is a necessary and not just sufficient state in the early stages of Cu(100) oxidation, we will investigate the stabilities and structural changes of unreconstructed Cu(100) surfaces exposed to additional oxygen molecules and compare the results to those from Section 5.3.2. To carry out this investigation, it is not sufficient to only investigate an oxygen coverage of 0.5 ML, as has been done [33, 36]. We therefore relaxed unreconstructed Cu(100) surfaces at 0.25, 0.5, 0.75, and 1.0 ML oxygen coverages with an oxygen molecule located at the initial positions shown in Fig. 5.8(a).

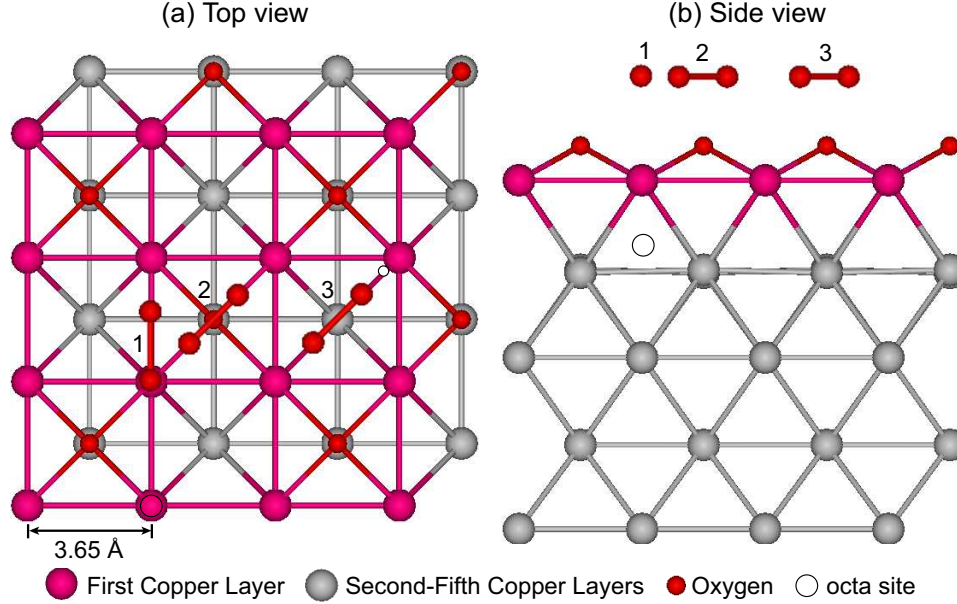


Figure 5.8: Initial positions of the oxygen molecule on the unreconstructed Cu(100) surface before structural relaxation. (a) Top and (b) side view of the unreconstructed  $p(4 \times 4)$  unit cell at 0.5 ML coverage. The initial positions are labeled: 1. Top-bridge (TB), 2. Fcc hollow (FCC), and 3. Unoccupied fcc hollow (UFC). There are 16 octahedral (octa) sites in sub-surface region one of which is shown.

Based on the results from Chapter IV, oxygen embedment into unreconstructed surfaces with 0.25 ML and 0.5 ML oxygen coverage is not highly probable because of high energy barriers (2.65 eV and 2.37 eV) [68]. Hence, sub-surface oxygen is not considered for 0.25 ML and 0.5 ML oxygen coverages. In case of 0.75 ML coverage, however, the energy barrier is 0.49 eV, which makes oxygen embedment is probable, so that we consider sub-surface oxygen. For 1.0 ML coverage, sub-surface oxygen is not considered because 0.75 ML coverage ( $0.047 \text{ eV}/\text{\AA}^2$ ) is more stable than 1.0 ML coverage ( $0.070 \text{ eV}/\text{\AA}^2$ ) and oxygen embedment occurs before oxygen coverage increases until 1.0 ML. For the sub-surface site, we use the octahedral site in the second copper layer, as shown in Fig. 5.8.

As presented in Table 5.3, at 0.25 and 0.5 ML coverages, the surface-oxide energy [Eq. (5.1)] increases except for one case (0.25 ML, UFC), where there is a slight decrease. For oxygen coverages higher than 0.5 ML, however, the surface-oxide energy

Table 5.3: Surface-oxide energy,  $E_S$ , of  $p(4\times 4)$  Cu(100) surfaces without and with an additional oxygen molecule. For each oxygen coverage, the configuration of surface oxygen atoms is chosen so as to minimize the energy [i.e.  $c(2\times 2)$  phase of oxygen for 0.5 ML coverage]. The initial positions of the additional oxygen molecule are the top-bridge (TB), fcc hollow (FCC), and unoccupied fcc hollow (UFC) sites [see Fig. 5.8(a)]. “-” indicates no data (e.g., there is no UFC site at 1.0 ML coverage). For on-surface coverage of 0.6875 ML, one of surface-adsorbed oxygen atoms at 0.75 ML embedded into the sub-surface region and the sub-surface coverage is thus 0.0625 ML (the summation of on- and sub-surface coverage is 0.75 ML). The unit cell area is  $106.58 \text{ \AA}^2$ .

On-surface coverage [ML]	Sub-surface coverage [ML]	No O <sub>2</sub>	$E_S$ [eV/ $\text{\AA}^2$ ]		
			TB	FCC	UFC
0	0	0.184	-	-	-
0.25	0	0.109	0.109	0.118	0.104
0.50	0	0.047	0.053	0.056	0.052
0.75	0	0.047	0.025	0.040	0.037
0.6875	0.0625	0.032	0.024	0.024	0.022
0.75	0.25	-0.027	-0.033	-0.031	-0.029
0.75	0.50	-0.016	-0.029	-0.031	-0.027
1.00	0	0.070	-0.012	-0.014	-

of surfaces with an oxygen molecule (TB, FCC, and UFC) is smaller than that of the surface without an oxygen molecule (No O<sub>2</sub>). The surface-oxide energy decreases (i.e., the stability increases) because of the surface restructuring induced by the oxygen molecule. When the sub-surface oxygen coverage increases for an on-surface coverage of 0.75 ML, the surface-oxide energy is minimized at a sub-surface coverage of 0.25 ML for the “No O<sub>2</sub>” cases. For surfaces with an oxygen molecule, the surface-oxide energy is smaller than that of the “No O<sub>2</sub>” cases. For an on-surface coverage of 0.75 ML and a sub-surface coverage of 0.25 ML, the relaxed structure with an oxygen molecule at the TB position shows the smallest surface-oxide energy.

After the surface restructuring on the unreconstructed Cu(100) surfaces, the top copper layer is elevated and tetrahedral copper-oxygen structures exist. The Cu-O-Cu and O-Cu-O angles range from  $93.18^\circ$  to  $132.15^\circ$  and the Cu-O bond lengths range from  $1.883 \text{ \AA}$  to  $2.388 \text{ \AA}$ . These tetrahedral structures do not have the characteristics of Cu<sub>2</sub>O (Cu-O-Cu and O-Cu-O bond angles are  $109.471^\circ$  and  $180^\circ$ , Cu-O bond length is  $1.849 \text{ \AA}$ ). We also added two oxygen molecules to the unreconstructed

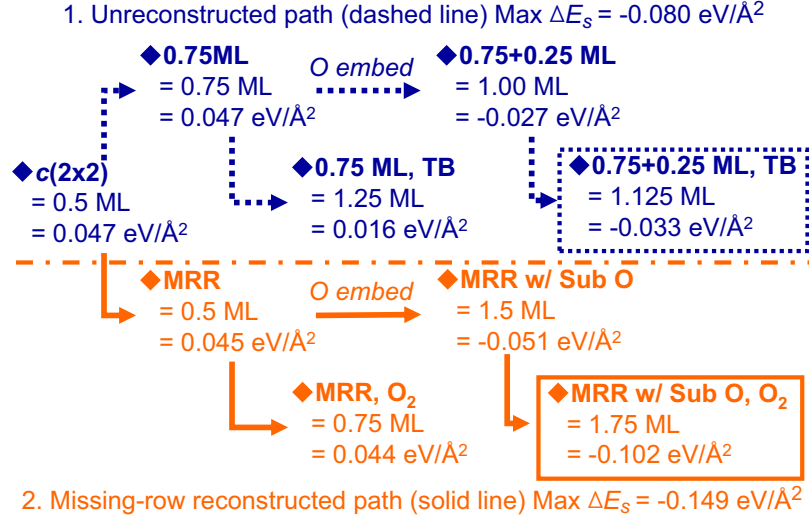


Figure 5.9: Potential oxidation paths on the unreconstructed and missing-row reconstructed Cu(100) surfaces. The surface-oxide energies ( $E_s$ ) are calculated from the  $p(4 \times 4)$  unit cell for the unreconstructed path and from the  $p(2\sqrt{2} \times 2\sqrt{2})$  unit cell for the missing-row reconstructed path. The surface-oxide energies are presented in Table 5.3 for the unreconstructed path. “0.75+0.25 ML” means on-surface coverage 0.75 ML with sub-surface coverage 0.25 ML. For the missing-row reconstructed path, MRR stands for the missing-row reconstructed Cu(100) surface and MRR w/ “Sub O” denotes the missing-row reconstructed Cu(100) surface with sub-surface oxygen. The MRR structures with an oxygen molecule are denoted by O<sub>2</sub>.

surface at 0.75 ML and 1.0 ML oxygen coverages but no Cu<sub>2</sub>O-like structures were produced. In contrast, we showed in Section 5.3.2 that surface restructuring induced by an additional oxygen molecule on the missing-row reconstructed Cu(100) surface can produce Cu<sub>2</sub>O-like structures with comparable bond angles and lengths to that of Cu<sub>2</sub>O when there is sub-surface oxygen.

As shown in Fig. 5.9, there are two potential oxidation paths starting from the  $c(2 \times 2)$  phase. The first path is through the unreconstructed surfaces at an on-surface coverage of 0.75 ML followed by further oxygen exposure. The second path is through the missing-row reconstruction at 0.5 ML oxygen coverage followed by further oxygen exposure. The second path was investigated by our previous report [69]. As we previously reported, oxygen embedment into the subsurface is feasible through the missing-row reconstructed surface at 0.5 ML coverage and also possible

into the unreconstructed Cu(100) surface at 0.75 ML coverage [68]. As such, sub-surface oxygen atom was considered for both the unreconstructed and missing-row reconstructed oxidation paths. The surface-oxide energy eventually decreases along both paths but the magnitude of the drop is much bigger through the missing-row reconstruction path ( $-0.149 \text{ eV}/\text{\AA}^2$ ) than through the unreconstructed path ( $-0.080 \text{ eV}/\text{\AA}^2$ ). This result indicates that the missing-row reconstructed path enhances the structural stability more than the unreconstructed path. Previous investigations did not capture this result because they fixed the oxygen coverage at 0.5 ML [33, 36]. Based on these energetics and structural arguments, we believe that the missing-row reconstruction is a highly probable step for  $\text{Cu}_2\text{O}$  nucleation during Cu(100) oxidation.

## 5.4 Summary

In this chapter, we showed that sub-surface oxygen plays a critical role in the formation of  $\text{Cu}_2\text{O}$ -like structures during the oxidation of a Cu(100) surface. In Section 5.3.1, we demonstrated the likely existence of sub-surface oxygen by comparing our DFT-predicted elevation of the top copper layer to previous STM measurements [see Figs. 5.3(c) and 5.3(d)]. When an oxygen molecule is added to the missing-row reconstructed Cu(100) surface, significant surface restructuring and oxide-like structures are observed when the sub-surface oxygen coverage increases. Such restructuring is not observed in the presence of copper point defects or extra oxygen atoms on the on-surface sites. We find similarity between these structures and bulk  $\text{Cu}_2\text{O}$  by analyzing their structure, net charges, and projected density of states [see Figs. 5.5(e), 5.5(f), 5.6(a), 5.6(b), 5.7(a), and 5.7(b)]. Based on the observed similarities, we believe that an increase in the sub-surface oxygen coverage is the key mechanism by which the



missing-row reconstruction transitions to oxide formation.

In Section 5.3.3, the possibility of oxygen molecule-induced surface restructurings on the unreconstructed Cu(100) surfaces for 0.25, 0.5, 0.75, and 1.0 ML oxygen coverages was tested. The resulting surfaces were compared to similar calculations on the missing-row reconstructed Cu(100) surface with sub-surface oxygen. The surface-oxide energy decrease is two times bigger through the missing-row reconstruction than through the unreconstructed surface. Cu<sub>2</sub>O-like structures are not observed on the unreconstructed Cu(100) surfaces. These results led to the conclusion that the missing-row reconstruction is a necessary step in the formation of Cu<sub>2</sub>O.

The DFT calculations used in Chapters III-V were performed at zero temperature and zero pressure conditions. In the next chapter, we will extend these zero temperature and zero pressure DFT calculations results to finite temperatures and pressures using an *ab-initio* thermodynamics framework.

## CHAPTER VI

### ***Ab-initio* atomistic thermodynamics study of early stages of Cu(100) oxidation**

#### **6.1 Introduction**

In Chapter IV, we used DFT calculations to show that oxygen penetration through the missing row and subsurface diffusion are potential mechanisms for Cu(100) oxidation [68]. In Chapter V, we observed that subsurface oxygen leads to a large increase in the surface stability of the missing-row reconstructed Cu(100) surface and to the formation of Cu<sub>2</sub>O-like structures [69].

To extend these DFT results to finite temperature and pressure conditions, in this chapter, we apply an *ab-initio* atomistic thermodynamics. In this framework, the Gibbs free energy,  $G(T, p)$ , is calculated from DFT energies and the chemical potentials of the surface and gas environment [10, 36, 107–115]. In Section 6.2.1, the computational unit cells, set-up, and procedures for the DFT calculations are presented. We present the *ab-initio* atomistic thermodynamics framework in Section 6.2.2. In Section 6.3.1, we apply the *ab-initio* atomistic thermodynamics framework to the early stages of Cu(100) oxidation (from the clean surface to bulk Cu<sub>2</sub>O) and compare our results with previous experimental [34] and computational results [36]. Then, in Section 6.3.2, we apply the *ab-initio* atomistic thermodynamics framework

to DFT-predicted structures with on- and/or sub-surface oxygen atoms. We find that these structures can be intermediate states between the missing-row reconstruction and bulk  $\text{Cu}_2\text{O}$  formation.

## 6.2 Calculation methodology

### 6.2.1 Density functional theory calculations

We performed the DFT calculations using the Vienna Ab-initio Simulation Package (VASP) [62–66], which uses a plane-wave basis set [64, 66]. We use ultra-soft pseudo potentials, the PW91 generalized gradient approximation [86], and apply a 350 eV energy cutoff. The  $p(2\times 2)$  and  $p(2\sqrt{2}\times 2\sqrt{2})$  unit cells are used. All slab structures include 5 layers (the bottom layer is fixed) and the vacuum size is 11 Å. There are 40 copper and 4 oxygen atoms in the  $p(2\sqrt{2}\times 2\sqrt{2})$  unit cell, the biggest that we consider. For both  $p(2\times 2)$  and  $p(2\sqrt{2}\times 2\sqrt{2})$  unit cells, an  $8\times 8\times 1$   $k$ -point mesh is generated by the Monkhorst-Pack scheme [79].

The density of the  $k$ -point mesh, the energy cutoff, and the number of copper layers are chosen based on convergence tests performed for the  $p(2\sqrt{2}\times 2\sqrt{2})$  missing-row reconstructed surface, which are reported in Chapter V. The energy differences compared to more strict options (600 eV energy cutoff,  $12\times 12\times 1$   $k$ -point mesh, and 8 copper layers), are small (0.005 eV for energy cutoff and  $k$ -point mesh, 0.0008 eV/Å<sup>2</sup> for the number of layers).

### 6.2.2 *Ab-initio* atomistic thermodynamics framework

To study the finite-temperature and -pressure interaction between a Cu(100) surface and a gas phase oxygen environment and to determine the most stable surface structure for each condition, we use the *ab-initio* atomistic thermodynamics framework developed by Reuter et al. [111]. In the *ab-initio* atomistic thermodynamics

framework, the surface is assumed to be in thermodynamical equilibrium with a gas phase environment [36,111]. For the interaction between an oxygen environment and a copper surface, two different approaches have been used. The first is to investigate the transition from the clean copper surface to a bulk  $\text{Cu}_2\text{O}$  structure using bulk fcc copper as the reservoir [36,115]. The second one is to investigate of a  $\text{Cu}_2\text{O}$  slab using bulk  $\text{Cu}_2\text{O}$  as the reservoir [10,114]. In our systems, the surface restructuring happens in the first and second copper layers. The third through bottom layers do not show any dramatic structural changes (i.e., they are similar to bulk fcc copper). Also, we examine the effects of oxygen molecule's pressure and temperature. Hence, we followed the first approach, which uses bulk fcc copper and an isolated oxygen molecule as the reference points.

To compare the stabilities of different surface structures, we use the surface free energy,  $\gamma(T, p_{\text{O}_2})$ ,

$$\gamma(T, p_{\text{O}_2}) = \frac{1}{A_{\text{surf}}} [G(T, p_{\text{O}_2}, N_{\text{Cu}}, N_{\text{O}}) - N_{\text{Cu}}\mu_{\text{Cu}} - N_{\text{O}}\mu_{\text{O}}(T, p_{\text{O}_2})], \quad (6.1)$$

which depends on the Gibbs free energy  $G(T, p_{\text{O}_2}, N_{\text{Cu}}, N_{\text{O}})$ , the number of atoms, and the chemical potentials,  $\mu$ . The surface free energy is normalized by the unit cell area of the sample to allow for comparison of the results from different unit cells sizes. The  $N_{\text{Cu}}\mu_{\text{Cu}}$  term represents the energy cost of exchanging copper atoms between an oxygen-covered surface and bulk fcc copper.  $\mu_{\text{Cu}}$  is therefore equal to the free energy of a copper atom in the fcc bulk phase,  $E_{\text{Cu,bulk}}$  [36]. The Gibbs free energy is

$$G = E_{\text{O/Cu,slab}} + F_{\text{O/Cu,slab}}^{\text{vib.}} - pV, \quad (6.2)$$

which includes the total energy of the oxygen-covered copper surface calculated from DFT ( $E_{\text{O/Cu,slab}}$ ), the Helmholtz free energy due to lattice vibrations ( $F_{\text{O/Cu,slab}}^{\text{vib.}}$ ), and the contribution of pressure and volume change ( $pV$ ) [111]. Because solids are

typically incompressible,  $pV$  is negligible. The contribution of lattice vibrations is 0.002-0.006 eV/Å<sup>2</sup>, as reported by a previous investigation, and is also negligible [115]. Hence, Eq. (6.1) can be rewritten as

$$\gamma(T, p_{O_2}) = \frac{1}{A_{surf}} [E_{O/Cu,slab} - N_{Cu}E_{Cu,bulk} - N_O\mu_O(T, p_{O_2})]. \quad (6.3)$$

The oxygen chemical potential,  $\mu_O(T, p_{O_2})$ , for an ideal gas is

$$\mu_O(T, p_{O_2}) = \frac{1}{2} \left[ E_{O_2} + \mu_{O_2}(T, p^0) + k_B T \cdot \ln\left(\frac{p_{O_2}}{p^0}\right) \right], \quad (6.4)$$

where  $k_B$  is the Boltzmann constant. In our calculation, we set the standard pressure,  $p^0$ , as 1 atm and use the oxygen chemical potential values calculated by Reuter et al. [111] based on the thermochemical tables [116]. For convenience and consistency, the relative oxygen chemical potential,  $\Delta\mu_O(T, p_{O_2})$ , is defined as

$$\Delta\mu_O(T, p_{O_2}) = \mu_O(T, p_{O_2}) - \frac{1}{2}E_{O_2} = \mu_O(T, p^0) + \frac{1}{2}k_B T \cdot \ln\left(\frac{p_{O_2}}{p^0}\right). \quad (6.5)$$

Substituting Eq. (6.5) into Eq. (6.3) and using Eq. (5.1) leads to

$$\gamma(T, p_{O_2}) = E_S - \frac{N_O}{A_{surf}} \cdot \Delta\mu_O(T, p_{O_2}), \quad (6.6)$$

where  $E_S$  is defined in Chapter V, Eq. 5.1. The surface free energy plotted vs. the relative oxygen chemical potential is therefore a straight line with a slope  $-\frac{N_O}{A_{surf}}$ . By comparing the surface free energies calculated by Eq. (6.6) for different structures, we can identify the most stable surface structure for different temperature and pressure conditions.

## 6.3 Results

### 6.3.1 Early stages of Cu(100) oxidation

In this section, we investigate the structures present during the early stages of Cu(100) oxidation, as shown in Figs. 6.1(a)-6.1(n). The structures shown in Figs.

6.1(a)-6.1(e) and 6.1(h) are the experimentally observed clean, 0.25 ML,  $c(2 \times 2)$  [23], missing-row reconstruction (MRR) [26], bulk  $\text{Cu}_2\text{O}$  [117], and missing-row reconstruction with 1/4 disordered vacancy [ $c(2 \times 2)$  w/ 0.25 DV structures] [34]. An upper limit for the relative oxygen chemical potential,  $\Delta\mu_{\text{O}}(T, p_{\text{O}_2})$ , is determined from the heat of formation for bulk  $\text{Cu}_2\text{O}$ ,  $\Delta H_f(\text{Cu}_2\text{O})$ , calculated from

$$\begin{aligned}\Delta H_f(\text{Cu}_2\text{O}) &= H(\text{Cu}_2\text{O}) - H_f(2\text{Cu} + \text{O}), \\ &= \frac{E_{\text{Cu}_2\text{O},\text{bulk}} - N_{\text{Cu}}E_{\text{Cu},\text{bulk}} - N_{\text{O}}\frac{1}{2}E_{\text{O}_2}}{N_{\text{Cu}_2\text{O}}},\end{aligned}\quad (6.7)$$

where  $N_{\text{Cu}_2\text{O}}$  is the number of  $\text{Cu}_2\text{O}$  units in the bulk  $\text{Cu}_2\text{O}$  sample structure and  $E_{\text{Cu}_2\text{O},\text{bulk}}$  is the total energy of the bulk  $\text{Cu}_2\text{O}$  sample. Our calculated heat of formation,  $\Delta H_f(\text{Cu}_2\text{O})$ , -1.24 eV, is consistent with a previous DFT-calculated result [36].

The missing-row reconstruction, Fig. 6.1(d) is the most frequently observed intermediate state before  $\text{Cu}_2\text{O}$  island formation by experiments. At high temperature and low oxygen partial pressure conditions, however, it is experimentally observed that the missing-row reconstruction does not happen and that the  $\text{Cu}(100)$  surface is unreconstructed [34]. We therefore also consider oxygen coverages on the unreconstructed surface higher than 0.5 ML in our stability analysis [Figs. 6.1(f) and 6.1(g)] [57].

During the transition from the missing-row reconstruction to bulk  $\text{Cu}_2\text{O}$  island formation, Iddir et al. reported that there is copper-vacancy exchange above 473 K, which leads to the missing-row reconstruction with 1/4 disordered vacancy structure [ $c(2 \times 2)$  w/ 0.25 DV] [34]. They also observed oxygen desorption from oxygen-covered unreconstructed surfaces. The vacancy affects the surface stability by inducing structural change. To test the effects of copper and/or oxygen vacancies on the stability of the missing-row reconstructed surface, we also investigated the missing-row reconstruction with additional copper and/or oxygen vacancies [Figs. 6.1(i)-6.1(n)].

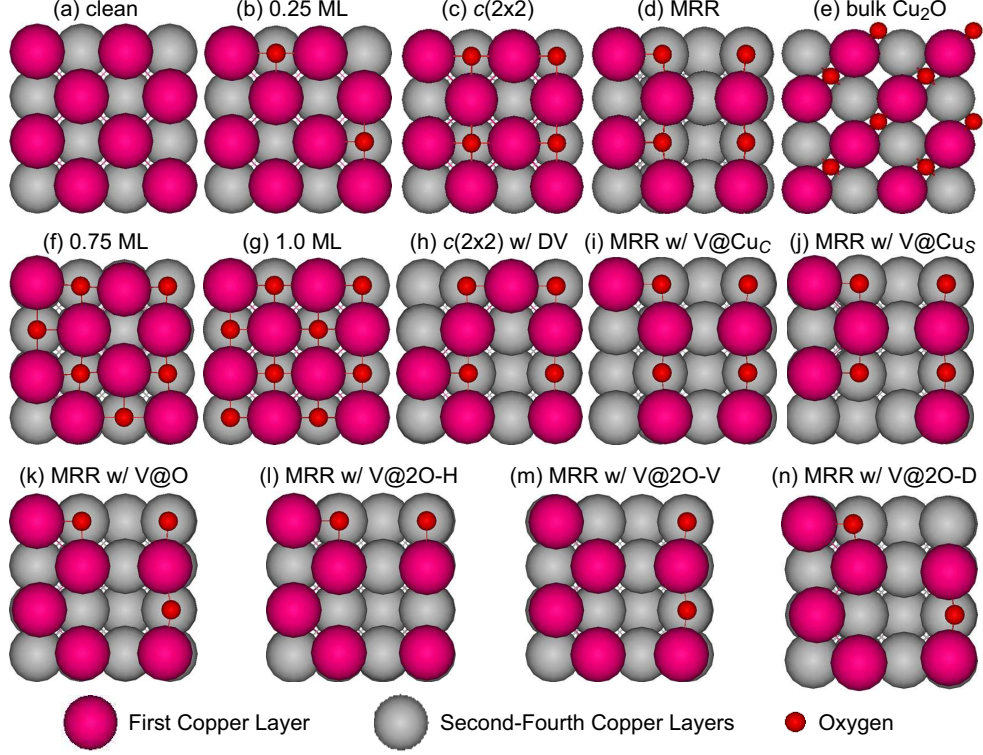


Figure 6.1: Top view of surface structures during the early stages of Cu(100) oxidation: (a) clean surface. (b)  $2 \times 2$  phase at 0.25 ML oxygen coverage. (c)  $c(2 \times 2)$  phase at 0.5 ML oxygen coverage. (d) missing-row reconstruction (MRR). (e) bulk  $\text{Cu}_2\text{O}$ . (f) oxygen coverage 0.75 ML. (g) oxygen coverage 1.0 ML. (h) MRR with vacancy disorder [ $c(2 \times 2)$  w/ 0.25 DV]. MRR with copper vacancy at (i) not adjacent ( $\text{Cu}_C$ ) and (j) adjacent ( $\text{Cu}_S$ ) to the missing row. (k) MRR with an oxygen vacancy. MRR with two oxygen vacancies located (l) horizontally (2O-H), (m) vertically (2O-V), and (n) diagonally (2O-D). All these relaxed structures are visualized using the  $p(2\sqrt{2} \times 2\sqrt{2})$  unitcell.

We applied the *ab-initio* atomistic thermodynamics framework to the structures shown in Fig. 6.1. The surface-oxide energy calculated from DFT ( $E_S$ ), the number of oxygen atoms in the unit cell ( $\#$  of O atoms), and the unit cell area ( $A_{surf}$ ) are provided in Table 6.1. We substituted these values into Eq. (6.6) and then compared the surface free energies,  $\gamma(T, p_{\text{O}_2})$  for different relative oxygen chemical potentials. The structure having the lowest surface free energy is the most stable structure at the given temperature and pressure condition and is therefore expected to be observed in an experiment. As shown in Fig. 6.2(a), we can identify the most stable structure at each relative oxygen chemical potential (related to the temperature and pressure

Table 6.1: Surface-oxide energy,  $E_S$ , for structures in the early stages of Cu(100) oxidation. For each oxygen coverage, the configuration of surface oxygen atoms is chosen so as to minimize the energy [i.e.  $c(2\times 2)$  phase of oxygen for 0.5 ML coverage]. The relaxed structures are shown in Fig. 6.1. The unit cell surface area,  $A_{surf}$ , is  $26.65 \text{ \AA}^2$  for  $p(2\times 2)$  unit cell and  $53.29 \text{ \AA}^2$  for  $p(2\sqrt{2}\times 2\sqrt{2})$  unit cell.

Index	Label in Fig. 6.1	Coverage [ML]	Unit cell	# of O atoms	$E_S$ [eV/ $\text{\AA}^2$ ]
clean	(a)	0.00	$p(2\sqrt{2}\times 2\sqrt{2})$	0	0.184
0.25 ML	(b)	0.25	$p(2\times 2)$	1	0.104
$c(2\times 2)$	(c)	0.50	$p(2\sqrt{2}\times 2\sqrt{2})$	4	0.047
MRR	(d)	0.50	$p(2\sqrt{2}\times 2\sqrt{2})$	4	0.045
0.75 ML	(f)	0.75	$p(2\times 2)$	3	0.047
1.00 ML	(g)	1.00	$p(2\times 2)$	4	0.070
$c(2\times 2)$ w/ DV	(h)	0.50	$p(2\sqrt{2}\times 2\sqrt{2})$	4	0.049
MRR w/ V@Cu <sub>C</sub>	(i)	0.50	$p(2\sqrt{2}\times 2\sqrt{2})$	4	0.051
MRR w/ V@Cu <sub>S</sub>	(j)	0.50	$p(2\sqrt{2}\times 2\sqrt{2})$	4	0.047
MRR w/ V@O	(k)	0.375	$p(2\sqrt{2}\times 2\sqrt{2})$	3	0.087
MRR w/ V@2O-H	(l)	0.25	$p(2\sqrt{2}\times 2\sqrt{2})$	2	0.129
MRR w/ V@2O-V	(m)	0.25	$p(2\sqrt{2}\times 2\sqrt{2})$	2	0.127
MRR w/ V@2O-D	(n)	0.25	$p(2\sqrt{2}\times 2\sqrt{2})$	2	0.125

condition) This information was used to generate the phase diagram shown in Fig. 6.2(b).

As the relative oxygen chemical potential,  $\Delta\mu_O(T, p_{O_2})$  is increased (i.e., by decreasing  $T$  or increasing  $p_{O_2}$ ), the most stable structure transitions from the clean surface (clean), to the 0.25 ML oxygen coverage (0.25 ML), to the missing-row reconstruction (MRR), to the bulk Cu<sub>2</sub>O structure. The  $c(2\times 2)$  phase is always slightly less stable than the missing-row reconstruction. While these two structures have the same number of oxygen atoms [i.e., the same slope in Fig. 6.2(a)], the  $c(2\times 2)$  phase has a slightly higher surface-oxide energy (+0.002 eV/ $\text{\AA}^2$ , see Table 6.1). The unreconstructed Cu(100) surfaces with oxygen coverages higher than 0.5 ML and the missing-row reconstruction with additional copper and/or oxygen vacancies are not observed to be the most stable structure at any temperature/pressure condition but could still exist locally over short times. The phase transitions happen at  $\Delta\mu_O(T, p_{O_2})$  values of -2.14 eV (clean-0.25 ML), -1.57 eV (0.25 ML-MRR), and -1.24 eV (MRR-



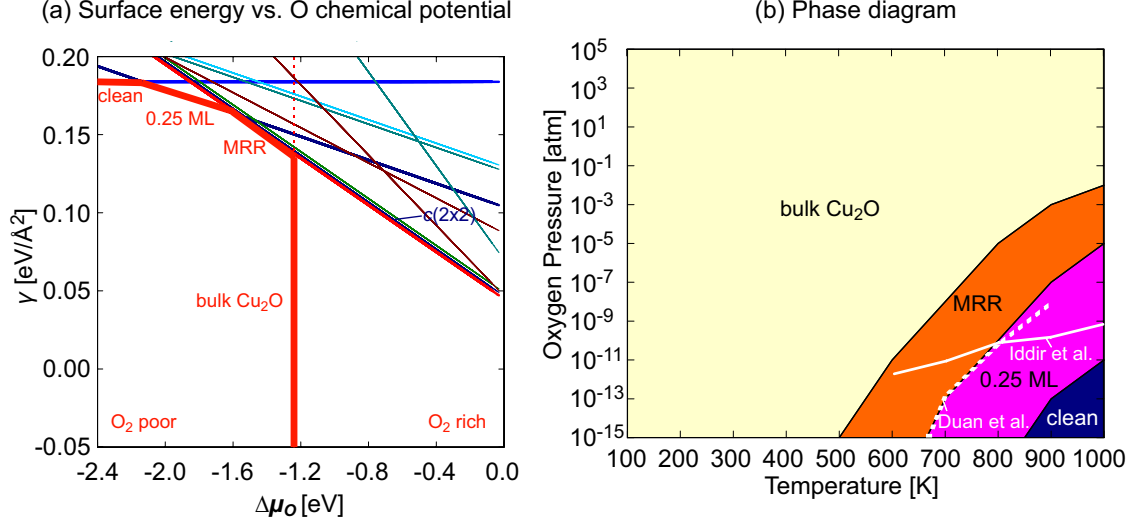


Figure 6.2: (a) Surface free energy  $[\gamma(T, p_{O_2})]$  of the early stages of Cu(100) oxidation as a function of the relative oxygen chemical potential ( $\Delta\mu_O$ ). (b) Phase diagram predicted from Fig. 6.2(a) [these structures are shown in Figs. 6.1(a), 6.1(b), 6.1(d), and 6.1(e)]. The phase boundaries between 0.25 ML and MRR from an experiment (Iddir et al.) and a previous *ab-initio* thermodynamics calculation (Duan et al.) are shown for comparison.

bulk Cu<sub>2</sub>O). Our transition values of  $\Delta\mu_O(T, p_{O_2})$  are slightly different with those of Duan et al. (-1.89 eV for the clean-0.25 ML and -1.72 eV for the 0.25 ML-MRR) [36] because of different basis sets and computational packages, but we predict the same surface structures to be stable. In the phase diagram shown in Fig. 6.2(b), the oxygen environment changes from oxygen-poor (lower-right corner) into oxygen-rich (upper-left corner) condition. As the oxygen environment changes, the clean Cu(100) surface is covered by atomic oxygen and the oxygen coverage increases until 0.25 ML. When  $c(2 \times 2)$  phases with coverage of 0.5 ML form locally, they are transformed into the missing-row reconstruction (MRR) [23,31] and the  $c(2 \times 2)$  phase is therefore not shown in the phase diagram. If the oxygen environment changes into a more oxygen-rich condition, the Cu<sub>2</sub>O islands nucleate on the missing-row reconstructed surface and eventually bulk Cu<sub>2</sub>O forms. The phase diagram includes four distinct states (clean, 0.25 ML, MRR, and bulk Cu<sub>2</sub>O), consistent with previous experimental and theoretical results [34,36]. For comparison, the 0.25 ML-MRR phase boundaries from

experiment (Iddir et al. [34]) and the *ab-initio* thermodynamics framework (Duan et al. [36]) are shown in Fig. 6.2(b). The experimentally observed phase boundary (Iddir et al.), however, is different with ours because of uncertainties in experimental measurements and in the DFT calculations. Although there is difference of the oxygen partial pressure range for the 0.25 ML-MRR phase boundary between ours and an experiment (Iddir et al. [34]), the temperatures range matches well. In addition, our results agree quantitatively with the *ab-initio* thermodynamics framework result of Duan et al. [36].

### 6.3.2 Stable intermediate states from missing-row reconstruction to bulk $\text{Cu}_2\text{O}$ formation

Although we predicted the stable structures during the early stages of Cu(100) oxidation in Section 6.3.1, the results are not sufficient to explain the mechanism of  $\text{Cu}_2\text{O}$  formation. In Chapter V, we proposed various missing-row reconstructed structures with on- or sub-surface oxygen atoms and demonstrated that a  $\text{Cu}_2\text{O}$ -like structure is formed on the missing-row reconstructed structures when sub-surface oxygen is present [68, 68]. All the reported results, however, are from the DFT calculations, and are valid only at zero-temperature and zero-pressure. To test if the DFT-predicted structures can be stable intermediate states between the missing-row reconstruction and the bulk  $\text{Cu}_2\text{O}$  formation at finite temperature and pressure conditions, we need to analyze them in the *ab-initio* thermodynamics framework.

As candidates for the intermediate states between the missing-row reconstruction and bulk  $\text{Cu}_2\text{O}$  formation, we investigate the missing-row reconstruction with extra on-surface oxygen [Figs. 6.3(a)-6.3(c)] and the missing-row reconstruction with extra sub-surface oxygen [Figs. 6.3(d)-6.3(l)]. We calculated the surface-oxide energy for each structure with an additional oxygen molecule in Chapter V. For our *ab-initio*

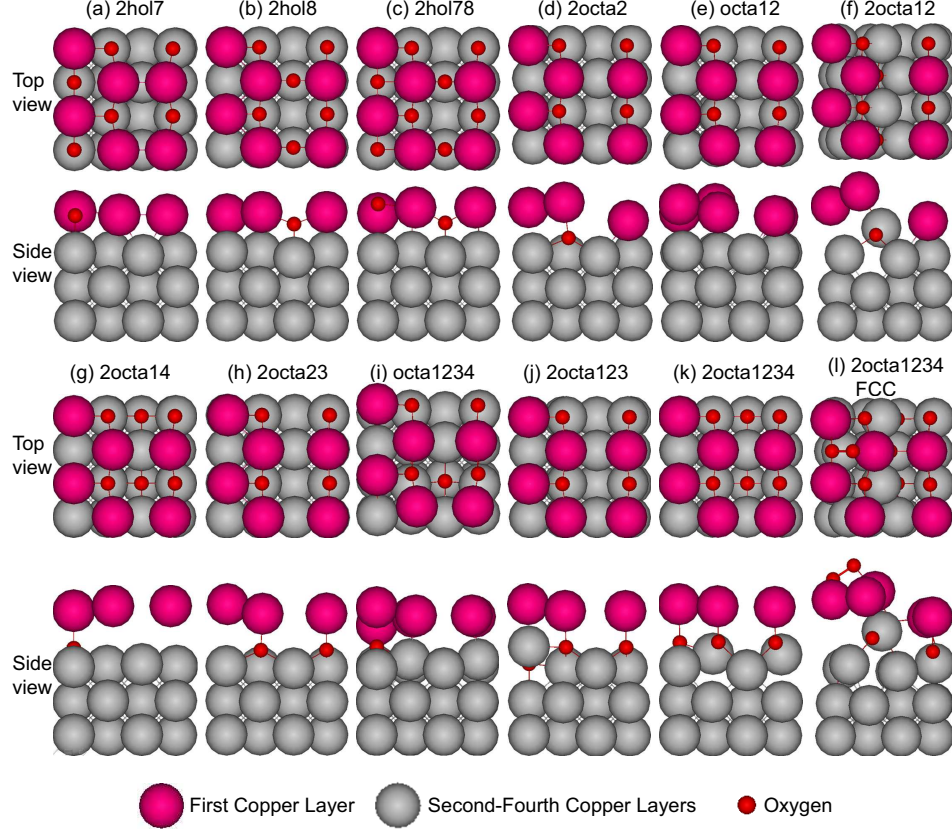


Figure 6.3: Top and side views of relaxed structures that may exist between the missing-row reconstruction (MRR) and bulk  $\text{Cu}_2\text{O}$  nucleation: MRR with additional on-surface oxygen atoms at (a) two hol7 sites (2hol7), (b) two hol8 sites (2hol8), and (c) two hol7 and hol8 sites (2hol78). MRR with additional sub-surface oxygen atoms at (d) two octa2 sites, (e) octa1 and octa2 sites, (f) two octa1 and octa2 sites, (g) two octa1 and octa2 sites, (h) two octa2 and octa3 sites, (i) octa1-4 sites, (j) two octa1-3 sites, (k) two octa1-4 sites, and (l) two octa1-4 sites with an oxygen molecule at FCC site (hol and octa sites are specified in Chapter V). Although (a)-(j) structures with an additional oxygen molecule are included in our *ab-initio* thermodynamics framework investigation, we show the only meaningful case, (l), here.

thermodynamics framework investigation, we tested all the results but show only the case that led to a  $\text{Cu}_2\text{O}$ -like structure [Fig. 6.3(l)].

We applied the *ab-initio* atomistic thermodynamics framework to these structures and the results are shown in Figs. 6.4(a) and 6.4(b). The surface-oxide energy ( $E_S$ ) and number of oxygen atoms in unit cell (# of oxygen) are provided in Table 6.2.

As shown in Fig. 6.4(a), we found the most stable structure as a function of the relative oxygen chemical potential,  $\Delta\mu_O(T, p_{O_2})$ . Below the bulk  $\text{Cu}_2\text{O}$  limit [see

index	label in Fig. 6.3	Coverage [ML]	Unit cell	# of oxygen	$E_S$ [eV/Å <sup>2</sup> ]
2hol7	(a)	0.75	$p(2\sqrt{2}\times 2\sqrt{2})$	6	0.006
2hol8	(b)	0.75	$p(2\sqrt{2}\times 2\sqrt{2})$	6	0.039
2hol78	(c)	1.00	$p(2\sqrt{2}\times 2\sqrt{2})$	8	0.003
2octa2	(d)	0.75	$p(2\sqrt{2}\times 2\sqrt{2})$	6	0.010
octa12	(e)	0.75	$p(2\sqrt{2}\times 2\sqrt{2})$	6	0.022
2octa12	(f)	1.00	$p(2\sqrt{2}\times 2\sqrt{2})$	8	-0.016
2octa14	(g)	1.00	$p(2\sqrt{2}\times 2\sqrt{2})$	8	-0.012
2octa23	(h)	1.00	$p(2\sqrt{2}\times 2\sqrt{2})$	8	-0.030
octa1234	(i)	1.00	$p(2\sqrt{2}\times 2\sqrt{2})$	8	-0.005
2octa123	(j)	1.25	$p(2\sqrt{2}\times 2\sqrt{2})$	10	-0.057
2octa1234	(k)	1.50	$p(2\sqrt{2}\times 2\sqrt{2})$	12	-0.051
2octa1234 FCC	(l)	1.75	$p(2\sqrt{2}\times 2\sqrt{2})$	14	-0.102

Table 6.2: Surface-oxide energy,  $E_S$ , of potential intermediate states between missing-row reconstruction and bulk  $\text{Cu}_2\text{O}$  nucleation. The relaxed structures are shown in Fig. 6.3. The index notation is explained in Chapter V. The unit cell surface area,  $A_{surf}$ , is 53.29 Å<sup>2</sup> for  $p(2\sqrt{2}\times 2\sqrt{2})$  unit cell.

the dash line in Fig. 6.4(a)], we predicted the same stable structures (clean, 0.25 ML, and MRR) found in Section 6.3.1. Above the bulk  $\text{Cu}_2\text{O}$  limit, however, we observe that the missing-row reconstructions with extra on- or sub-surface oxygen atoms (2hol7, 2octa23, 2octa123, and 2octa1234 FCC) are the most stable structures. Based on these findings, we produced the phase diagram shown in Fig. 6.4(b). In oxygen-poor conditions (i.e., high temperature and low oxygen partial pressure), the clean, 0.25 ML, and MRR states are still more stable than others. Increasing  $\Delta\mu_O(T, p_{O_2})$  (from oxygen-poor to oxygen-rich conditions), the missing-row reconstruction (MRR) changes into MRR with extra on-surface oxygen (2hol7) and then becomes MRR with sub-surface oxygen (2octa23, 2octa123, and 2octa1234FCC). The phase transitions happen at -1.04 eV (MRR-2hol7), -0.96 eV (2hol7-2octa23), -0.70 eV (2octa23-2octa123), and -0.61 eV (2octa123-2octa1234 FCC). These findings indicate that as an oxygen-poor environment changes into an oxygen-rich environment, the missing-row reconstruction gradually allows extra on-surface oxygen adsorption, the sub-surface oxygen coverage increases, and then  $\text{Cu}_2\text{O}$  structures form on the

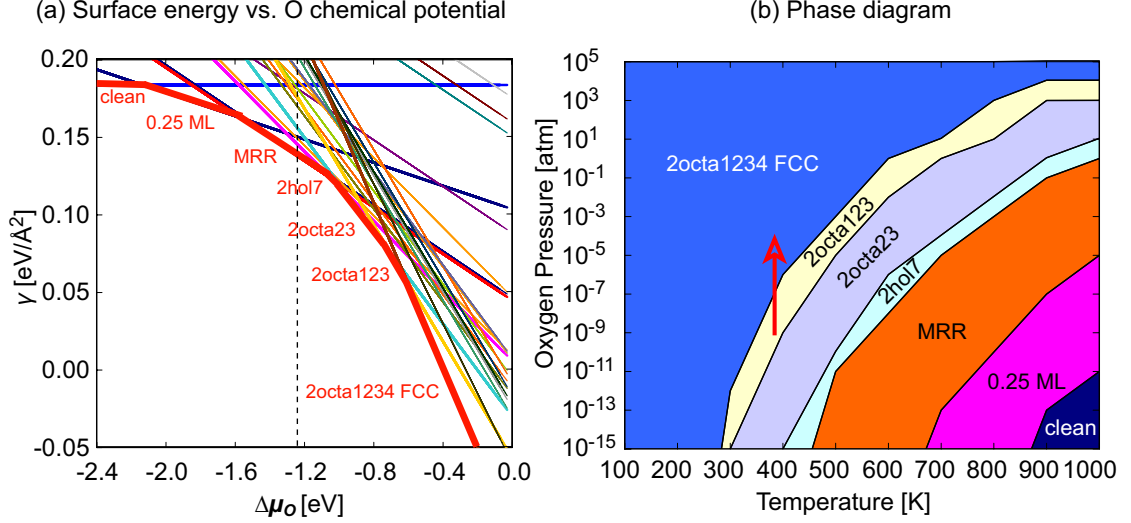


Figure 6.4: (a) Surface free energy ( $E_S$ ) of early stages of Cu(100) oxidation including intermediate states between the missing-row reconstruction and the bulk Cu<sub>2</sub>O formation as a function of oxygen chemical potential ( $\Delta\mu_o$ ) (the bulk Cu<sub>2</sub>O limit, -1.24 eV, is provided by a dashed line), and (b) Phase diagram predicted from Fig. 6.4(a) [these structures are shown in Figs. 6.3(a), 6.3(h), 6.3(j), and 6.3(l)]. The arrow points out the transition observed by Lahtonen et al. as shown in Fig. 6.5.

missing-row reconstructed surface.

Our finding is supported by the experimental results of Lahtonen et al. [38], which are reproduced in Fig. 6.5. As the oxygen partial pressure is increased significantly from  $7.89 \times 10^{-10}$  atm ( $8.0 \times 10^{-7}$  mbar) to  $3.65 \times 10^{-5}$  atm ( $3.7 \times 10^{-2}$  mbar) at 373 K, the well-ordered missing-row reconstructed surfaces are observed and the amount of oxygen on the surface increases slightly (from 0.4 ML to 0.6 ML). There is no evidence of further oxidation. After an oxygen exposure of  $6.0 \times 10^5$  L, the missing-row reconstructed surface becomes very reactive to further oxidation, oxygen penetration is observed, and disordered Cu<sub>2</sub>O structures form on the missing-row reconstruction. Although our simplified structures are not exactly the same as what Lahtonen et al. found, our missing-row reconstruction with extra on-surface oxygen [see Fig. 6.3(a)] is comparable to their inert missing-row reconstructed surface. Also, our missing-row reconstructions with extra sub-surface oxygen [see Figs. 6.3(h), 6.3(j), and 6.3(l)] are comparable to their surfaces including oxygen penetrations and aggressive Cu<sub>2</sub>O for-

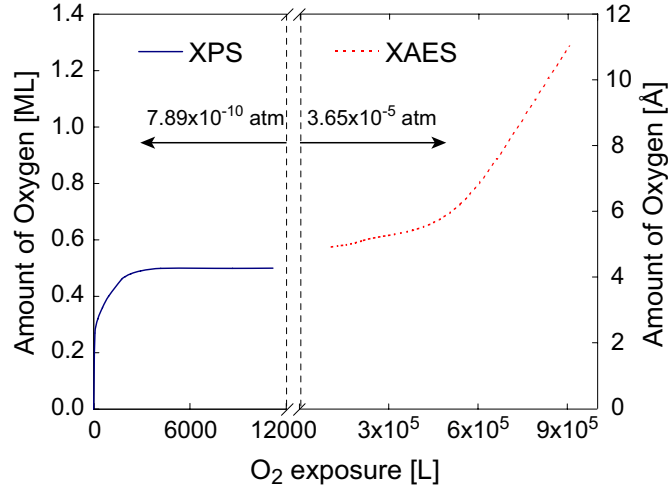


Figure 6.5: Average thickness of oxide layer on Cu(100) surface at 373 K reproduced using the data of Lahtonen et al. For the vertical axis, 0.5 ML coverage in the  $\text{O}_2$  pressure  $7.89 \times 10^{-10}$  atm ( $8.0 \times 10^{-7}$  mbar) corresponds to 4 Å in the oxygen partial pressure  $3.65 \times 10^{-5}$  atm ( $3.7 \times 10^{-5}$  mbar). The Cu(100) surface at 0.5 ML oxygen coverage is fully missing-row reconstructed  $[(2\sqrt{2} \times \sqrt{2})\text{R}45^\circ]$ . The  $\text{O}_2$  pressure regimes ( $7.9 \times 10^{-10}$  atm and  $3.7 \times 10^{-5}$  atm) are separated by the break.

mation. Finally, we put the temperature (373 K) and pressure ( $7.89 \times 10^{-10}$  atm and  $3.65 \times 10^{-5}$  atm) conditions used by Lahtonen et al. to our phase diagram using arrow as shown in Fig. 6.4(b). The result shows that the experimentally observed transition happens across the boundary between the missing-row reconstructed Cu(100) surface including sub-surface oxygen and  $\text{Cu}_2\text{O}$ -like structure produced by our *ab-initio* thermodynamics framework, indicating that our prediction is comparable to the experimental result.

## 6.4 Summary

We applied the *ab-initio* atomistic thermodynamics framework to DFT-predicted surface structures to investigate phase transitions during the early stages of Cu(100) oxidation. This framework allows for the consideration of finite temperature and pressure conditions not accessible with DFT.

In Section 6.3.1, we confirmed that the most stable structures during the early

stages of Cu(100) oxidation are clean, 0.25 ML oxygen coverage, missing-row reconstruction, and bulk Cu<sub>2</sub>O nucleation. Our predictions are consistent with previous experimental [34] and theoretical results [36]. We also tested unreconstructed surfaces with higher oxygen coverage and additional copper and/or oxygen vacancies on the missing-row reconstructed surface. None of these structures are favored in the ranges of 100 - 1000 K and  $10^{-15}$  -  $10^5$  atm.

In Section 6.3.2, we investigated the stability of DFT-predicted missing-row reconstruction structures including extra on- or sub-surface oxygen atoms. We found that these structures are predicted to be the most stable structures at certain temperature and pressure conditions. Based on this result, we inferred the transition mechanism from missing-row reconstruction (MRR) to Cu<sub>2</sub>O nucleation, which agrees qualitatively with a previous experimental observation [38].

## CHAPTER VII

### Summary of contributions and suggested directions for future work

#### 7.1 Summary of contributions

The objective of this thesis research was to identify the transition mechanisms during the early stages of Cu(100) oxidation using DFT calculations. In Chapter II, the DFT-predicted missing-row reconstruction was validated using experimentally measured structural parameters and the most stable oxygen adsorption structure on the Cu(100) surface was determined. In Chapter III, the  $c(2\times 2)$  to missing-row reconstruction was studied. Energetically favorable copper ejection and diffusion paths were identified using the NEB method [67]. In Chapters IV and V, the transition from the missing-row reconstruction to Cu<sub>2</sub>O island nucleation was investigated [68, 69]. In Chapter VI, the transition mechanisms found in Chapters III-V were validated for finite temperature and pressure condition using an *ab-initio* thermodynamics framework [70]. In this chapter, the major contributions are summarized and future research directions are discussed.

- **$c(2\times 2)$ -missing-row reconstruction transition mechanism**

By comparing the stability increases induced by an additional oxygen molecule on a wide range of unreconstructed and missing-row reconstructed surfaces, we found



that the missing-row reconstructed surface is necessary in the Cu(100) oxidation process. Using the NEB method, we investigated the  $c(2\times 2)$ -missing-row reconstruction transition by identifying copper ejection and diffusion paths and their energy barriers, which are comparable to experimentally measured activation energies and diffusion barriers. We found that the presence of a copper adatom decreases the energy barrier by 0.54 eV. Using transition state theory based on the harmonic approximation, we calculated the crossover temperature from coordinated (two copper atoms eject together) to non-coordinated ejection (copper atoms eject one by one) for two ejection paths (343 K for A $\rightarrow$ C and 356 K for A $\rightarrow$ D). Because Cu(100) oxidation experiments are performed at temperatures of 450 K or higher, we inferred that the missing-row reconstruction is formed by non-coordinated ejection. The predicted diffusion barriers of an ejected copper atom near the missing row are comparable to that of copper adatom on the perfect  $c(2\times 2)$  phase and on the clean Cu(100) surface, indicating that the  $c(2\times 2)$  phase can act a copper diffusion channel, a mechanism proposed by earlier STM observations [38]. Our investigation is the first about the  $c(2\times 2)$ -missing-row reconstruction mechanism and increases the understanding of the formation of the missing-row reconstruction both kinetically and energetically. In the future, these results can be used to generate input parameters for a Kinetic Monte Carlo (KMC) simulation package, TFOx [118], that can simulate surface oxide and thin film formation for larger length scales and longer time scales, allowing for eventual comparison with *in-situ* UHV-TEM observations.

- **Missing-row reconstruction-Cu<sub>2</sub>O transition mechanism**

Next, we investigated the missing-row reconstruction-Cu<sub>2</sub>O transition using DFT calculations and the NEB method. To explain surface oxide growth into the sub-

strate [41, 42], atomic oxygen embedment into the Cu(100) surface was tested for different oxygen coverages on the unreconstructed surface and at a fixed oxygen coverage on different surface morphologies. On the unreconstructed surface, as oxygen coverage increases from 0.25 ML to 0.75 ML, embedment becomes more probable and the energy barrier is 2.65 eV at 0.25 ML and 0.49 eV at 0.75 ML. At a fixed oxygen coverage of 0.5 ML, reconstructed surfaces [e.g., missing-row reconstruction,  $c(2\times 2)$  phase with 1/4 vacancy disorder] are more favorable for oxygen embedment (those energy barriers are 1.55 eV and 1.43 eV) than the unreconstructed surface [ $c(2\times 2)$  phase](the energy barriers is 1.96 eV). On the missing-row reconstructed surface, we found that the energy barriers of oxygen embedment through missing row paths (0.26-0.44 eV) are much smaller than those through non-missing-row paths (0.86-1.28 eV). We also found that oxygen atoms can diffuse in between sub-surface octahedral sites. The energy barrier for sub-surface diffusion (0.25-0.78 eV) is comparable to or less than that of on-surface oxygen diffusion (0.74 eV) [20]. Based on these results, we proposed that atomic oxygen embedment and sub-surface diffusion are potential transition mechanisms from the missing-row reconstruction to  $\text{Cu}_2\text{O}$  nucleation. The missing-row reconstructed surfaces with sub-surface oxygen induce a 1.7 Å elevation of the top copper layer, which is comparable to an earlier experimental measurement of 1.8 Å [37]. We also investigated oxygen molecule-induced surface restructuring on the DFT-predicted missing-row reconstructed surfaces with extra on- or sub-surface oxygen and found that  $\text{Cu}_2\text{O}$ -like structures form only on the surfaces with sub-surface oxygen. Showing the similarities of structure (bond length and angle), electronic density of states, and atomic net charges to those of bulk  $\text{Cu}_2\text{O}$ , we confirmed that our DFT-predicted structures have a  $\text{Cu}_2\text{O}$ -like nature. Our proposed missing-row reconstruction- $\text{Cu}_2\text{O}$  transition mechanism and atomic level energetic and structural

information are complementary to experimental observations and will help to understand Cu<sub>2</sub>O island formation at the atomic level. Those energy barriers and relaxed structures are also key input parameters for the KMC simulation package TFOx [118].

- *Ab – initio* thermodynamics framework for early stages of Cu(100) oxidation

The DFT calculations in Chapters III-V are based on zero temperature and zero pressure. To extend our findings to finite temperature and pressure conditions, we applied an *ab – initio* atomistic thermodynamics framework and investigated phase transitions during the early stages of Cu(100) oxidation. We predicted that clean, 0.25 ML oxygen coverage, missing-row reconstruction, and bulk Cu<sub>2</sub>O nucleation are the most stable structures for finite temperature and pressure environments, consistent with previous experimental [34] and theoretical results [36]. During this investigation, we found that higher oxygen coverages on the unreconstructed surface and additional copper and/or oxygen vacancies on the missing-row reconstructed surface do not increase the stability in the range of 100 - 1000 K and 10<sup>-15</sup> - 10<sup>5</sup> atm. Next, we confirmed that our proposed transition mechanism from the missing-row reconstruction to Cu<sub>2</sub>O nucleation is valid for the same temperature and pressure ranges. We then compared surface free energies for our DFT-predicted missing-row reconstruction structures including extra on- or sub-surface oxygen atoms with respect to experimentally observed early stages of Cu(100) oxidation (clean, 0.25 ML, and MRR). For decreasing temperature and increasing oxygen pressure, we found that the most stable structure changes from the clean surface to 0.25 ML to MRR, and then to missing-row reconstructions with extra on-surface and sub-surface oxygen. These results demonstrate that our proposed transition mechanism from the missing-row reconstruction to Cu<sub>2</sub>O nucleation are consistent with a previous experimental

observation [38].

## 7.2 Future research directions

### 7.2.1 Development of DFT-based Kinetic Monte Carlo simulation

Kinetic Monte Carlo (KMC) simulation is a technique for investigating the time evolution of physical or chemical events with known initial and final states [97–101]. Using KMC simulation, the Lattice Gas (LG) model has been successfully used for determining the kinetics of atomistic reactions and diffusions during thin film growth [119–123]. LG-KMC is able to simulate larger length and longer time scales than DFT calculations and molecular dynamics (MD) simulations. It is therefore a powerful method for studying atomic phenomena involving thermally activated diffusions. During LG-KMC simulation, atoms are located at discrete points on a lattices. When an atom has enough thermal energy to overcome the energy barrier for a certain event (e.g., diffusion), the event happens. The rate of this transition (i.e., the reaction rate) can be determined by transition state theory (TST) [93]. To predict transition rates and perform LG-KMC, input parameters (energy barriers, initial and final states) are required. To produce these input parameters, (i) semi-empirical potentials [123–125], (ii) model (pseudo) potentials [98, 101, 118, 126–132], (iii) lookup tables created in local environments [95, 133, 134], and (iv) DFT calculations [99, 135–145] have been applied. Although methods (i)–(iii) can capture the general trends of film growth, atomic resolution predictions of diffusion and island growth are limited because of the many required approximations and a lack of physically reliable information about activation energies and structures. As discussed in Chapter II, DFT is a first principle calculation, which can predict physically reliable energies and relaxed structures. Therefore, the LG-KMC using DFT predicted input parameters (DFT-KMC) is an

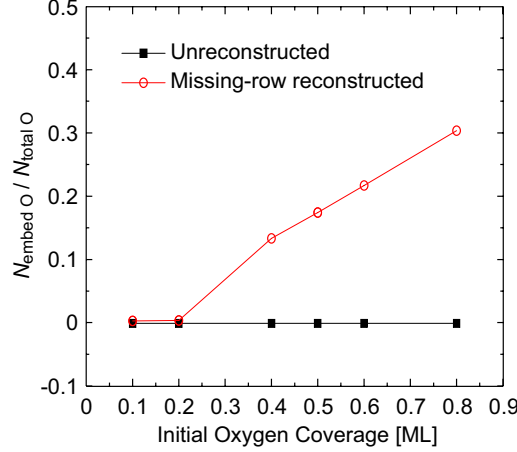


Figure 7.1: Number ratio between embedded oxygen atoms ( $N_{\text{embed O}}$ ) and total number of oxygen atoms ( $N_{\text{total O}}$ ) vs. initial oxygen coverages on a Cu(100) surface during DFT-based Lattice Gas kinetic Monte Carlo (LG-KMC) simulations. Data and graph courtesy of Dr. Sang eun Jee.

attractive technique.

In this thesis research, we focused on identifying transition mechanisms and quantifying their kinetic and energetics (e.g., predicting intermediate structures and energy barriers). These results were used as input parameters for a LG-KMC simulation to describe oxygen embedment into the unreconstructed and missing-row reconstructed Cu(100) surfaces. The results are shown in Fig. 7.1. The horizontal axis shows the oxygen coverage at the beginning of the LG-KMC simulation and the vertical axis is the ratio between the number of oxygen atoms in the sub-surface region ( $N_{\text{embed O}}$ ) and total number of oxygen atoms in the computational cell ( $N_{\text{total O}}$ ). As the initial oxygen coverage increases, the ratio  $N_{\text{embed O}}/N_{\text{total O}}$ , does not change for the unreconstructed surface but increases for the missing-row reconstructed surface at 0.2 ML or higher oxygen coverages. This result indicates that the oxygen embedment, which is important for the formation of oxide-like structures, only occurs on the missing-row reconstructed surface, consistent with previous experimental observation [37] and DFT investigation [69]. These preliminary results show the potential for DFT-based LG-KMC to describe Cu(100) oxidation. To develop a LG-KMC formulation that

can be compared to UHV-TEM measurements, however, requires a large database of input parameters. More DFT-based investigations (e.g., predicting energy barriers and relaxed structures) are required, including:

- Oxygen molecule dissociation on (i) unreconstructed surfaces at oxygen coverages up to 0.5 ML and (ii) missing-row reconstructed surfaces.
- Effects of steps and kinks on oxygen molecule dissociation, oxygen atom diffusion, and copper-vacancy exchange.
- Effects of an ejected copper atom on oxygen molecule dissociation and oxygen atom (on- and sub-surface) diffusion.
- Copper-vacancy exchanges on missing-row reconstructed surface including extra on- and/or sub-surface oxygen atoms.
- Uphill and downhill diffusion of copper and oxygen atoms.
- Mobility of  $\text{Cu}_2\text{O}$  clusters.

### 7.2.2 Investigation of Cu(110) surface

The Cu(110) surface displays different adsorption and reconstruction phenomena compared to the Cu(100) surface, as observed by experiments [41, 42, 44, 46, 146, 147] and as predicted by DFT calculation [16, 52, 148, 149]. For example, the oxygen adsorption sites [149][see Figs. 7.2(a) and 7.2(b)] are very different with respect to the Cu(100) surface. This difference affects the energetics of oxygen adsorption and the oxygen-induced surface reconstruction on the Cu(110) surface. For the Cu(110) surface, the most stable adsorption site is the long bridge site (lb) for atomic oxygen [52] and the four-fold hollow site for the molecular oxygen (predicted by DFT calculations) [16].

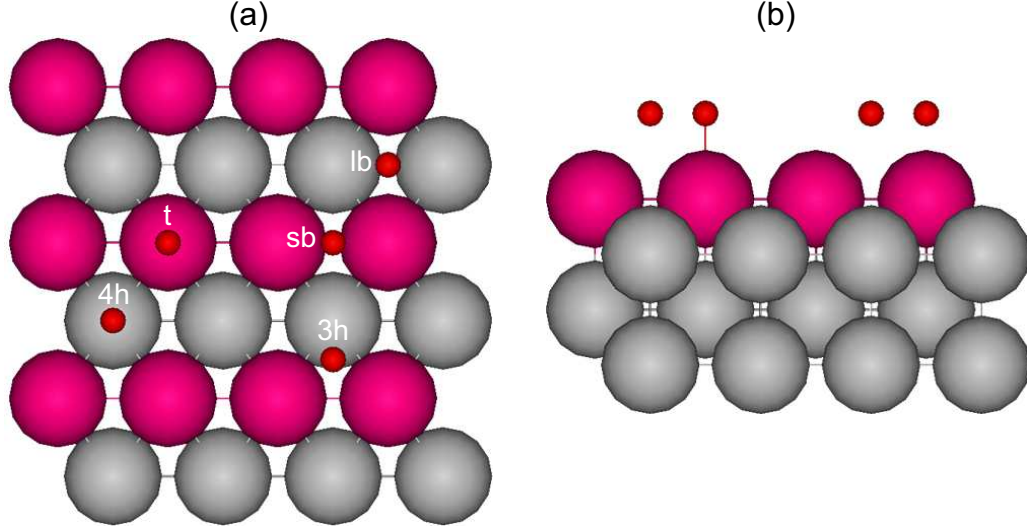


Figure 7.2: (a) Adsorption sites on the Cu(110) surface (3h: three-fold hollow site, 4h: four-fold hollow site, t: top site, sb: short bridge site, lb: long bridge site). (b) Side view of the Cu(110) surface. The topmost copper layer is colored differently.

Kuk et al. explained the mechanism for the transition from the added-row to the missing-row reconstruction [147], which is the saturated oxygen covered reconstruction of the added-row model on the Cu(110) surface, as shown in Fig. 7.3. According to Kuk et al., a diffusing copper atom moves along  $[1\bar{1}0]$  direction [see Figs. 7.3(a), and 7.3(b)], the copper atom is bound to the diffusing oxygen atoms, and then the oxygen atoms are adsorbed in the preferred long bridge site. This reaction is repeated and then the Cu(110) surface is reconstructed as the missing-row reconstruction at the saturated oxygen coverage. By DFT calculation, it is found that the added-row and missing-row reconstruction makes the Cu(110) surface energetically more stable than unreconstructed surface [52]. If more oxygen atoms are supplied to the reconstructed Cu(110) surface, the copper oxide is formed and grown horizontally and vertically, as observed by STM [41, 42].

To find a specific model from the transition from the missing-row reconstruction to the copper oxide formation on Cu(110) surface, further oxygen-induced reconstruction on the missing-row reconstructed Cu(110) surface at the saturated oxygen coverage

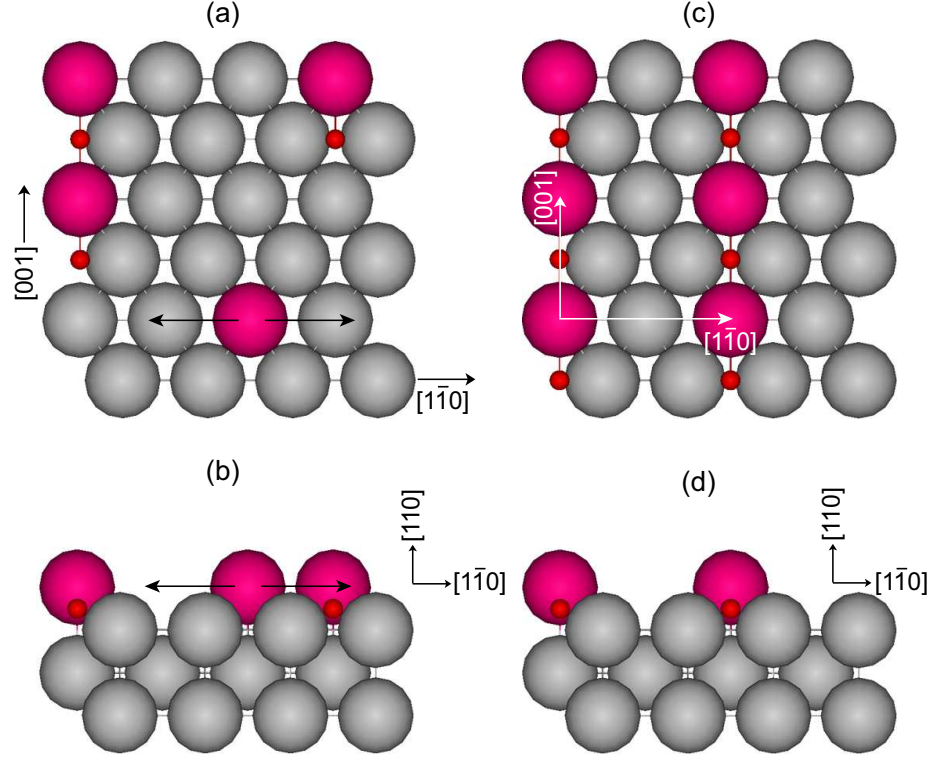


Figure 7.3: Oxygen-induced reconstruction on Cu(110) surface; (a) Top and (b) Side view of added-row reconstruction (The arrows of the topmost copper atom indicate the copper diffusion direction). (c) Top and (d) Side view of missing-row reconstruction.

needs to be investigated by DFT calculations. In the relaxed added-row (less saturated oxygen coverage) and missing-row (saturated oxygen coverage) reconstruction, an oxygen molecule is added to the unit-cell and the copper surface with the oxygen molecule is relaxed, as we did for the Cu(100) surface previously. Defects affect the oxide formation and growth on the Cu(110) surface [41]. We need to add a copper point defect (vacancy) or line defect (dislocation) to surfaces. The surfaces can then be relaxed with an additional oxygen molecule and be compared to the perfect (defect-free) cases for structural and energetic changes.



## BIBLIOGRAPHY

- [1] G. Paul, R. Ghosh, S. Bera, S. Bandyopadhyay, T. Sakurai, and K. Akimoto, "Deep level transient spectroscopy of cyanide treated polycrystalline  $p$ -Cu<sub>2</sub>O/ $n$ -ZnO solar cell." *Chemical Physics Letters* **463** (2008) 117–120.
- [2] B. Yuhas and P. Yang, "Nanowire-Based All-Oxide Solar Cells." *Journal of American Chemical Society* **131** (2009) 3756–3761.
- [3] A. Guerrero-Ruiz, I. Rodriguez-Ramos, and J. Fierro, "Dehydrogenation of methanol to methyl formate over supported copper catalysts." *Applied Catalysis* **72** (1991) 119–137.
- [4] W. Setthapun, S. K. Bej, and L. T. Thompson, "Carbide and nitride supported methanol steam reforming catalysts: Parallel synthesis and high throughput screening." *Topic in Catalysis* **49** (2008) 73–80.
- [5] F. Jing, Y. Zhang, S. Luo, W. Chu, H. Zhang, and X. Shi, "Catalytic synthesis of 2-methylpyrazine over Cr-promoted copper based catalyst via a cyclo-dehydrogenation reaction route." *Journal of Chemical Sciences* **122** (2010) 621–630.
- [6] L. Cecchi, F. D. Sarlo, and F. Machetti, "Synthesis of 4,5-dihydroisoxazoles by condensation of primary nitro compounds with alkenes by using a copper/base catalytic system." *Chemistry - A European Journal* **14** (2008) 7903–7912.
- [7] G. Centi and S. Perathoner, "Nature of active species in copper-based catalysts and their chemistry of transformation of nitrogen-oxides." *Applied Catalysis A-General* **132** (1995) 179–259.
- [8] T. Huang and D. Tsai, "CO oxidation behavior of copper and copper oxides." *Catalysis Letters* **87** (2003) 173–178.
- [9] B. White, M. Yin, A. Hall, D. Le, S. Stolbov, T. Rahman, N. Turro, and S. O'Brien, "Complete CO Oxidation over Cu<sub>2</sub>O Nanoparticles Supported on Silica Gel." *Nano Letters* **6** (2006) 2095–2098.
- [10] D. Le, S. Stolbov, and T. S. Rahman, "Reactivity of the Cu<sub>2</sub>O(100) surface: Insights from first principles calculations." *Surface Science* **603** (2009) 1637–1645.
- [11] N. Cabrera and N. F. Mott, "Theory of the oxidation of metals." *Reports on Progress in Physics* **12** (1948) 163–184.
- [12] J. C. Yang, B. Kolasa, J. M. Gibson, and M. Yeadon, "Self-limiting oxidation of copper." *Applied Physics Letters* **73** (1998) 2841–2843.
- [13] P. S. Bagus and F. Illas, "Theoretical analysis of the bonding of oxygen to Cu(100)." *Physical Review B* **42** (1990) 10852–10857.

- [14] T. Lederer, D. Arvanitis, G. Comelli, L. Troger, and K. Baberschke, "Adsorption of Oxygen on Cu(100). I. Local Structure and Dynamics for Two Atomic Chemisorption States." *Physical Review B* **48** (1993) 15390–15404.
- [15] T. Wiell, J. E. Klepeis, P. Bennich, O. Bjorneholm, N. Wassdahl, and A. Nilsson, "Local aspects of the adsorbate-substrate chemical bond in N/Cu(100) and O/Cu(100)." *Physical Review B* **58** (1998) 1655–1664.
- [16] S. Liem, J. Clarke, and G. Kresse, "Pathways to dissociation of O<sub>2</sub> on Cu (110) surface: First principles simulations." *Surface Science* **459** (2000) 104–114.
- [17] Y. Xu and M. Mavrikakis, "Adsorption and dissociation of O<sub>2</sub> on Cu(111): Thermochemistry, reaction barrier and the effect of strain." *Surface Science* **494** (2001) 131–144.
- [18] L. Padilla-Campos and P. Fuentealba, "Theoretical study of the adsorption of oxygen on a Cu(100) surface and the coadsorption with alkali atoms." *Theoretical Chemistry Accounts* **110** (2003) 414–420.
- [19] Z. X. Wang and F. H. Tian, "The adsorption of O atom on Cu (100), (110), and (111) low-index and step defect surfaces." *Journal of Physical Chemistry B* **107** (2003) 6153–6161.
- [20] M. Alatalo, S. Jaatinen, P. Salo, and K. Laasonen, "Oxygen adsorption on Cu(100): First-principles pseudopotential calculations." *Physical Review B* **70** (2004) 245417.
- [21] A. Puisto, H. Pitkanen, M. Alatalo, S. Jaatinen, P. Salo, A. S. Foster, T. Kangas, and K. Laasonen, "Adsorption of atomic and molecular oxygen on Cu(100)." *Catalysis Today* **100** (2005) 403–406.
- [22] M. Alatalo, A. Puisto, H. Pitkanen, A. Foster, and K. Laasonen, "Adsorption dynamics of O<sub>2</sub> on Cu(100)." *Surface Science* **600** (2006) 1574–1578.
- [23] T. Fujita, Y. Okawa, Y. Matsumoto, and K. Tanaka, "Phase boundaries of nanometer scale c(2×2)-O domains on the Cu(100) surface." *Physical Review B* **54** (1996) 2167–2174.
- [24] S. Stolbov, A. Kara, and T. S. Rahman, "Electronic structure of the c(2x2)O/Cu(001) system." *Physical Review B* **66** (2002) 245405.
- [25] H. C. Zeng, R. A. McFarlane, and K. A. R. Mitchell, "A LEED crystallographic investigation of some missing row models for the Cu(100)-(2√2 × √2)R45°-O surface structure." *Surface Science* **208** (1989) L7–L14.
- [26] F. Jensen, F. Besenbacher, E. Laegsgaard, and I. Stensgaard, "Dynamics of oxygen-induced reconstruction of Cu(100) studied by scanning tunneling microscopy." *Physical Review B* **42** (1990) 9206–9212.
- [27] K. W. Jacobsen and J. K. Norskov, "Theory of the Oxygen-Induced Restructuring of Cu(110) and Cu(100) surfaces." *Physical Review Letters* **65** (1990) 1788–1791.
- [28] F. M. Leibsle, "STM studies of oxygen-induced structures and nitrogen coadsorption on the Cu(100) surface: Evidence for a one-dimensional oxygen reconstruction and reconstructive interactions." *Surface Science* **337** (1995) 51–66.
- [29] D. Sekiba, T. Inokuchi, Y. Wakimoto, K. Yagi-Watanabe, and H. Fukutani, "Electronic structure of Cu(100)(2√2 × √2)R45°-O surface: Angle-resolved photoemission spectroscopy and tight-binding calculation." *Surface Science* **470** (2000) 43–52.
- [30] M. Kittel, M. Polcik, R. Terborg, J.-T. Hoeft, P. Baumgartel, A. Bradshaw, R. Toomes, J.-H. Kang, D. Woodru, M. Pascal, C. Lamont, and E. Rotenberg, "The structure of oxygen on Cu(100) at low and high coverages." *Surface Science* **470** (2001) 311–324.

- [31] S. Stolbov and T. S. Rahman, “Role of long range interaction in oxygen superstructure formation on Cu(001) and Ni(001).” *Physical Review Letters* **89** (2002) 116101.
- [32] M. J. Harrison, D. P. Woodruff, J. Robinson, W. P. D. Sander, and J. Kirschner, “Adsorbate-induced surface reconstruction and surface-stress changes in Cu(100)/O: Experiment and theory.” *Physical Review B* **74** (2006) 165402.
- [33] N. Bonini, A. Kokalj, A. D. Corso, S. de Gironcoli, and S. Baroni, “Structure and dynamics of the missing-row reconstruction on O/Cu(001) and O/Ag(001).” *Surface Science* **600** (2006) 5074–5079.
- [34] H. Iddir, D. D. Fong, P. Zapol, P. H. Fuoss, L. A. Curtiss, G.-W. Zhou, and J. A. Eastman, “Order-disorder phase transition of the Cu(001) surface under equilibrium oxygen pressure.” *Physical Review B* **76** (2007) 241404(R).
- [35] S. Jaatinen, J. Blomqvist, P. Salo, A. Puisto, M. Alatalo, M. Hirsimäki, M. Ahonen, and M. Valden, “Adsorption and diffusion dynamics of atomic and molecular oxygen on reconstructed Cu(100).” *Physical Review B* **74** (2007) 075402.
- [36] X. Duan, O. Warschkow, A. Soon, B. Delley, and C. Stampfl, “Density functional study of oxygen on Cu(100) and Cu(110) surfaces.” *Physical Review B* **81** (2010) 075430–1–15.
- [37] M. Lampimäki, K. Lahtonen, M. Hirsimäki, and M. Valden, “Nanoscale oxidation of Cu(100): Oxide morphology and surface reactivity.” *Journal of Chemical Physics* **126** (2007) 034703.
- [38] K. Lahtonen, M. Hirsimäki, M. Lampimäki, and M. Valden, “Oxygen adsorption-induced nanostructures and island formation on Cu(100): Bridging the gap between the formation of surface confined oxygen chemisorption layer and oxide formation.” *Journal of Chemical Physics* **129** (2008) 124703.
- [39] G. Zhou and J. C. Yang, “Formation of quasi-one-dimensional Cu<sub>2</sub>O structures by in situ oxidation of Cu(100).” *Physical Review Letters* **89** (2002) 106101.
- [40] G. Zhou and J. C. Yang, “Temperature effect on the Cu<sub>2</sub>O oxide morphology created by oxidation of Cu(001) as investigated by in situ UHV-TEM.” *Applied Surface Science* **210** (2003) 165–170.
- [41] G. Zhou and J. C. Yang, “In situ UHV-TEM investigation of the kinetics of initial stages of oxidation on the roughened Cu(110) surface.” *Surface Science* **559** (2004) 100–110.
- [42] G. Zhou and J. C. Yang, “Initial oxidation kinetics of Cu(100), (110), and (111) thin films investigated by in situ ultra-high-vacuum transmission electron microscopy.” *Journal of Materials Research* **20** (2005) 1684–1694.
- [43] G. M. Whitesides and M. Boncheva, “Beyond molecules: Self-assembly of mesoscopic and macroscopic components.” *Proceedings of the National Academy of Sciences of the United States of America* **99** (2002) 4769–4774.
- [44] N. Hartmann and R. J. Madix, “Growth and ordering of Cu-O islands during oxygen adsorption on Cu(110) at 470 K.” *Surface Science* **488** (2001) 107–122.
- [45] Y. P. Guo, K. C. Tan, H. Q. Wang, C. H. A. Huan, and A. T. S. Wee, “Low-energy electron diffraction study of oxygen-induced reconstructions on Cu(210).” *Physical Review B* **66** (2002) 165410–1–8.
- [46] Y. Uehara, T. Matsumoto, and S. Ushioda, “Identification of O atoms on a Cu(110) surface by scanning tunneling microscope light emission spectra.” *Physical Review B* **66** (2002) 075413–1–5.

- [47] D. Loffreda, A. D. Corso, S. Baroni, L. Savio, and M. R. Luca Vattuone b, “Oxygen vibrations in O/Ag(001).” *Surface Science* **530** (2003) 26–36.
- [48] M. Hirsimäki, M. Lampima, K. Lahtonen, I. Chorkendorff, and M. Valden, “Investigation of the role of oxygen induced segregation of Cu during Cu<sub>2</sub>O formation on Cu(100), Ag/Cu(100) and Cu(Ag) alloy.” *Surface Science* **583** (2005) 157–165.
- [49] L. Sun and J. Yang, “The low-temperature initial oxidation stages of Cu(100) investigated by in situ ultra-high-vacuum transmission electron microscopy.” *Journal of Materials Research* **20** (2005) 1910–1917.
- [50] K. Moritani, M. Okada, T. Fukuyama, Y. Teraoka, A. Yoshigoe1, and T. Kasai, “The azimuthal dependent oxidation process on Cu(110) by energetic oxygen molecules.” *The European Physical Journal D* **38** (2006) 111–115.
- [51] H. Agren, V. Carravetta, and L. G. M. Pettersson, “Static exchange and cluster modeling of core electron shakeup spectra of surface adsorbates: CO/Cu(100).” *Physical Review B* **53** (1996) 16074–16085.
- [52] F. Frechard and R. van Santen, “Theoretical study of the adsorption of the atomic oxygen on the Cu(110) surface.” *Surface Science* **407** (1998) 200–211.
- [53] J. Gomes and J. Gomes, “Adsorption of the formate species on copper surfaces: DFT study.” *Surface Science* **432** (2003) 279–290.
- [54] A. Puisto, *Oxygen adsorption on clean and oxygen precovered Cu(100)*. Master of science thesis, Lappeenranta University of Technology, Lappeenranta, Finland (2004), see also [http://www.ee.lut.fi/fi/lab/elemtat/julkaisut/masters thesis apuisto.pdf](http://www.ee.lut.fi/fi/lab/elemtat/julkaisut/masters%20thesis%20apuisto.pdf).
- [55] C. D. Valentin, A. Figini, and G. Pacchioni, “Adsorption of NO and NO<sub>2</sub> on terrace and step sites and on oxygen vacancies of the CaO(100) surface.” *Surface Science* **556** (2004) 145–158.
- [56] L. Jiang, G.-C. Wang, Z.-S. Cai, Y.-M. Pan, and X.-Z. Zhao, “Promotion of the water-gas shift reaction by pre-adsorbed oxygen on Cu(hkl) surfaces: a theoretical study.” *Journal of Molecular Structure (Theochem)* **710** (2004) 97–104.
- [57] T. Kangas, K. Laasonen, A. Puisto, H. Pitkanen, and M. Alatalo, “On-surface and sub-surface oxygen on ideal and reconstructed Cu(100).” *Surface Science* **584** (2005) 62–69.
- [58] N. Nivalainen, *Oxygen adsorption on Cu(211) and structurally and chemically modified Cu(100)*. Master of science thesis, Lappeenranta University of Technology, Lappeenranta, Finland (2007), see also [http://www.ee.lut.fi/fi/lab/elemtat/julkaisut/masters thesis nivalainen.pdf](http://www.ee.lut.fi/fi/lab/elemtat/julkaisut/masters%20thesis%20nivalainen.pdf).
- [59] A. Puisto, *The Initial Oxidation of Transition Metal Surfaces*. Phd thesis, Lappeenranta University of Technology, Lappeenranta, Finland (2008).
- [60] C. Q. Sun, “Oxidation electronics: bond-band-barrier correlation and its applications.” *Progress in Materials Science* **48** (2003) 521–685.
- [61] T. Kangas and K. Laasonen, “DFT study of reconstructed Cu(100) surface with high oxygen coverages.” *Surface Science* **602** (2008) 3239–3245.
- [62] G. Kresse and J. Hafner, “Ab initio molecular dynamics for liquid metals.” *Physical Review B* **47** (1993) 558–561.
- [63] G. Kresse and J. Hafner, “Ab initio molecular-dynamics simulation of the liquid-metal-amorphous-semiconductor transition in germanium.” *Physical Review B* **49** (1994) 14251–14269.

- [64] G. Kresse and J. Hafner, “Norm-conserving and ultrasoft pseudopotentials for first-row and transition elements.” *Journal of Physics: Condensed Matter* **6** (1994) 8245–8257.
- [65] G. Kresse and J. Fürthmüller, “Efficiency of ab-initio total energy calculations for metals and semiconductors using a plane-wave basis set.” *Computational Materials Science* **6** (1996) 15–50.
- [66] G. Kresse and J. Fürthmüller, “Efficient iterative schemes for ab-initio total-energy calculations using a plane-wave basis set.” *Physical Review B* **54** (1996) 11169–11186.
- [67] M. Lee and A. J. H. McGaughey, “Energetics and kinetics of the  $c(2 \times 2)$  to  $(2\sqrt{2} \times \sqrt{2})R45^\circ$  transition on the Cu(100) surface.” (in preparation).
- [68] M. Lee and A. J. H. McGaughey, “Energetics of oxygen embedment into unreconstructed and reconstructed Cu(100) surfaces: Density functional theory calculations.” *Surface Science* **603** (2009) 3404–3409.
- [69] M. Lee and A. J. H. McGaughey, “Role of sub-surface oxygen in Cu(100) oxidation.” *Surface Science* **604** (2010) 1425–1431.
- [70] M. Lee, W. Al-Saidi, and A. J. H. McGaughey, “*Ab-initio* atomistic thermodynamics study of early stages of Cu(100) oxidation.” (in preparation).
- [71] E. Schrödinger, “An Undulatory Theory of the Mechanics of Atoms and Molecules.” *Physical Review* **28** (1926) 1049–1070.
- [72] P. Hohenberg and W. Kohn, “Inhomogeneous electron gas.” *Physical Review* **136** (1964) B864–B871.
- [73] W. Kohn and L. J. Sham, “Self-consistent equation including exchange and correlation effects.” *Physical Review* **140** (1965) A1133–A1138.
- [74] J. P. Perdew, K. Burke, and M. Ernzerhof, “Generalized Gradient Approximation Made Simple.” *Physical Review Letters* **77** (1996) 3865–3868.
- [75] D. Young, *Computational Chemistry: A Practical Guide for Applying Techniques to Real World Problems Appendix A. A.2.1 pg 332, ADF*. Wiley-Interscience, New York (2001).
- [76] X. Gonze, J.-M. Beuken, R. Caracas, F. Detraux, M. Fuchs, G.-M. Rignanese, L. Sindic, M. Verstraete, G. Zerah, F. Jollet, M. Torrent, A. Roy, M. Mikami, P. Ghosez, J.-Y. Raty, and D. Allan, “First-principles computation of material properties: the ABINIT software project.” *Computational Materials Science* **25** (2002) 478–492.
- [77] J. M. Soler, E. Artacho, J. D. Gale, A. Garcia, J. Junquera, P. Ordejon, and D. Sanchez-Portal, “The SIESTA method for ab initio order-N materials simulation.” *Journal of Physics: Condensed Matter* **14** (2002) 2745–2779.
- [78] M. F. Guest, I. J. Bush, H. J. J. van Dam, P. Sherwood, J. M. H. Thomas, J. H. van Lenthe, R. W. A. Havenith, and J. Kendrick, “The GAMESS-UK structure package: algorithms, developments and applications.” *Molecular Physics* **103** (2005) 719–747.
- [79] H. J. Monkhorst and J. D. Pack, “Special points for Brillouin-zone integrations.” *Physical Review B* **13** (1976) 5188–5192.
- [80] F. R. Kroeger and C. A. Swenson, “Absolute linear thermal-expansion measurements on copper and aluminum from 5 to 320K.” *Journal of Applied Physics* **48** (1977) 853–864.
- [81] A. K. Giri and G. B. Mitra, “Extrapolated values of lattice constantso f some cubic metals at absolute zero.” *Journal of Physics D: Applied Physics* **18** (1985) L75–L782.

- [82] D. R. Lide, *CRC Handbook of Chemistry and Physics, Student Edition. 84th Edition.* CRC Press, New York (2004).
- [83] J. Greeley, A. Gokhale, J. Kreuser, J. Dumesic, H. Topsøe, N.-Y. Topsøe, and M. Mavrikakis, “CO vibrational frequencies on methanol synthesis catalysts: a DFT study.” *Journal of Catalysis* **213** (2003) 63–72.
- [84] T. L. Cottrell, *The Strengths of Chemical Bonds, 2nd ed.* Butterworths, London (1958).
- [85] B. D. Darwent, *National Standard Reference Data Series.* National Bureau of Standards, No. 31, Washington, DC (1970).
- [86] J. P. Perdew, J. A. Chevary, S. H. Vosko, K. A. Jackson, M. R. Pederson, D. J. Singh, and C. Fiolhais, “Atoms, molecules, solids, and surfaces: Applications of the generalized gradient approximation for exchange and correlation.” *Physical Review B* **46** (1992) 6671–6687.
- [87] H. Jónsson, G. Mills, and K. W. Jacobsen, *Classical and Quantum Dynamics in Condensed Phase Simulations.* edited by B. J. Berne, G. Ciccotti, and D. F. Coker, World Scientific, Singapore (1998).
- [88] G. Henkelman, B. P. Uberuaga, and H. Jónsson, “A climbing image nudged elastic band method for finding saddle points and minimum energy paths.” *Journal of Chemical Physics* **113** (2000) 9901–9904.
- [89] G. Henkelman and H. Jónsson, “Improved tangent estimate in the nudged elastic band method for finding minimum energy paths and saddle points.” *Journal of Chemical Physics* **113** (2000) 9978–9985.
- [90] R. A. Olsen, G. J. Kroes, G. Henkelman, A. Arnaldsson, and H. Jónsson, “Comparison of methods for finding saddle points without knowledge of the final states.” *Journal of Chemical Physics* **121** (2004) 9776–9792.
- [91] J. C. Yang, M. Yeadon, B. Kolasa, and J. M. Gibson, “The Homogeneous Nucleation Mechanism of Cu<sub>2</sub>O on Cu(001).” *Scripta Materialia* **38** (1998) 1237–1242.
- [92] J. A. Venables, *Introduction to Surface and Thin Film Process.* Cambridge University Press, Cambridge (2000).
- [93] H. Eyring, “The Activated Complex in Chemical Reactions.” *Journal of Chemical Physics* **3** (1935) 107–115.
- [94] K. J. Laidler and M. C. King, “The Development of Transition-State Theory.” *Journal of Physical Chemistry* **87** (1983) 2657–2664.
- [95] A. F. Voter, “Classically exact overlayer dynamics: Diffusion of rhodium clusters on Rh(100).” *Physical Review B* **34** (1986) 6819–6829.
- [96] D. S. Sholl and J. Steckel, *Density Functional Theory: A Practical Introduction.* John Wiley & Sons (2008).
- [97] W. M. Young and E. W. Elcock, “Monte Carlo Studies of Vacancy Migration in Binary Ordered Alloys - I.” *Proceedings of the Physical Society* **89** (1966) 735.
- [98] J. Venables, G. Spiller, and M. Hanbuchen, “Nucleation and growth of thin-films.” *Reports on Progress in Physics* **47** (1984) 399–459.
- [99] P. Ruggerone, C. Ratsch, and M. Scheffler, “Chapter 13. Density-functional theory of epitaxial growth of metals.” *The Chemical Physics of Solid Surfaces* **8** (1997) 490–544.

- [100] D. Landau and K. Binder, *A Guide to Monte Carlo Simulation in Statistical Physics*. Cambridge University Press, Cambridge (2003).
- [101] E. Cox, M. Li, P.-W. Chung, C. Ghosh, T. S. Rahman, C. J. Jenks, J. W. Evans, and P. A. Thiel, "Temperature dependence of island growth shapes during submonolayer deposition of Ag on Ag(111)." *Physical Review B* **71** (2005) 115414–1–9.
- [102] I. Batyrev, A. Alavi, and M. W. Finnis, "*Ab initio* calculations of the  $\text{Al}_2\text{O}_3$  (0001) surface." *Faraday Discuss.* **144** (1999) 33–43.
- [103] J. M. Hawkins, J. F. Weaver, and A. Asthagiri, "Density functional theory study of the initial oxidation of the Pt(111) surface." *Physical Review B* **79** (2009) 125434–1–13.
- [104] R. F. W. Bader, *Atoms in Molecules: A Quantum Theory*. Oxford University Press, Oxford (1990).
- [105] G. Henkelman, A. Arnaldsson, and H. Jónsson, "A fast and robust algorithm for Bader decomposition of charge density." *Computational Materials Science* **36** (2006) 354–360.
- [106] J. Kitchin, J. Norskov, M. Barteau, and J. Chen, "Modification of the surface electronic and chemical properties of Pt(111) by subsurface 3d transition metals." *Journal of Chemical Physics* **120** (2004) 10240–10246.
- [107] C. Weinert and M. Scheffler, "Chalcogen and Vacancy Pairs in Silicon Electronic Structure and Stabilities." *Materials Science Forum* **10-12** (1986) 25–30.
- [108] E. Kaxiras, Y. Bar-Yam, J. Joannopoulos, and K. Pandey, "Ab initio theory of polar semiconductor surfaces. I. Methodology and the (22) reconstructions of GaAs(111)." *Physical Review B* **35** (1987) 9625–9635.
- [109] X.-G. Wang, W. Weiss, S. Shaikhutdinov, M. Ritter, M. Petersen, F. Wagner, R. Schlögl, and M. Scheffler, "The Hematite ( $\alpha\text{-Fe}_2\text{O}_3$ ) (0001) Surface: Evidence for Domains of Distinct Chemistry." *Physical Review Letters* **81** (1998) 1038–1041.
- [110] X.-G. Wang, A. Chaka, and M. Scheffler, "Effect of the Environment on  $\alpha\text{-Al}_2\text{O}_3$  (0001) Surface Structures." *Physical Review Letters* **84** (2000) 3650–3653.
- [111] K. Reuter and M. Scheffler, "Composition, structure, and stability of  $\text{RuO}_2$ (110) as a function of oxygen pressure." *Physical Review B* **65** (2001) 035406–1–11.
- [112] K. Reuter and M. Scheffler, "First-Principles Atomistic Thermodynamics for Oxidation Catalysis: Surface Phase Diagrams and Catalytically Interesting Regions." *Physical Review Letters* **90** (2003) 046103–1–4.
- [113] J. R. Kitchin, K. Reuter, and M. Scheffler, "Alloy surface segregation in reactive environments: First-principles atomistic thermodynamics study of  $\text{Ag}_3\text{Pd}$ (111) in oxygen atmospheres." *Physical Review B* **77** (2008) 075437–1–12.
- [114] A. Soon, X.-Y. Cui, B. Delley, S.-H. Wei, and C. Stampfl, "Native defect-induced multifarious magnetism in nonstoichiometric cuprous oxide: First-principles study of bulk and surface properties of  $\text{Cu}_{2-\delta}\text{O}$ ." *Physical Review B* **79** (2009) 035205–1–15.
- [115] N. Inoğlu and J. R. Kitchin, "Atomistic thermodynamics study of the adsorption and the effects of water-gas shift reactants on Cu catalysts under reaction conditions." *Journal of Catalysis* **261** (2009) 188–194.
- [116] D. R. Stull and H. Prophet, *JANAF Thermochemical Tables, 2nd ed.* U.S. National Bureau of Standards, Washington, DC (1971).
- [117] R. Wyckoff, *Crystal Structures Vol. I*. John Wiley & Sons, New York (1963).

- [118] X. Han, R. McAfee, and J. C. Yang, "Kinetic Monte Carlo Simulations of the Dramatic Effects of Attachment Probability and Potential Gradients on Island Morphology Variations under Heteroepitaxial Growth Conditions." *Journal of Computational and Theoretical Nanoscience* **5** (2008) 117–128.
- [119] A.-L. Barabasi and H. Stanley, *Fractal Concepts in Surface Growth*. Cambridge University Press, Cambridge (1995).
- [120] A. Pimpinelli and J. Villain, *Physics of Crystal Growth*. Cambridge University Press, Cambridge (1998).
- [121] C. Ratsch and J. Venables, "Nucleation theory and the early stages of thin film growth." *Journal of Vacuum Science & Technology A* **21** (2003) S96–S109.
- [122] T. Michely and J. Krug, *Islands, Mounds, and Atoms*. Springer, Berlin (2004).
- [123] K. Caspersen, D.-J. Liu, M. Bartelt, C. Stoldt, A. Layson, P. Thiel, J. Evans, M. G. (editor), and L. C. (editor), *Computational Materials Chemistry in pp. 91-124: Methods and Applications*. Kluwer, Dordrecht (2004).
- [124] S. J. Cook and P. Clancy, "Comparison of semi-empirical potential functions for silicon and germanium." *Physical Review B* **47** (1993) 7686–7699.
- [125] L. Pelaz, L. Marques, M. Aboy, P. Lopez, I. Santos, and R. Duffy, "Atomistic process modeling based on Kinetic Monte Carlo and Molecular Dynamics for optimization of advanced devices." In "Electron Devices Meeting (IEDM), 2009 IEEE International," 1–4.
- [126] F. H. Stillinger and T. A. Weber, "Computer simulation of local order in condensed phases of silicon." *Physical Review B* **31** (1985) 5262–5271.
- [127] T. J. Raeker and A. E. Depristo, "Theory of chemical bonding based on the atom-homogeneous electron-gas system." *International Reviews in Physical Chemistry* **10** (1991) 1–54.
- [128] M. Daw, S. Folies, and M. Baskes, "The Embedded-Atom Method - A Review of Theory and Applications." *Materials Science Reports* **9** (1993) 251–310.
- [129] P. Stoltze, "Simulation of Surface-Defects." *Journal of Physics: Condensed Matter* **6** (1994) 9495–9517.
- [130] G.-D. Lee, C. Z. Wang, Z. Y. Lu, and K. M. Ho, "Ad-Dimer Diffusion between Trough and Dimer Row on Si(100)." *Physical Review Letters* **81** (1998) 5872–5875.
- [131] F. Baumann, D. Chopp, T. de la Rubia, G. Gilmer, J. Greene, H. Huang, S. Kodambaka, P. O'Sullivan, and I. Petrov, "Multiscale modeling of thin-film deposition: Applications to Si device processing." *MRS Bulletin* **26** (2001) 182–189.
- [132] A. F. Voter, F. Montalenti, and T. C. Germann, "Extending the time scale in atomistic simulation of materials." *Annual Review of Materials Research* **32** (2002) 321–346.
- [133] M. Breeman and D. Boerma, "Atomic Mobilities on a stepped Cu(100) surface." *Surface Science* **287** (1993) 881–885.
- [134] O. Biham, I. Furman, M. Karimi, G. Vidali, R. Kennett, and H. Zeng, "Models for diffusion and island growth in metal monolayers." *Surface Science* **400** (1998) 29–43.
- [135] E. Hansen and M. Neurock, "Modeling surface kinetics with first-principles-based molecular simulation." *Chemical Engineering Science* **54** (1999) 3411–3421.
- [136] E. Hansen and M. Neurock, "First-principles-based Monte Carlo simulation of ethylene hydrogenation kinetics on Pd." *Journal of Catalysis* **196** (2000) 241–252.



- [137] F. Grosse and M. Gyure, “Island and step morphology in InAs(001) homoepitaxy.” *Physica Status Solidi B-Basic Research* **234** (2002) 338–345.
- [138] D. Mei, Q. Ge, M. Neurock, L. Kieken, and J. Lerou, “First-principles-based kinetic Monte Carlo simulation of nitric oxide decomposition over Pt and Rh surfaces under lean-burn conditions.” *Molecular Physics* **102** (2004) 361–369.
- [139] M. E. Bjorketun, P. G. Sundell, G. Wahnstrom, and D. Engberg, “A kinetic Monte Carlo study of proton diffusion in disordered perovskite structured lattices based on first-principles calculations.” *Solid State Ionics* **176** (2005) 3035–3040.
- [140] D.-J. Liu, “CO oxidation on Rh(100): Multisite atomistic lattice-gas modeling.” *Journal of Physical Chemistry C* **111** (2007) 14698–14706.
- [141] S. Jaatinen, M. Rusanen, and P. Salo, “A multi-scale Monte Carlo study of oxide structures on the Cu(100) surface.” *Surface Science* **601** (2007) 1813–1821.
- [142] A. Dkhissi, G. Mazaleyrat, A. Esteve, and M. D. Rouhani, “Nucleation and growth of atomic layer deposition of HfO<sub>2</sub> gate dielectric layers on silicon oxide: a multiscale modelling investigation.” *Physical Chemistry Chemical Physics* **11** (2009) 3701–3709.
- [143] A. Kushima and B. Yildiz, “Oxygen ion diffusivity in strained yttria stabilized zirconia: where is the fastest strain?” *Journal of Materials Chemistry* **20** (2010) 4809–4819.
- [144] N. Dinter, M. Rusanen, P. Raybaud, S. Kasztelan, P. da Silva, and H. Toulhoat, “Temperature-programmed reduction of unpromoted MoS<sub>2</sub>-based hydrodesulfurization catalysts: First-principles kinetic Monte Carlo simulations and comparison with experiments.” *Journal of Catalysis* **275** (2010) 117–128.
- [145] D. Mei, J. Du, and M. Neurock, “First-Principles-Based Kinetic Monte Carlo Simulation of Nitric Oxide Reduction over Platinum Nanoparticles under Lean-Burn Conditions.” *Industrial & Engineering Chemistry Research* **49** (2010) 10364–10373.
- [146] F. Jensen, F. Besenbacher, E. Laegsgaard, and I. Stensgaard, “Surface reconstruction of Cu(110) induced by oxygen chemisorption.” *Physical Review B* **41** (1990) 10233–10236.
- [147] Y. Kuk, F. M. Chua, P. J. Silverman, and J. A. Meyer, “O chemisorption on Cu(110) by scanning tunneling microscopy.” *Physical Review B* **41** (1990) 12393–12402.
- [148] A. Soon, M. Todorova, B. Delley, and C. Stampfl, “Oxygen adsorption and stability of surface oxides on Cu(110): A first-principles investigation.” *Physical Review B* **73** (2006) 165424–1–12.
- [149] X.-Y. Pang, L.-Q. Xue, and G.-C. Wang, “Adsorption of atoms on Cu surfaces: a density functional theory study.” *Langmuir* **23** (2007) 4910–4917.